ABSTRACT

Title of Dissertation: FLUID-STRUCTURE INTERACTIONS: IMPLOSIONS OF SHELL STRUCTURES AND WAVE IMPACT ON A FLAT PLATE

Christine M. Ikeda, Doctor of Philosophy, 2012

Advisor: Professor James H. Duncan
Department of Mechanical Engineering

The work in this dissertation examines the fluid-structure interaction phenomena in a series of three experimental studies. The first two sets of experiments were conducted in a large, water-filled pressure vessel with a nominal internal diameter of 1.77 m. Cylindrical shells were made from thin-walled aluminum and brass tubes with circular cross-sections (internal diameters D) and internal clearance-fit aluminum end caps. Implosion and explosion events were photographed with a high-speed camera (27,000 frames per second), and the waterborne pressure waves resulting from the implosion were measured simultaneously with underwater blast sensors. The natural implosions were generated by raising the ambient water pressure slowly to a value, P_c, just above the elastic instability limit of the models. For the models with larger L/D, where L is the internal length of the model, the model cross sections flattened during the implosion (mode 2). It was found that the amplitude of these mode 2 pressure waves scale with the pressure difference $\Delta P = P_c - P_i$ (where P_i is the internal pressure of the air inside the cylindrical models) and the

time scales with $(D/2)\sqrt{\rho/\Delta P}$ (where ρ is the density of water). The geometry and material properties of the structure seem to play only a secondary role. During the explosion experiments, the pressure vessel is pressurized to various pressure levels below the natural implosion pressure of the models and an explosive was set off nearby. It was found that the implosion is induced by one of two mechanisms: the shockwave generated by the explosion and the hydrodynamic pressure field of the explosion bubble during its collapse and re-expansion. In the final experimental study, the impact of a plunging breaking wave (wavelength ≈ 1.2 m) on a partially submerged cube (with dimensions $L = 0.3048$ m) is studied in a wave tank (14.8 m long). The water free surface shape upstream of the cube before and after the wave impact was measured with cinematic Laser-Induced Fluorescence (LIF), employing a high-speed digital camera, a laser light sheet and fluorescent dye mixed with the water. It was observed that for some cube positions, the free surface between the front face of the cube and the wave crest forms a circular arc that converges to a point and forms a high-velocity vertical jet (≈ 3 m/s). Although these problems are intrinsically different, they are flows dominated by inertial forces (viscous effects are not important) where a rapidly collapsing interface shape produces high-pressure waves.

Fluid Structure Interactions: Implosions of Shell Structures and Wave Impact on a Flat Plate

by

Christine M. Ikeda

Dissertation submitted to the Faculty of the Graduate School of the
University of Maryland, College Park in partial fulfillment
of the requirements for the degree of
Doctor of Philosophy
2012

Advisory Committee:
Professor James H. Duncan, Chair/Advisor
Professor Amir Riaz
Professor Balakumar Balachandran
Professor William Fourney
Professor Richard Calabrese, Dean's Representative

Acknowledgments

First and most importantly, I would like to thank my advisor, Professor James H. Duncan, for giving me my first experience conducting research as an undergraduate. Without this opportunity, I would have never found a passion for experimental research in Fluid Dynamics. Working with him in the last six years has been a pleasure, and I aspire to be like him.

I would also like to thank my committee members, Professor William Fourney, Professor Balakumar Balachandran, Professor Amir Riaz and Dean's Representative, Professor Richard Calabrese, for their time and feedback on my dissertation and research. I would also like to acknowledge the other faculty members and staff who have also helped me over the years: Professor Kenneth Kiger, Professor Santiago Solares, Professor James Wallace, Ulrich Lieste and Amarildo DaMata.

I also wish to acknowledge my colleagues in the Hydrodynamics lab: Dr. Xinan Liu, Dr. Mostafa Shakeri, Dr. Eric Maxeiner, Dr. James Diorio, Dr. Mohammadreza Tavakolinejad, Naeem Nasnadi, Ren Liu, Dan Wang, Nathan Washuta, An Wang and Karan Parmar. In addition, I would like to acknowledge the help of the following undergraduate students: Martin Czechanowski, Jens Wilkerling, Christoph Rother, Ronen Lautman, Steffen Harbarth and Michael Choquette. I would also like to acknowledge Marcelo Valdez for his assistance in the ANSYS calculations.

Finally, I would like to thank my family and friends for their support.

Table of Contents

List of Tables

List of Figures

Chapter 1

Introduction

Fluid-structure interaction phenomena are very common in nature. However, the underlying physics of these interactions is not as well understood due to their complex nature. The work in this dissertation studies small piece of the fluid-structure interaction field in a series of three experimental studies: (1) the natural implosion of cylindrical shell structures in a high-pressure water environment, (2) the explosion-induced implosion of cylindrical shell structures in a high-pressure water environment, and (3) the impact of a deep-water plunging breaking wave on a partially submerged rigid cube. Although these three physical problems are intrinsically different, they share some physical features. The first feature is that there is a rapidly collapsing interface shape that produces high-pressure waves. The second feature is that each flow is dominated by inertia forces and viscosity is not important.

For the natural implosion of cylindrical shell structures, to be discussed in Chapter 2, a cavity of air is surrounded by a thin cylindrical structure, which is in turn surrounded by high-pressure water. The collapse of this cavity involves the buckling of the structure. The generated pressure waves during the natural implosion event have contributions from both, the structure and the air cavity. The impact of the collapsed walls of the cylinder against each other, as well as the collapse

of the air cavity produce a distinct pressure pulse.

Typical time scales of these implosion events are on the order of 1 ms. The growth rate of the boundary layer surrounding the cylindrical structure can be estimated as $\delta \sim \sqrt{\nu t}$, where ν is the kinematic viscosity. Using a value of $\nu = 1.004 \times 10^{-6}$ m^2/s for water at 20°C, the final thickness of this boundary layer after the implosion event is estimated at 1 μm.

The explosion-induced implosions of cylindrical shell structures, to be discussed in Chapter 3, involve two cavities of gas. The first cavity is the air surrounded by the thin metallic structure, and the second cavity is the explosive gas bubble created during the explosion event. The pressure waves resulting from the explosion event include a distinguishable shockwave front and several pressure oscillations due to the multiple cycles of collapse and re-expansion of the explosion gas bubble and reflections from the tank walls. Pressure waves also result from the collapse of the cylindrical structure and internal air cavity.

The time scale of the shockwave is typically on the order of 1 ns, while the time-scale of the implosion is again on the order of milliseconds. An estimate of the boundary layer growth over the time duration of an explosion is 31.7 nm. This value is a conservative estimation since, in actuality, the local temperature of the water near the structure is increased as a consequence of the explosion event. This increased temperature corresponds to a decreased kinematic viscosity (for example, 0.326×10^{-6} m^2/s for water at 90°C), and thus, the boundary layer would be even thinner.

Finally, when a deep-water plunging breaking wave impacts the front face of a

partially submerged cube, the presence of the wall causes the wave breaking event to change. During this event, the crest of the wave steepens as it approaches the wall, and the water level between the cube and the crest increases, creating a circular arc. This arc closes as the wave crest progresses toward the wall. In some cases, the wave crest begins to break and curl over, closing the circular arc and entrapping air. The focusing of this circular water surface into a smaller and smaller arc is accompanied by high accelerations and high pressure gradients. The impact of the wave on the front face of the cube produces a strong peak pressure on the cube, and this is usually accompanied by a strong vertical jet of water. The air cavity in question is only partially closed and is bounded by the front face of the cube and the free-surface of the water. The time scale of the wave impact event is on the order of 0.1 s. An estimate of the boundary layer growth over the time duration of the wave impact is 0.45 mm.

For the three different physical events, the time scales are short enough that viscous diffusion does not have time to affect the physics of the flow. As described above, the thickest boundary layer is encountered on the surface of the cube impacted by a plunging wave and is estimated to be less than 0.5 mm. The thinnest boundary layer, developing on the surface of a collapsing cylindrical shell subject to a nearby explosion, was of the order of nanometers. In comparison to the length scales of the structures (17 mm to 31 mm for the cylindrical shell structures and 31 cm for the cube), the boundary layer is negligible.

This dissertation is a combination of three projects that shall be discussed in Chapters 2, 3, and 4. The first project is on the natural implosion of cylindrical shell

structures in high-pressure water (Chapter 2). The second project is a continuation of the first project and examines the implosion of cylindrical shell structures in high-pressure water due to a nearby explosion (Chapter 3). The final project is on the impact of a plunging breaking wave on a partially submerged cube in deep water (Chapter 4). Finally, Chapter 5 shall discuss the main conclusions obtained from these projects.

Chapter 2

The Implosion of Cylindrical Shell Structures in High-Pressure Water

2.1 Abstract

The implosion of cylindrical shell structures in a high-pressure water environment was studied experimentally. The shell structures are made from thin-walled aluminum and brass tubes with circular cross sections and internal clearance-fit aluminum end caps. The internal diameters of the tubes ranged from 15-mm to 40-mm diameters (D) and the internal length-to-diameter ratios (L/D) were between 2.3 and 10. The models were filled with air at atmospheric pressure, P_i. The implosions were generated in a high-pressure tank with a nominal internal diameter of 1.77 m by raising the ambient water pressure slowly to a value, P_c, just above the elastic instability limit of each shell structure. The implosion events were photographed with a high-speed digital movie camera and the pressure waves were measured simultaneously with an array of underwater blast sensors. For the models with larger L/D, the tubes flatten during implosion (with a mode 2 cross-sectional shape). In these cases, it was found that the pressure wave profiles primarily scale with the pressure difference $\Delta P = P_c - P_i$ and the time scale $(D/2)\sqrt{\rho/\Delta P}$, where ρ is the density of water, with the details of the structure producing only secondary effects. For models with smaller L/D, the tubes imploded with modes 3 and 4, meaning that 3 or 4 lobes were formed in the final cross-sectional shape. Even when these

geometries were chosen to have the same available energy (P_cV, where V is the internal volume of air inside the cylindrical shell), the pressure wave profiles did not scale using fluid properties.

2.2 Introduction

2.2.1 Literature Review

The collapse or implosion of cylindrical shell structures produces high-frequency pressure waves that can cause damage to nearby structural elements. Predictions of the onset of elastic instability and critical mode number based on linear theory for simple shell structures (spheres and cylinders) have been available from the 1850s for the application of boiler flues during the Industrial Revolution. In the first experiments, only cylindrical pipes with very long aspect ratios were of interest. Fairbairn's [29] study, the first of its kind, investigated the effect of tube strength with respect to variations in length, diameter, and wall-thickness. The empirical expression Fairbairn found for the strength of the tube is

$$P_c = C\frac{w^{2.19}}{LD}, \tag{2.1}$$

where P_c is the collapse pressure, w is the wall thickness, L is the length, D is the diameter, and C is an experimentally determined constant [29]. Due to manufacturing limitations, the cylindrical models tested were not uniform in wall thickness or roundness [12].

Basset [4], Bryan [7], Carman [10] and Stewart [55] predicted theoretically

the elastic instability limit for infinitely long cylinders using energy methods. Basset pointed out that the correct mathematical expressions for the potential energy terms were not known due to the mathematical definition of the problem. While an approximation can be made, the exact energy terms cannot be defined.

Carman [10, 13, 11] found that there is a critical length above which the collapse pressure is a constant and no longer dependent on the length of the tube. Carman [11] ran an extensive set of experiments on shorter length tubes, varying the ratio of w/D for different diameter tubes of steel, brass, aluminum, hard rubber, and glass. It is important to note that the experimentally determined collapse pressure for a given tube design was not repeatable because the manufacturing procedures at that time were not capable of producing repeatable tubes.

Using energy methods, Southwell [52, 53, 54] derived an expression for the elastic instability limit with a dependence on mode number

$$P_c = 2E\frac{w}{D}\left[\frac{\pi^4}{16n^4(n^2-1)}\cdot\frac{D^4}{L^4}+\frac{1}{3\nu^2\left(M^2-1\right)}\cdot\left(1/\nu^2-1\right)\frac{w^2}{D^2}\right], \tag{2.2}$$

where E is the elastic modulus, ν is Poisson's ratio, and M is the total mass. This expression yields multiple solutions, (i.e., a family of curves, one curve for each mode number) for a given length and wall thickness, see Fig 2.2, which contains a plot of P_c versus L, for a single set of values for E, ν, M, and w. Mode 2 ($n = 2$, the lowest mode) occurs when the cross-section becomes flat and exhibits two lobes. Mode 3 ($n = 3$) occurs when the cross section contains 3 lobes that are ideally equally spaced and so on. As can be seen in the figure, as the pressure in raised for a given tube design, the mode number and collapse pressure are given by the curve with the

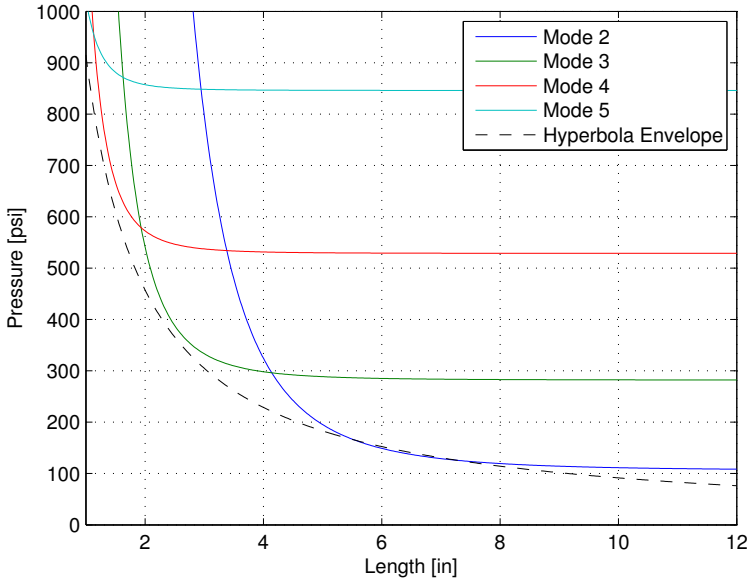

Figure 2.1: Family of curves from Southwell Theory (solid lines) and hyperbola envelope (dashed line) for the conditions of $E = 16.6 \times 10^6$ psi, $\nu = 0.33$, $D = 1$ in and $w = 0.013$ in.

lowest pressure at the given value of L. Southwell also found an approximation (for easier calculation) to these curves by enveloping the curves with one hyperbola (see Fig. 2.1), which is

$$P_c = \frac{8\sqrt{6}\pi}{27} \frac{E}{(1-\nu^2)^{3/4}} \frac{(w/D)^{5/2}}{L/D}. \tag{2.3}$$

Southwell's investigation gave the first complete theoretical explanation of the lobes into which the model collapsed.

Careful experiments performed by Cook [18] validated the theoretical prediction from Southwell [53]. Additionally, Southwell and Cook [18, 19] concluded that tubes with infinitely low ratios of L/D could not collapse purely by this instability. In fact, von Sanden and Günther [51] found through a theoretical investigation that the collapse of a very short tube, with $L/D < 0.2$, is brought on by high-stress regions adjacent to the supports exceeding the proportional limit and causing the

tube to fail by yielding.

R. von Mises [59] was the first to develop a theory for the collapse of short tubes under both axial and radial loading conditions. Until this point, only radial loading had been considered [51]. The theory from von Mises, considering only simply-supported end conditions, was derived from the theory of elasticity. His result is shown below:

$$P_c = \left[\frac{1}{3}\left[n^2 + \left(\frac{\pi D}{2L}\right)^2\right]^2 - 2\nu_1 n^2 + \nu_2 \frac{2E}{1-\nu}(w/D)^3 + \frac{2E(w/D)}{[n^2(\frac{2L}{\pi D})^2 + 1]^2}\right] \frac{1}{n^2 - 1 + \frac{1}{2}\left(\frac{\pi D}{2L}\right)^2}, \tag{2.4}$$

where

$$\mu_1 = \frac{1}{2}\left[1 + (1+\nu)\,\rho\right]\left[2 + (1-\nu)\,\rho\right], \tag{2.5}$$

$$\mu_2 = (1-\rho\nu)\left[1 + (1+2\nu)\,\rho - \left(1-\nu^2\right)\left(1 + \frac{1+\nu}{1-\nu}\rho\right)\rho^2\right], \tag{2.6}$$

and

$$\rho = \frac{1}{n^2\left(\frac{2L}{\pi D}\right)^2 + 1}. \tag{2.7}$$

Because it was difficult without computers or calculators to evaluate the complex expression he derived, he also developed approximations to the equation [59, 61].

In the early 1930s, the US Navy became interested in applying the knowledge of the collapse of shells to submarine design. Experiments conducted at the U.S. Experimental Model Basin by Saunders and Windenburg [51, 61] were compared to the theoretical predictions of Southwell [52, 53, 54] and von Mises [59] and were used to develop new empirical formulas for the collapse pressures of cylindrical shell structures of low aspect ratio. They found that the von Mises prediction was the most accurate of the theories. Windenburg et al. [51, 61] also studied the effect of

imperfections in the circular cross sections of the cylindrical models and found that almost no reduction in the collapse pressure occurs if variations in the radius of the cylinder at all points do not exceed the wall thickness of the model.

Further research was put forth by Sturm [56], who provided a very rigorous derivation of the collapse pressure of a cylindrical shell under radial and axial loading. The cases for fixed end conditions were derived from the stress equilibrium equations and are shown below:

$$P_c = rKE\left(\frac{w}{D}\right)^3 = \left(K_1 + K_2\frac{D^2}{w^2}\right)E\left(\frac{w}{D}\right)^3, \tag{2.8}$$

where

$$K_1 = \frac{2}{3}\frac{n^2\{n^2\lambda_2^2 - \nu(\lambda_2 - 1) - 1\} + \frac{\alpha_2 - 1 - \nu}{\alpha_2\lambda_2}[n^2\{1 + (\lambda_2 + 1)(2 - \nu)\} - 1]}{F_2(1 - \nu^2)}, \tag{2.9}$$

$$K_2 = \frac{2}{\alpha_2^2 F_2}, \tag{2.10}$$

$$F_2 = n^2 - 1 + \frac{1}{\alpha_2^2} - \frac{\nu}{\lambda_2\alpha_2} + \frac{I}{R^2(1 - \nu^2)w\lambda_2\alpha_2}[n^2\{1 - (\lambda_2 + 1)(2 - \nu)\} - 1][\alpha_2 - 1 - \nu + (1 - \frac{P_a R}{Ew})\{\alpha_2(1 - \nu^2) - (1 + \nu)^2\}], \tag{2.11}$$

$$\lambda_2 = \frac{\pi^2 R^2}{n^2 b^2 L^2} - 1, \tag{2.12}$$

$$\alpha_2 = \frac{n^2 b^2 L^2}{\pi^2 R^2} - 1, \tag{2.13}$$

$$r = \frac{F}{F + \pi^2 R^2/2L^2}, \tag{2.14}$$

$R = D/2$ is the radius, I is the moment of inertia, P_a is the pressure load on the ends, and $b \cong 0.664$ is the constant which is evaluated from the end conditions. Sturm verified his theory experimentally.

Finally, in the late 1990s to present day, research has been conducted on cylindrical models to understand the pressure wave pulses generated by the collapse of cylindrical shell structures [28, 43, 58, 38, 22], the collapse propagation along a long tube [38, 22], and the examination of the effect of defects in the cylindrical shell structures [30, 28, 43, 41, 22].

Park and Kyriakides [43] studied the collapse of stainless steel cylinders that were dented to various degrees. The dents reduced the local resistance to collapse, and larger dents were found to lower the collapse pressure due to the effect on the deformation of the cross-section of the cylinder. Dyau and Kyriakides [28] experimented with the propagation pressure of long cylindrical shells under external pressure. A long cylindrical shell model with a local imperfection can lead to a local collapse when exposed to external pressure. The propagation pressure is defined as the lowest pressure at which the local collapse will propagate.

Turner [58] conducted experiments with thin-wall glass spheres in order to determine the influence of failure on pressure waves. The models were forced to fail using a mechanical indentation device. The results from these experiments were compared to a computational fluid-structure interaction model and had reasonable agreement.

2.2.2 Present Work

Due to both the large amount of deformation in the solid material (small linear deformation assumptions do not apply) and the large motion of the fluid-structure

interface, the process of the implosion (after the implosion is initiated due to the elastic instability) is not well understood or predicted. The time history of the pressure waves generated from the collapse of the structure is not easily predicted theoretically or numerically.

The research described in this chapter seeks to expand on the previous studies. Three laboratory-scaled experimental studies were conducted to understand the generation of pressure waves during the collapse process for cylindrical shell structures immersed in a high-pressure water environment. The first study explores the effects of model geometry and material on the implosion of models that collapse in a mode 2 shape. In the second study, mode 2, 3 and 4 implosions are compared for models created with the same 25.4-mm diameter brass-260 tube stock and lengths chosen such that the available energy of the implosion (P_cV, where P_c is the ambient collapse pressure and V is the volume of air in the cylindrical shell structure) is constant; shorter cylindrical shell structures (with lower internal volume, V) require higher ambient pressures (P_c) to become elastically unstable than for longer cylindrical shell structures (with larger V). In the final study mode 2 and 4 implosions are compared for models made from brass 260 alloy tube stock with two diameters and lengths such that the constant available energy of the implosion (P_cV) is the same for both model designs as are the collapse pressure (P_c) and the volume of air inside the cylindrical shells (V). The dynamic pressure waves generated by the implosions were compared within these three studies, and high-speed movies provided simultaneous information about the structural deformation and motion during the implosions.

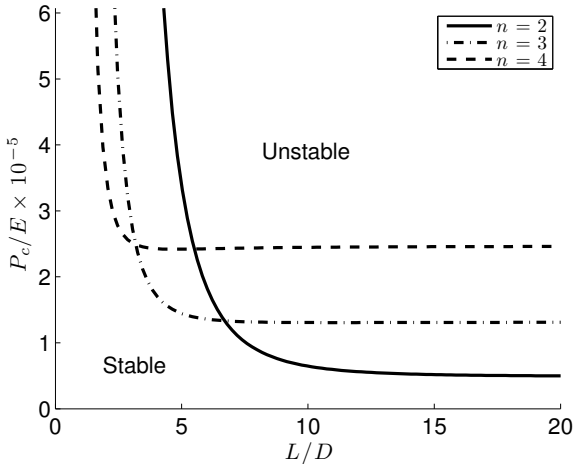

Figure 2.2: Limiting pressure (P_c) over the elastic modulus (E) for the elastic stability limit versus model aspect ratio (tube length (L) over tube outer diameter (D)) for radial and axial loading of a cylindrical shell structure with fixed end conditions, for $w/D = 0.022$, wall-thickness to diameter ratio. (Theory from Sturm [56]).

2.3 Experimental Details

Two types of experiments are conducted to study the collapse of cylindrical shell structures in high-pressure water. The first is natural implosion, which occurs when the ambient pressure in the experimental facility is raised above the elastic instability limit of a given geometry and material of a hollow cylindrical shell structure. Once the elastic instability limit is reached, the model becomes unstable and begins to collapse inward. The mode in which it collapses to is determined by the theory given in Sec. 2.2. The second experiment consists of explosion-induced implosions (to be discussed in Chapter 3).

Both experiments are conducted in the high-pressure experimental facility (Sec. 2.3.1). The cylindrical shell models that are used in both experiments are fabricated from thin-walled brass and aluminum hollow cylinders (to be discussed in Sec. 2.3.2). For both experiments, high-frequency pressure measurements are

taken with piezoelectric pressure sensors (Sec. 2.3.3), and high-speed photography is used to understand the implosion process (Sec. 2.3.4).

2.3.1 High-Pressure Experimental Facility

The implosion experiments were conducted in a steel high-pressure tank that consists of a vertically oriented cylindrical middle section (height 0.85 m, internal diameter 1.77 m and wall thickness) capped by "elliptically" shaped top and bottom sections, see Fig. 2.3 (a) and (b). The maximum internal height of the tank is 1.77 m. The tank is rated for static internal pressures up to 40 bar (gauge). There are 10 window ports with diameters of 10.2 cm in the tank walls; eight of the ports are located on the circular horizontal mid-plane of the tank, while two ports are located on the top, see Figs. 2.3 (b) and (a), respectively. During the experiments, three of the ports along the mid-plane of the tank were fitted with glass windows while the other seven were fitted with steel plates. There are also two 50.8-mm diameter openings, one in the top of the tank and one in the bottom. The opening at the bottom is fitted with a ball valve and is used for draining the tank. The opening at the top is fitted with a piping tree used for filling the tank with water and high-pressure nitrogen gas. The nitrogen gas was used to increase the pressure of the air above the water surface of the tank. The pressure in the water at the free surface inside the tank is the same as that in the air-nitrogen gas while, due to the hydrostatic pressure gradient, the pressure at the bottom of the tank is about 0.18 bar higher due to the hydrostatic pressure gradient. In all cases herein the

pressure in the nitrogen gas is reported as P_c.

The piping tree at the top of the experimental facility, schematically shown in Fig. 2.3 (a), is connected to the water inlet opening at the top of the tank. The piping tree includes openings for the nitrogen gas inlet and gas outlet (not shown). The inlet and outlet are controlled by two solenoid valves. The system was designed so that supplying electrical power to both valves opens the inlet and closes the outlet, thus allowing nitrogen gas to enter the facility and increase the ambient pressure. When power is not supplied to the valves, the inlet valve is closed and the outlet valve is open, allowing the nitrogen gas to leave the facility, thus decreasing the ambient pressure in the facility to that in the laboratory. Additionally, there are two ambient pressure sensors connected to the piping tree. The first one is a slow-response pressure transducer (Honeywell, Model TJE, Range 0 to 1,000 psig, resolution 1 psi) that is read by the data acquisition computer and a digital read-out box. The second pressure sensor is a mechanical dial sensor, for back up. Finally, there is a pressure-relief safety valve, which would be opened if the ambient pressure inside the facility is greater than 41 bar.

A quick-opening manhole on the side of the tank (not shown) allows for access to the interior for the placement of models and pressure probes. The models and measurement equipment were suspended inside the tank on fishing lines (monofilament nylon, rated for a tension load of 178 N), which were attached to 12 eye bolts welded to the inside surface of the tank. Cables for the pressure sensors entered the tank via high-pressure feed-through fittings that were placed in ten 25.4-mm-diameter couplings located on the bottom of the tank.

It is important to consider acoustic reflections inside the tank during the implosion experiments. If an imaginary sphere of radius 0.885 m were centered inside the tank, it would touch the tank walls along a circle at the mid-plane of the cylindrical middle section of the tank and at single points on the top and bottom. The remaining parts of the internal surface of the tank are farther than 0.885 m from the tank center. (The longest distance from the center to a point on the wall is ≈ 0.92 m.) Given a sound wave speed in water of 1482 m/s at 20° C, the acoustic reflection time for a wave traveling from the center of the tank to the closest points on the tank wall and back to the center is approximately 1.19 ms. However, since the remainder of the internal surface is farther from the tank center and since the tank wall internal surface normals are not directed toward the center, most of the energy from spherical pressure waves generated at the center of the tank return after multiple reflections with reduced amplitude and spread out in times greater than 1.19 ms. Reflections from the internal surface of the tank come back with a positive amplitude while reflections from the free surface return with a negative amplitude.

2.3.2 Cylindrical Shell Structures: Brass, Aluminum

The cylindrical models were assembled from thin-walled tubes, end caps, washers, and screws. Fig. 2.4 shows a schematic drawing of the arrangement of the tube and end caps. To construct a model, the tube was first cut to length, L_t, using a lathe. To mount the tube in the lathe without deformation from the clamping pressure, a collet with a diameter slightly larger than the outer diameter of the

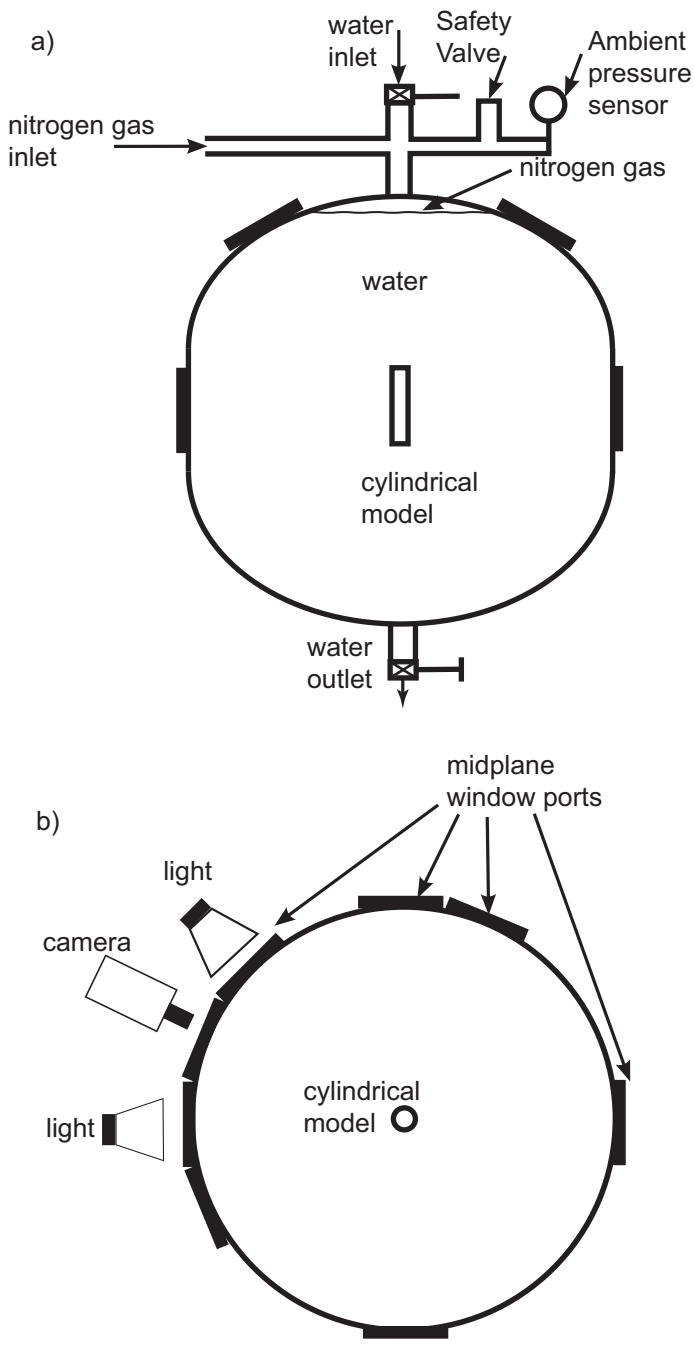

Figure 2.3: Experimental facility: (a) Steel high-pressure tank with piping tree shown on top. There are 10 window ports and a quick-opening manhole. Solenoid valves control the flow of compressed nitrogen gas into the facility. (b) Schematic showing the set up of the camera and lights. This is a plan view of the experimental facility. The circle at the center of the tank shows the position of the cylindrical model. The camera views the implosion event through one of the 8 window ports on the midplane of the facility. Two high-intensity flood lamps (650 W) are placed at the two windows adjacent to the one used for the camera. The remaining window ports have steel plates installed.

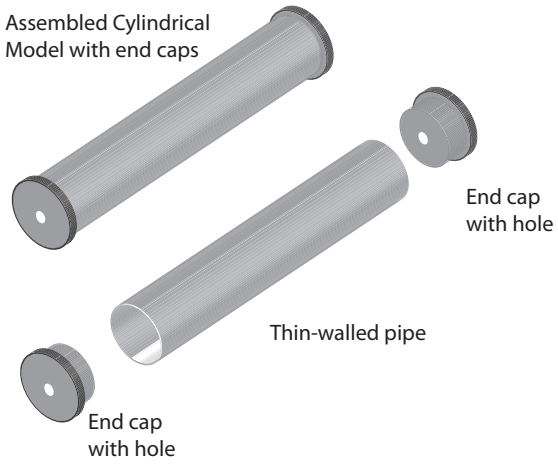

Figure 2.4: Schematic of Cylindrical Models. A tube is first cut to length, $L_t = L + D_o$, where D_o is the outer diameter of the tube, L_t is the cut length, and L is the length of air inside the cylindrical model, measured endcap to endcap. Endcaps are fabricated that have a clearance fit with the inner diameter of the model and have a penetration depth of $0.5D_o$.

tube was used with a thin layer of tape ensuring a snug fit around the tube. The collet was used to insure that the pressure holding the piece in the lathe was evenly distributed. The cut was performed slowly so the pipe did not bend, and both ends were faced off so the ends of the cylinder are perpendicular to the axis of the tube.

The end caps were fabricated on the lathe from an aluminum 6061 rod that was ≈ 3 mm larger in diameter than the outer diameter of the tube ($D_{rod} = 3$ mm$+D_o$). A hole was drilled through the axis of each end cap and tapped with a 1/4"-20 thread. The diameter of a $0.5D_o$-long portion of each end cap was then cut down to the inside diameter of the tube, D_i, minus a small amount, to yield a clearance fit when the cap was forced into the end of the tube, see Fig. 2.4. Therefore, the total length of each thin-walled tube was $L_t = L + D_o$, where L is the length of the internal air-filed portion of the tube after inserting the end caps. To insure that no water could enter the model through the clearance fit, a small layer of silicon

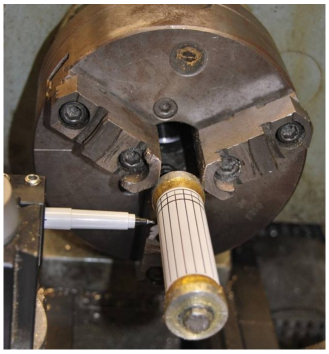

Figure 2.5: Lathe set up for drawing grid lines on a cylindrical model.

sealant was applied to the end cap during installation. After the end caps were installed, a 1/4"-20 drilled-head screw was placed in each end cap and sealed with the silicon sealant. Each screw had a 1/16"-diameter hole through its head in the direction normal to the screw axis for mounting the model in the tank. A thin-layer of white paint was sprayed on the outer surface of the tube between the end caps. An ultrafine black marker was used to draw a finely spaced grid (of squares 6.35 mm by 6.35 mm) on the painted tube surface using the lathe, while spinning it manually (see Fig. 2.5).

Each cylindrical model was mounted vertically in the center of the tank using fishing lines threaded through the holes in the two screw heads on the model and the eye bolts on the inside surface of the tank. The cylindrical models were primarily constrained in the vertical direction, so the model could move horizontally and deform freely during the implosion event.

The outer diameters of the tubes were measured both before and after the tubes were cut to length. In the first experiments, the diameters were measured photographically and in the later experiments they were measured using a microm-

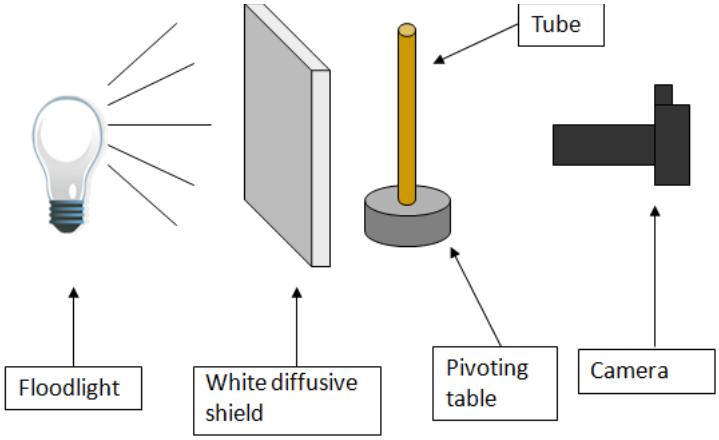

Figure 2.6: Schematic of Out-of-Roundness test set up.

eter. A reference line was first drawn onto the tube along its axis before being cut-to-length. The diameter was measured at axial distances spaced 150 mm apart before the tubes were cut and 25 mm apart after they were cut. These measurements were made at 12 equally spaced angular positions around the tube. Comparison of the measurements before and after cutting revealed that there was no measurable change in tube diameter or cross-sectional shape caused by the cutting process.

Fig. 2.6 shows a schematic of the photography technique for measuring the diameter of the tube. The tube, with one end cap assembled without silicon, was attached to a pivoting table with angular tick-marks. A flood light was used to back-light the tube with a white diffusive sheet between the flood lamp and the tube in order to create uniform lighting. A digital SLR (Nikon D1X) camera with a telephoto lens (200 mm focal length) was placed on the opposite side of the tube. The telephoto lens was used to move the camera farther away from the model and thus reduce distortion of the geometry in the images. Still images were taken at angular positions around the tube and at axial distances along the tube described

in the previous paragraph. The majority of pixels in each frame contained the entire diameter of the tube to increase the sensitivity. A calibration piece of known diameter was taken before each set of images. Once the images were taken, the still frames were post-processed using a gradient-based edge detection technique in Matlab. This photographic method of measuring tube diameter was sensitive to the camera focus and the threshold values chosen for the edge detection algorithm. This method was also found to be time consuming and not more accurate than simply measuring the diameters with a micrometer.

The digital micrometer was used instead of calipers, because the micrometer contact surfaces consist of two parallel plates. These plates allowed the measurer to insure that the measurement was done perpendicular to the curvature of the tube, because the parallel plates had to be positioned tangent to the tube wall. The micrometer chosen was designed to apply constant force during measurement to insure that the tube was not deformed while being measured and that the measurements were repeatable. The measurement time was much shorter than that of the photographic technique.

Attempts to measure the tube wall thickness were made using both an ultrasonic device and a micrometer with a ball-tip attachment. The ultrasonic device (GE Krautkramer CL 5) was used once the paint and grid were present on the surface of the cylindrical model and measured wall thicknesses at the points of intersection of the finely spaced grid. The ultrasonic device sends a sound wave into the material through a probe placed on the surface of the model. The sound wave is reflected back into the probe after hitting the inner tube surface due to the change

in acoustic impedance of the metal to air interface. Based on the known wave speed in the material and travel time of the wave, the thickness (half of the distance traveled) is determined. The thin layer of paint is ignored based on the low acoustic impedance of the paint compared to the metal. The accuracy of the ultrasonic gauge is calculated to be ± 0.0025 mm (or 0.0001 in). The ultrasonic measurements did not work well, probably because of the high surface curvature and thin tube wall (w). These factors resulted in an inability to determine that the probe was placed perpendicular to the surface of the cylindrical model and erratic results were obtained. These measurements were also time consuming.

Given the difficulties with the ultrasonic measurement device, a micrometer with a ball-tip attachment was used to measure the wall thickness of the cylindrical models. The ball tip was placed on the inside surface of the tube to allow for one point of contact on the interior of the tube, while the outside surface was in contact with the parallel plate consistent with standard micrometer design. However, measurements could only be made at the tube ends because of the physical limitations of micrometers. Since the end caps penetrate $0.5D_o$ into the tubes, the micrometer measurements are not made over the central air-filled section of the tube. Measuring the thickness on the tubes after they were cut gave insight into the thickness distribution along the manufactured tube stock from which the tubes were cut. The wall thicknesses were measured near each end of the tube at 3 locations (separated by increments of 6.35 mm along the axis) and at increments of 20° around the tube.

2.3.3 High-Frequency Pressure Measurements

The ambient water pressure in the tank was obtained from measurements of the pressure of the nitrogen gas using a slow-response pressure transducer (Honeywell, Model TJE, Range 0 to 1,000 psig, resolution 1 psi). This sensor was calibrated by the manufacturer before and after the experiments were performed. The calibration curve changed by less than 0.3% at typical operating pressures (7 bar to 25 bar). Due to the hydrostatic pressure gradient in the water, the pressure at the model is about 0.08 bar higher than the pressure in the nitrogen gas. In the results, the gas pressure is reported as the ambient pressure in the tank.

The dynamic pressure waves in the water were measured with up to 16 underwater blast sensors that use a Tourmaline crystal sensor (PCB Piezoelectronics, Inc. models #138A02 and 138A01). For the natural implosion experiments, eight of these sensors were attached to a thin stainless steel support frame so that the sensing elements formed a ring of radius $1.5R_o$, where $R_o = D_o/2$, around the centerline of the model, see Fig. 2.7. The support frame was suspended in the tank using fishing lines. The pressure sensors have a rise time of 1.5 microseconds (μs) and a useful range of $\pm$138 bar. Each sensor was connected to a signal conditioner that gives a $\pm$10 volt analog output signal. The signals were then sent to simultaneous sample-and-hold Analog-to-Digital (A/D) converters with a sample rate of 2 MHz per channel. A program in LabView was used to record the final output data into the computer and convert the voltage signal into units of pressure.

For the natural implosions, the ambient pressure at which a given model will

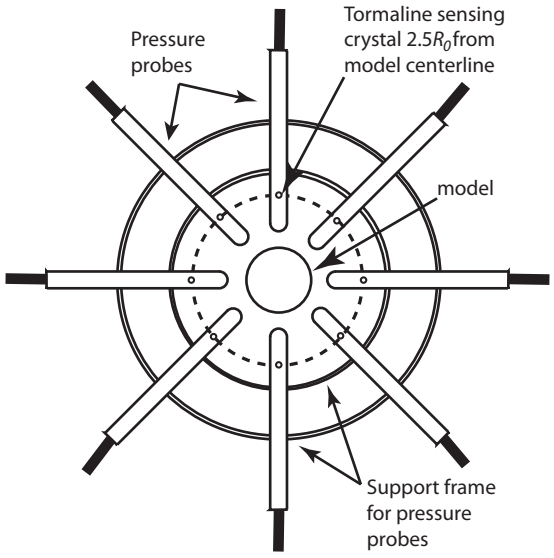

Figure 2.7: A schematic plan view showing the orientation of the cylindrical model in the tank surrounded by the eight meridian plane pressure sensors. In this schematic, the dots represent the position of the tourmaline crystals located inside the pressure sensors. The sensors are placed at a radius of $2.5R_0$ away from the center of the cylindrical model, where R_0 is the outer radius of the cylindrical model.

implode is not known precisely. Thus, in order to capture the pressure signals, the A-to-D system operates continuously filling the system memory in a first-in-first-out mode, holding more than 2 seconds of data at all times. Then, when the operator hears a noise from within the tank (the pressure waves hitting the tank walls from within) indicating that the model has imploded, she manually triggers the A-to-D system, which is set to save two seconds of data ending at the moment the trigger was initiated.

2.3.4 High-Speed Photography

The motion and deformation of the model during a natural implosion is recorded with high-speed digital photography, using a Phantom V7.2 camera (Vision Research, Inc) with an 800-by-600-pixel sensor, with a maximum sampling rate of

4800 pps at full resolution. The camera was set to record 27,000 pictures per second (pps) at an image size of 256 by 256 pixels and was post-triggered in the same way as the A/D system. A timing system triggers the A/D recorder and camera simultaneously, so that the pressure signals over the 37-μs period that each image is captured can be examined. The camera is positioned to view the implosion through one of the glass windows in the mid-plane of the tank and the two adjacent windows are used to project light from two 650-W flood lamps onto the model (shown in Fig. 2.3 (b)). The inside surface of the tank was painted black to provide contrast to the painted surface of the models. From the movies of the implosions, both qualitative information and quantitative measurements can be extracted. The qualitative information includes the state of the model at any time. Quantitative measurements include the implosion time of the model and the orientation of the collapsed model with respect to the tank.

2.3.5 Test Procedures

To perform an experiment, the model and pressure sensors were first placed in the experimental facility. The front manhole and drain were closed, and the tank was filled through the 50.8-mm-diameter ball valve in the piping tree at the top of the tank until $\approx$5.7 L of air remained. The water inlet ball valve was closed, and the tank was slowly pressurized with high-pressure nitrogen gas through a solenoid valve in the piping tree. Immediately after the model imploded, anywhere from 2 to 5 minutes after the pressurization process began, the nitrogen inlet valve was

closed and the nitrogen outlet valve was opened to depressurize the tank. After each experiment, the water inlet valve is opened and the tank is drained through the valve at the bottom.

2.3.6 Plan of Experiments

In this chapter, there are three different sets of experiments that will be discussed. Table 2.1 shows the conditions tested for the natural implosion experiments. The columns show the run designation; implosion mode number (n); the tube material; outer diameter (D) and wall thickness (w); the ambient implosion pressure (P_c); and available energy (P_cV) for each implosion test. The run designation starts with an "A" for aluminum or "B" for brass and this is followed by the observed mode number of the implosion ("2", "3" or "4"). For the brass models, the next symbol is a "D" for diameter followed by numbers giving the outer diameter of the tube truncated to the nearest millimeter. For the aluminum models (all of which had an outer diameter of 38.1 mm), the next symbol is an "A" followed by either a "2" for the 2024 alloy or "3" for the 3003 alloy. Finally, all run designations end with the run number.

It was found that the linear theory (from Sturm [56]) for predicting the collapse pressure and mode number was not always accurate, probably due to the slight differences between the tube end conditions used in the theory and those used in the models in the experiments. Therefore, several cylindrical models of different lengths were constructed and imploded to empirically determine parts of the linear

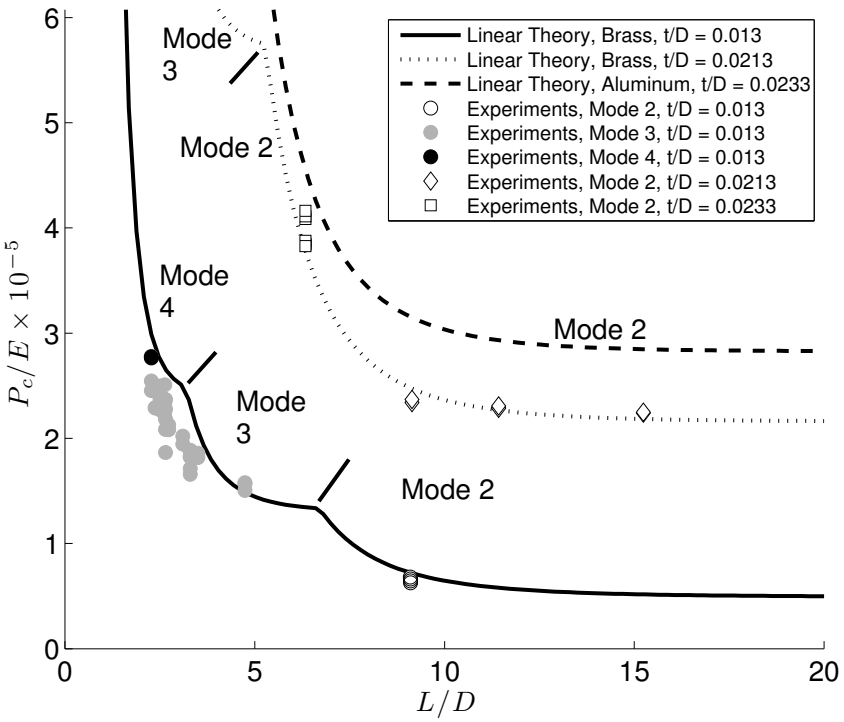

Figure 2.8: The linear theory (from Strum [56]) curves are shown for the three w/D cases that were tested in this study. Each circle represents one experimental run with a $w/D = 0.013$ at a given L/D that yielded a collapse pressure, P_c/E, as shown. The diamonds show the experimental runs with a $w/D = 0.0213$ at various L/D values. The squares show the experimental runs with $w/D = 0.0233$ at various L/D values. When the theory curve is very steep, the discrepancies between the theory and experiment are clearly seen; however, when the curve is less steep, there is a greater agreement between the theory and experiment.

theory curves for small L/D. Fig. 2.8 shows the linear theory elastic instability limit for the three different thickness-to-diameter (w/D) ratios used in this study. Points representing single experimental runs are plotted to show the difference in the linear theory and what was observed in the laboratory. From these experiments, cylindrical model geometries were chosen for the constant available energy experiments.

The first set of experiments explored mode 2 implosions on cylindrical models of different materials and geometries (Sec. 2.4.1). As seen in Fig. 2.8, mode 2 implosions occur when the length-to-diameter ratio of the model (L/D) is sufficiently large. Also, for mode 2, P_c becomes nearly constant when L/D is large. The models that underwent mode 2 implosions are B2D25 ($L/D = 9.1$), B2D16 ($L/D = 9.2$), A2A2 ($L/D = 6.3$), and A2A3 ($L/D = 6.3$).

The second study explored mode numbers 2 through 4 for cylindrical models that have the same available energy (P_cV) and the same cross-sectional geometry (see Sec. 2.4.2). Here models were created from the same tube stock but with different lengths. As can be seen from Fig. 2.8, as the model length is reduced the mode number of the instability increases as does P_c. To explore the effect of mode number, model lengths were chosen such that the energy available for the implosion, P_cV, was the same for all models. Fig. 2.9 (a) shows the theoretically computed P_cV versus L/D for the w/D of the tube stock used in this set of experiments. As can be seen, a horizontal line can be draw across at one value of P_cV that correspond to different values of L/D. The models used for these experiments were B2D25 ($L/D = 9.1$), B3D25 ($L/D = 3.3$), and B4D25 ($L/D = 2.3$). The available energy for these cylindrical models is about 80 N-m, see Table 2.1.

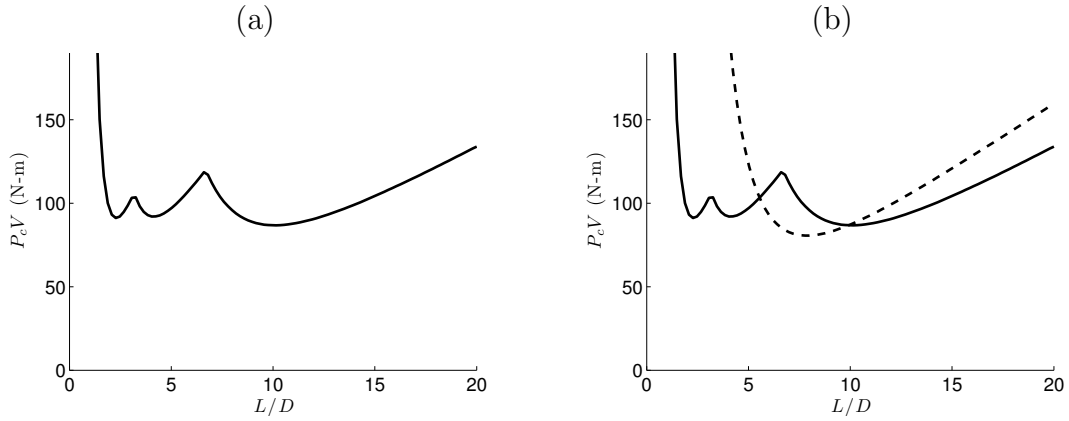

Figure 2.9: (a) Theoretically computed P_cV versus L/D for $w/D = 0.013$. This curve was computed from the solid black curve in Fig. 2.8 by multiplying P_c/E by E and V, the volume of the air inside the tube. (b) Theoretically computed P_cV versus L/D for $w/D = 0.013$ (shown in solid black) and $w/D = 0.0213$ (shown as a dashed black line). The solid black curve was computed from the solid black curve in Fig. 2.8 by multiplying P_c/E by E and V, the volume of the air inside the tube, and the dashed black curve from the dotted black curve.

In the third set of experiments, modes 2 and 4 were compared for cylindrical models having the same available energy (P_cV), while holding the collapse pressure and internal air volume constant (see Sec. 2.4.3) were studied. Two tubes with different diameters and lengths were chosen to hold P_cV constant in this manner. Fig. 2.9 (b) shows the theoretically computed values of P_cV versus L/D for the two different w/D tubes used in this experiment. In this set of experiments, the point of intersection between the two curves gives the L/D and w/D of the models to be tested.The models used for these experiments were B2D16 ($L/D = 9.2$) and B4D25 ($L/D = 2.3$). The available energy for these cylindrical models is about 86 N-m, see Table 2.1.

2.4 Results and Discussion

The results from the first, second and third set of experiments are presented in Secs. 2.4.1, 2.4.2, and 2.4.3, respectively. It is noted that the destructive nature of the experiment requires a new tube to be fabricated for each experiment, which leads to the slight variations from run to run. The error in cutting the length of the tubes is no more than 1 mm. There may be slight non-uniformity in the geometry of the tube stock due to the manufacturing process (extrusion).

2.4.1 Natural Implosions: Mode 2

In this first section of the results, the experiments conducted for the cylindrical shell structures that implode in mode 2 are discussed. For these experiments, four different cylindrical shell geometries and materials were used. Fig. 2.10, Fig. 2.11, Fig. 2.12, and Fig. 2.13 show the pressure records for one representative run for B2D25, B2D16, A2A2, and A2A3, respectively. In each figure, three still frames taken from the high-speed movies were matched in time with three of the key features in the pressure record. The qualitative behavior of the dynamic pressures for each collapse are very similar. The first region is the decrease in pressure caused by the relaxation in pressure on the wall of the cylinder as it moves inward. The second region is a small jump in pressure that occurs before the maximum peak. At this point in time, the walls initially make contact with one another. The final region consists of the second peak, which is the largest, and it occurs when the walls come into complete contact with one another. Appendix A shows the pressure records and movie frames for each experimental run.

Run	Mode n	Material	Outer Diameter D_o (mm)	Wall Thickness w (mm)	Length L (mm)	Collapse Pressure P_c (bar)	Available Energy P_cV (N-m)
B2D25r1	2	Brass	25.4	0.33	231	7.3	81.1
B2D25r2		260				7.1	78.9
B2D25r3						7.5	83.3
B2D16r1	2	Brass	16.6	0.36	152	26.6	80.1
B2D16r2		260				26.5	79.8
B2D16r3						26.9	81.1
A2A2r1	2	Alum	38.1	0.89	241	26.5	661.7
A2A2r2		2024				26.6	664.1
A2A2r3						28.2	704.0
A2A2r4						26.7	666.6
A2A2r5						26.4	659.1
A2A3r1	2	Alum	38.1	0.89	241	28.3	706.5
A2A3r2		3003				28.7	716.6
B3D25r1	3	Brass	25.4	0.33	84	19.4	78.2
B3D25r2		260				18.8	76.0
B3D25r3						20.7	83.6
B3D25r4						21.4	86.4
B3D25r5						21.3	86.1
B4D25r1	4	Brass	25.4	0.33	58	26.1	72.9
B4D25r2		260				28.3	78.9
B4D25r3						28.9	80.4
B4D25r4						27.9	77.9
B4D25r5						31.4	87.7
B4D25r6						31.5	88.0
B4D25r7						31.5	88.0

Table 2.1: A summary of the cylindrical models imploded naturally for the first three experiment sets. The names given have an "A" for aluminum or "B" for brass. The mode number follows, then there is either a "D" for diameter followed by numbers representing the diameter, or for the case of aluminum models, an "A" for alloy followed by "2" for 2024 or "3" for 3003. Finally, there is an "r" representing the run number for the given geometry and material. These names are used in plot legends and plot titles to give a quick reference to the cylindrical models in this table. 25 individual experimental runs were performed on 8 unique cylindrical models.

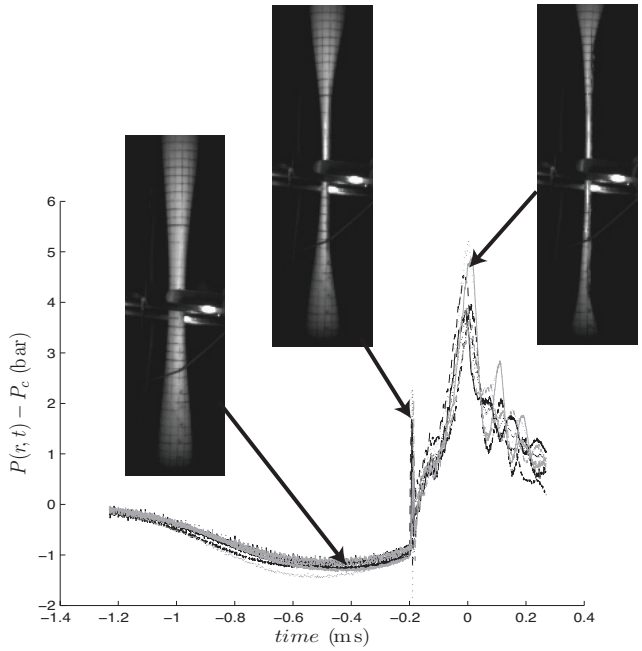

Figure 2.10: Each line represents one of the eight meridian pressure sensors for B2D25r2. Three still frames from the high-speed video are shown at the times corresponding to the minimum pressure peak, first small positive peak and the maximum positive peak. These still frames give insight into the shape of the imploding model at each time in the pressure record. As the walls close in, there is a drop in pressure. The first small positive peak occurs when the walls first impact each other. The large positive pressure peak occurs when the walls make full contact and the collapse is complete. For a complete set of pressure records and still frames, see Appendix A.

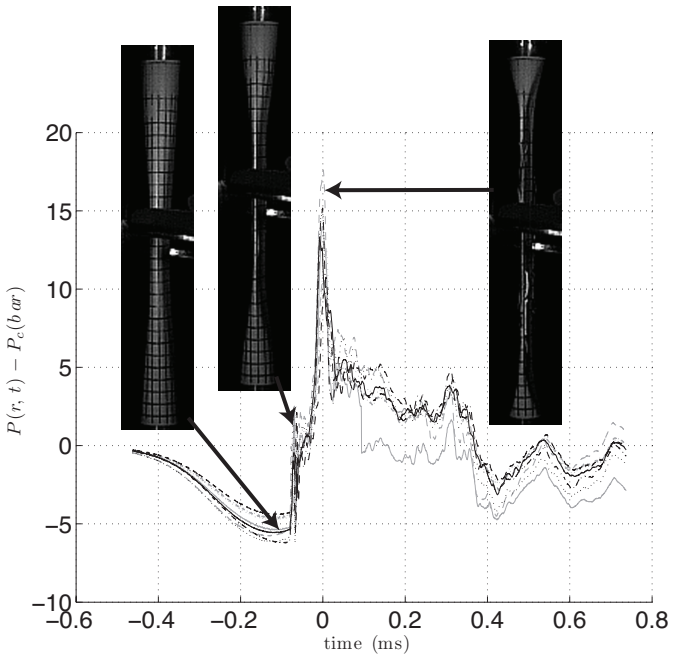

Figure 2.11: Each line represents the signal from one of the eight meridian pressure sensors for B2D16r1. Three still frames from the high-speed video are shown at the times corresponding to the minimum pressure peak, first small positive peak and the maximum positive peak. For a complete set of pressure records and still frames, see Appendix A.

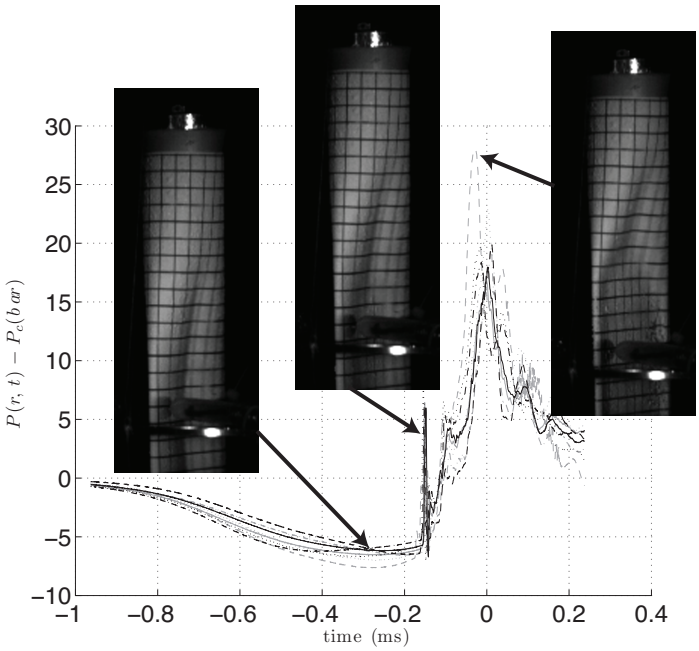

Figure 2.12: Each line represents the signal from one of the eight meridian pressure sensors for A2A2r2. Three still frames from the high-speed video are shown at the times corresponding to the minimum pressure peak, first small positive peak and the maximum positive peak. For a complete set of pressure records and still frames, see Appendix A.

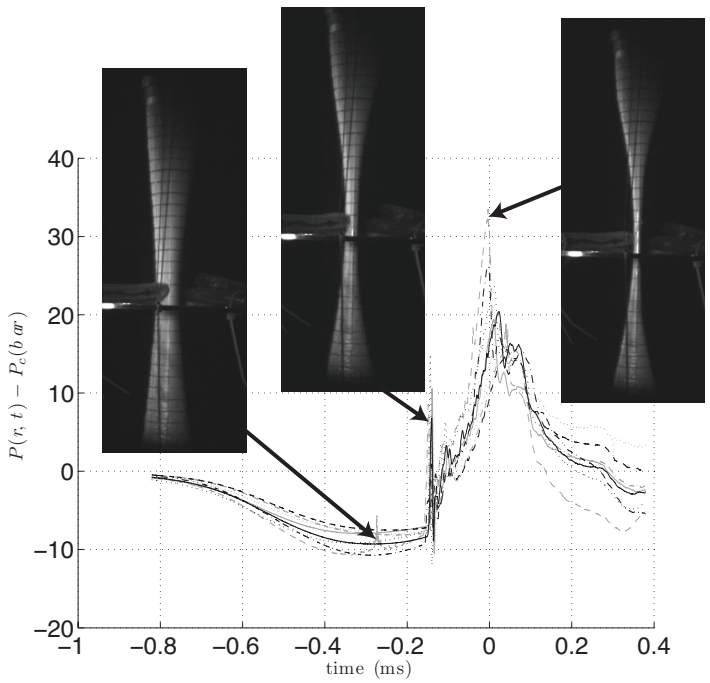

Figure 2.13: Each line represents the signal from one of the eight meridian pressure sensors for A2A3r2. Three still frames from the high-speed video are shown at the times corresponding to the minimum pressure peak, first small positive peak and the maximum positive peak. For a complete set of pressure records and still frames, see Appendix A.

Though the general behavior for the dynamic pressure records is the same for each experimental run, the time scales and pressure scales differ for each cylindrical model design tested. Fig. 2.14 shows one representative set of pressure records for the implosion of each of the four model designs. Each geometry yields a different collapse time and different pressure magnitude and time scales. In each case, the pressure records are shifted in time so that the maximum pressure peak occurs at $t = 0$. The pressure signals for the B2D25r2 model have the smallest amplitude and the longest time scale. The pressure signals for the B2D16r1 model show a higher amplitude than B2D25r1 and the shortest time scale. Finally, A2A2r2 and A2A3r1 are similar and have the highest pressure amplitude and the second longest time scale.

The pressure waves for each of the eight pressure sensors shown in Fig. 2.14 appear to be slightly different. In order to visualize the difference in pressure versus the azimuthal direction, the same pressure data for all experimental runs versus time can be shown in polar coordinates in Fig. 2.16, Fig. 2.17 and Fig. 2.18. The radial direction is taken to be the time, which begins when the pressure wave starts to decrease and ends at the time of the zero crossing after the maximum peak pressure. The azimuthal direction corresponds to the position of the pressure sensors (placed at increments of 45°). The grayscale of the surface gives the amplitude of the pressure wave with respect to time and azimuthal location. The straight line plotted on top of the contour shows the orientation of the final mode 2 collapse, which gives a reference to interpret the pressure contours. The orientation of the collapse was measured from the high-speed movies and the accuracy is ±15°. The angle, $\Delta\theta$,

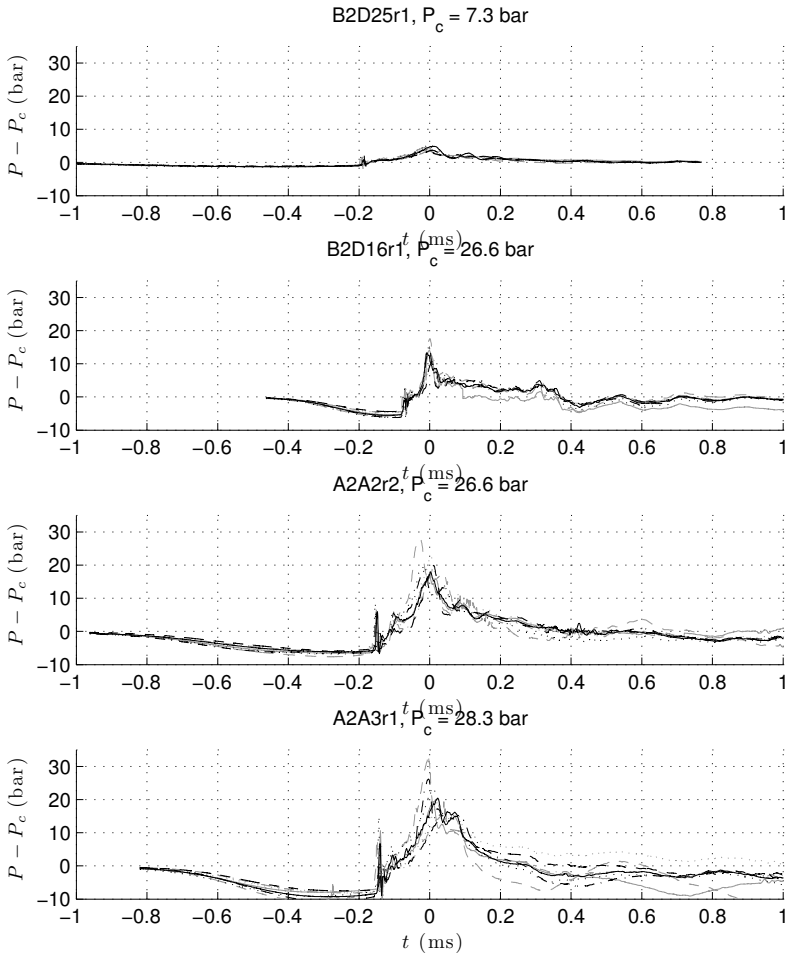

Figure 2.14: To compare the mode 2 occurrences, one representative run is shown for each of the four different cylindrical models collapsing in Mode 2. They are B2D25r1, B2D16r1, A2A2r2 and A2A3r1. Each geometry yields a different collapse time and different pressure magnitude and time scales. In each plot, the time scale is shifted so that the maximum positive pressure peak occurs at time $t = 0$. B2D25r2 has the smallest pressure amplitude of pressure and the longest collapse time. B2D16r1 has a higher pressure amplitude than B2D25r1 and the shortest collapse time. Finally, A2A2r2 and A2A3r1 are similar and have the highest pressure amplitudes and the second longest collapse times.

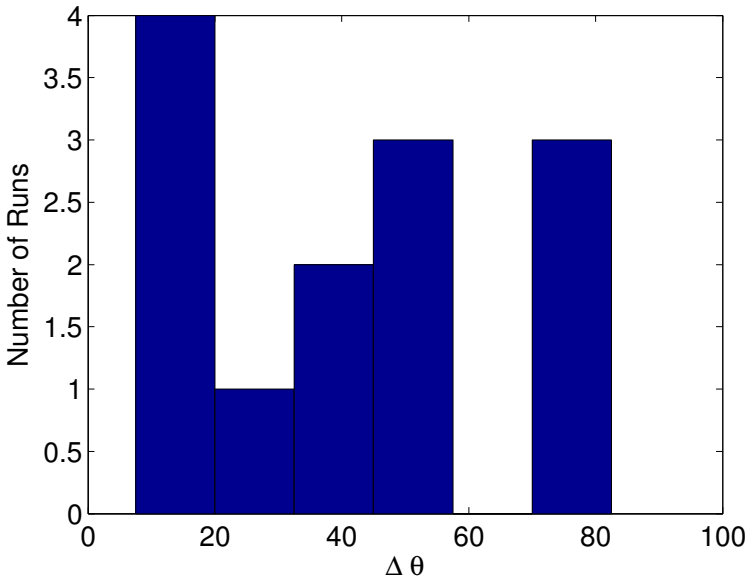

Figure 2.15: Histogram of $\Delta\theta$ obtained during the experiments, where $\Delta\theta$ is defined as the minimum angle between the line formed by the deformed cross-sectional shape of the cylinder and the location of the maximum peak pressure.

is defined as the minimum angle between the line formed by the deformed cross-sectional shape of the cylinder and the azimuthal location of the maximum peak pressure. Fig. 2.15 shows a histogram of $\Delta\theta$ obtained during the experiments. By definition of $\Delta\theta$, the angles can only fall between 0° and 90°. As shown for the four cases, the orientation of the final collapse shape and the peak pressure in the azimuthal direction do not show any correlation.

Because the peak pressure appears to be noisy in the pressure versus time signal (Fig. 2.14), the pressure impulse, the integral of the pressure versus time curve with respect to time, was computed. The black squares, shown in Fig. 2.16, Fig. 2.17 and Fig. 2.18, show the pressure impulse computed for each sensor record integrating only the positive pressure peak. The black diamonds show the total pressure impulse, calculated from the start of the collapse to the zero crossing after

the positive pressure peak. The white circles show the impulse from the start of the collapse to the zero crossing just before the positive pressure peak. Finally, the white diamonds show the amplitude of the minimum (negative) pressure peak. These four metrics are shown clearly in Fig. 2.16 (a). The radial direction corresponds to the magnitude of each of these four metrics. For each of these four metrics, there was no correlation with the orientation of the final collapse shape.

In order to directly compare one run to another and because there was no correlation between azimuthal pressure characteristics and the final deformed shape, an average of the eight meridian plane sensors was taken as the one representative curve for each experimental run, shown in Fig. 2.19.

This experiment is comparable to a cylindrical gas (air) bubble collapsing in water but with a thin-walled metallic membrane. Therefore, it seemed reasonable to scale the pressure signals with similar metrics for a collapsing bubble. The averaged pressure signals, from Fig. 2.19, are scaled by the difference in pressure between the ambient collapse pressure and the initial pressure inside the cylindrical model for the pressure axis and by the characteristic collapse time of a gas bubble in a fluid for the time axis. The scaling used is

$$\frac{P - P_c}{P_c - P_0}, \tag{2.15}$$

for the pressure and

$$\frac{t}{R_i\sqrt{\frac{\rho}{P_c - P_0}}}, \tag{2.16}$$

for the time, where P_c is the ambient collapse pressure, P_0 is the pressure inside the model (ambient pressure), R_i is the inner radius of the shell, and ρ is the density

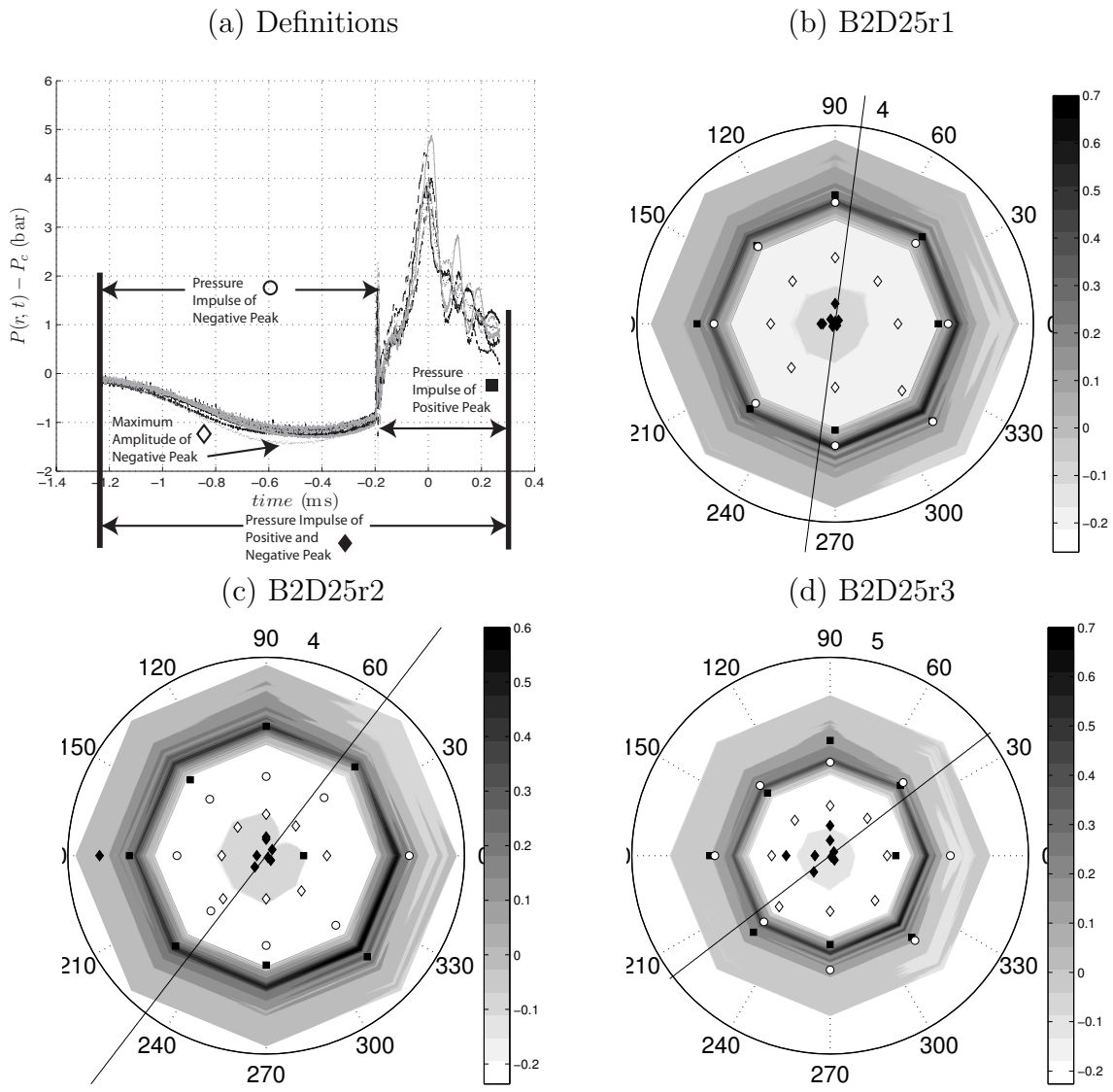

Figure 2.16: The pressure contours for the cylindrical models collapsing in mode 2. The radial direction is time. The azimuthal direction corresponds to the position of the pressure sensors (placed at increments of 45°). The grayscale of the surface gives the amplitude of the pressure wave. The line plotted on top of the contour shows the orientation of the final mode 2 collapse. The black squares show the pressure impulse computed for the positive pressure peak, shown in (a). The black diamonds show the total pressure impulse of both the positive and negative peak, shown in (a). The white circles show the pressure impulse of the negative peak, shown in (a). Finally, the white diamonds show the amplitude of the minimum (negative) pressure peak, also shown in (a). Pressure contours are continued in Figs. 2.17 and 2.18.

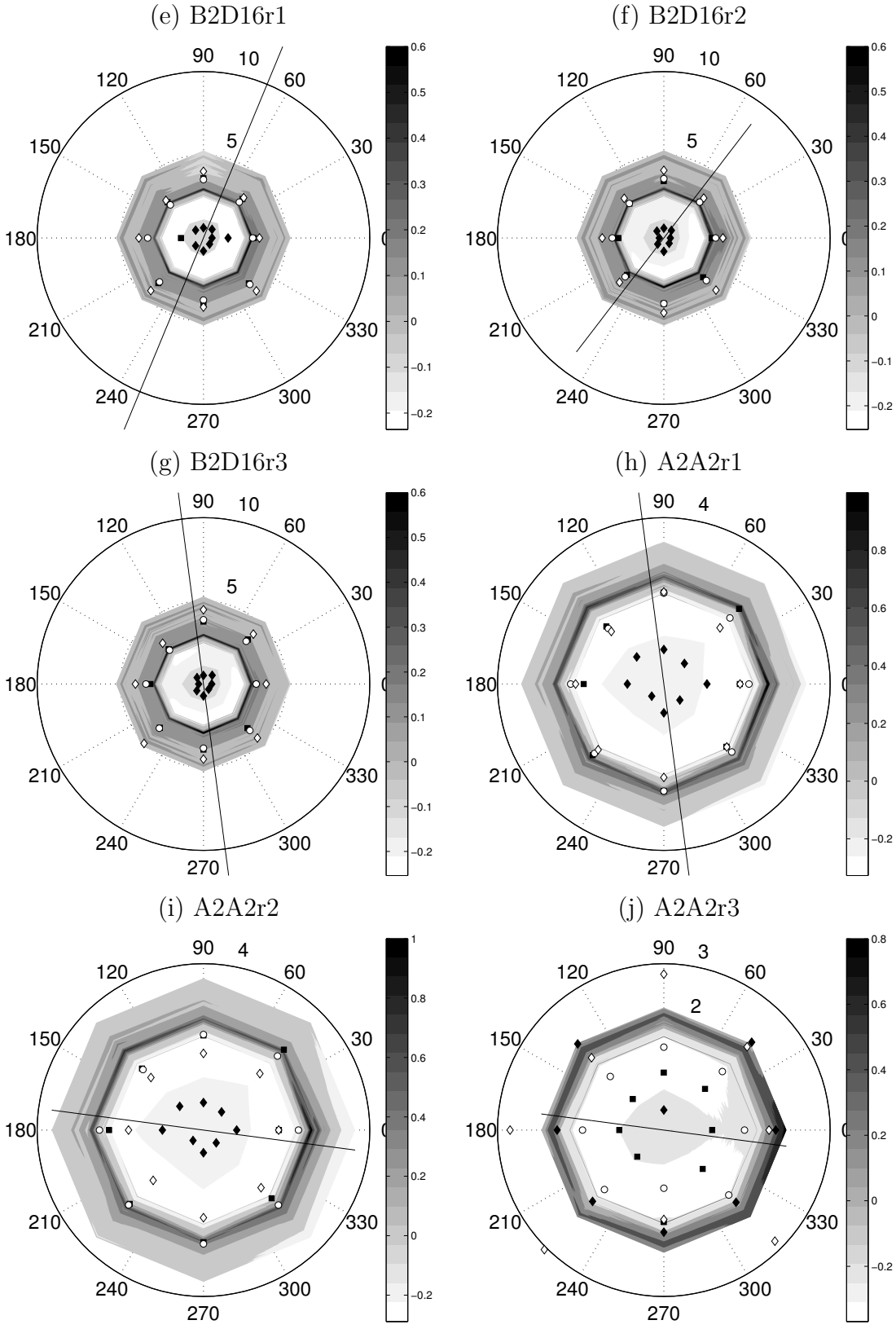

Figure 2.17: The pressure contours for the cylindrical models collapsing in Mode 2, continued.

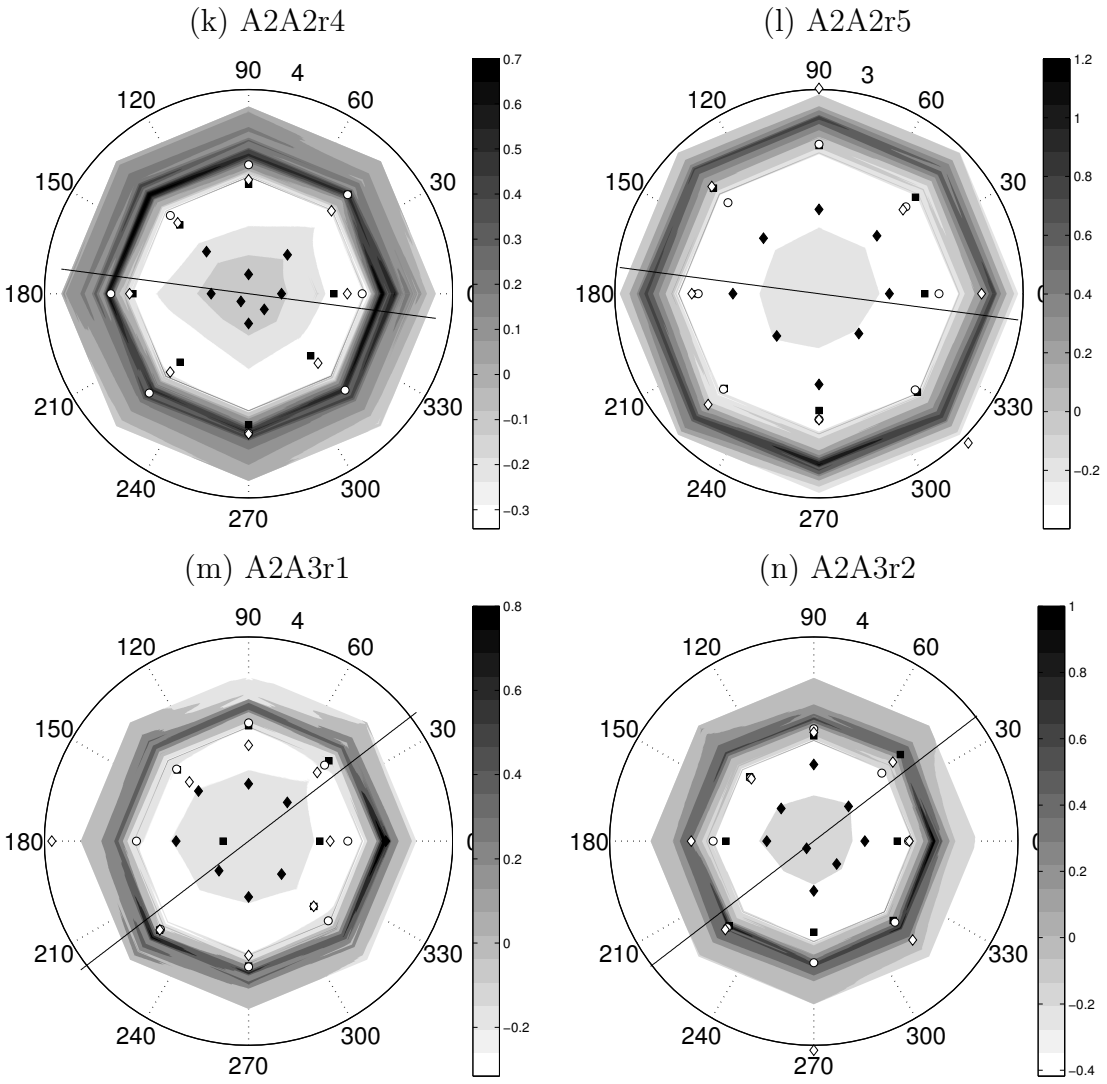

Figure 2.18: The pressure contours for the cylindrical models collapsing in Mode 2, continued.

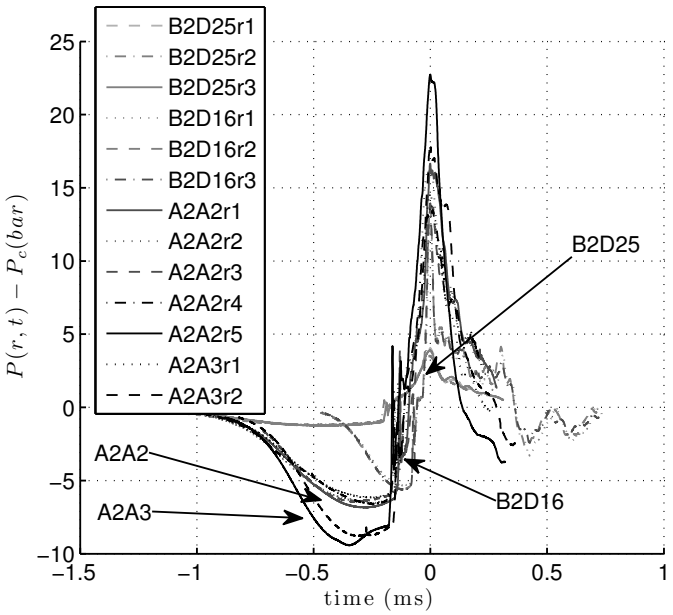

Figure 2.19: Each curve shows the average of the meridian plane pressure sensors for each run. The callouts show how repeated runs for each geometry grouped.

of water. The pressure versus time data from Fig. 2.19 is plotted using the above nondimensionalization in Fig. 2.20. The normalized data has nearly identical non-dimensionalized collapse time from each different experimental run for these mode 2 cylindrical models. The collapse time is defined as the time between the initial pressure drop and the maximum peak. The magnitude of the nondimensional peak pressures range between 0.5 and 0.9, and the minimum value in the dip before the peak ranges between -0.3 and -0.2. The scaling performed on the variables is considered satisfactory judging from the results in Fig. 2.20. Even though the thin-walled shell structure of the undeformed model is much stronger than the gas-fluid interface of a bubble, once the shell structure goes out of round due to the elastic instability, it becomes weak and undergoes large deformations. The success of the scaling in Fig. 2.20 supports the hypothesis that the weak state of the cylindrical

shell during the implosion allows for the hydrodynamic forces to dominate over the stiffness of the structure surrounding the air volume. This indicates that once the cylindrical model collapse is initiated, the metallic structure becomes unimportant and the air cavity collapses as if the structure was not present.

In order to investigate the spread in the dimensionless peak pressures in Fig. 2.20, the dimensionless peak pressure versus the mass ratio was plotted in Fig. 2.21 (a). The mass ratio is defined as the mass per unit length of the tube in the shell structure to the mass per unit length of the water that the structure displaces. The mass ratio was chosen here since, while it is hypothesized that the shell structure is weak during the implosion, structure still has significant mass which might affect the implosion rate and therefore the pressures. Here, the data falls into three groups of mass ratios based on the material and size. The aluminum cylindrical models (which all have the same size, wall thickness and mass per unit length) have the same mass ratio. It is interesting to note the relatively high variation in the peak dimensionless pressure values for the aluminum models as well as the fact that the variation in peak dimensionless pressures for the 3003 alloy cylindrical models fell into the range of the peak dimensionless pressures for the 2024 alloy cylindrical models. The peak dimensionless pressures for the two brass cylindrical models (B2D25 and B2D16) are nearly the same. The values of the dimensionless pressure peaks for the aluminum model implosions (A2A2 ad A2A3) were, on average, higher than the values for the brass cylindrical implosions and the values for the aluminum models have a much larger range.

In view of the larger range in dimensionless peak pressures for the aluminum

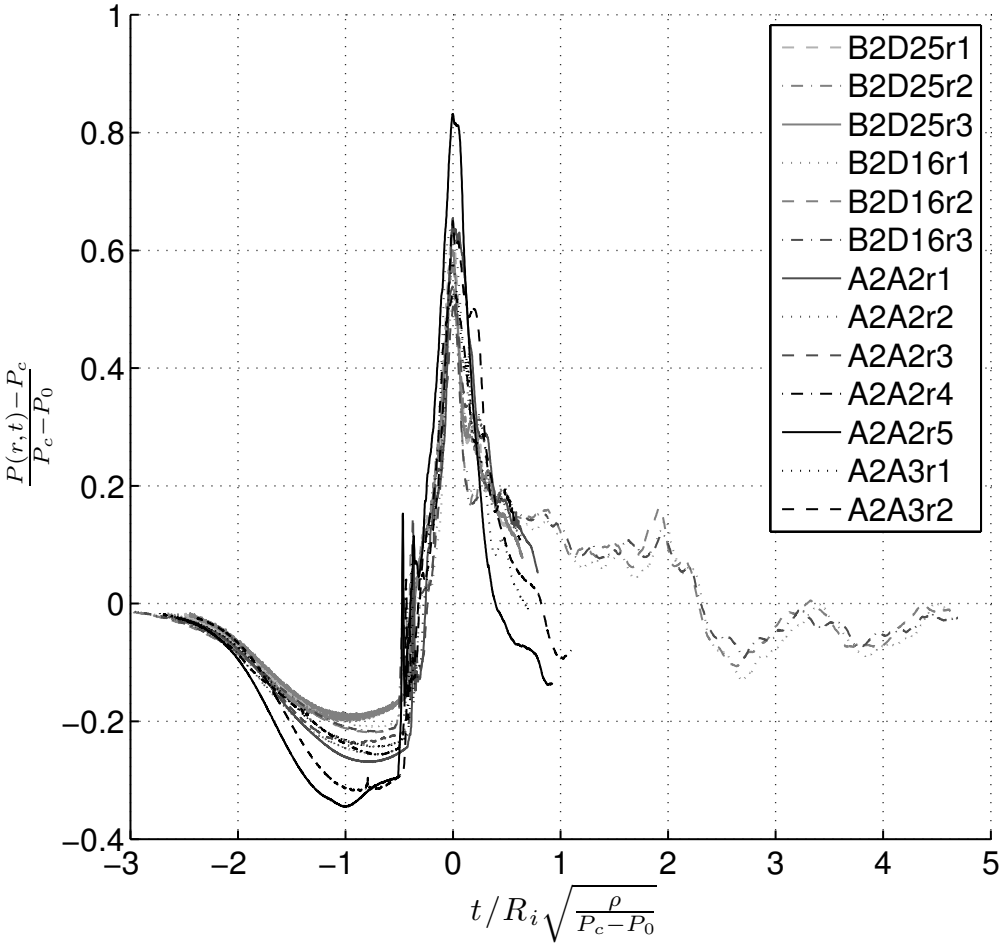

Figure 2.20: Each curve shows the average of the meridian plane pressure sensors for each run. The time (horizontal axis) is scaled in the time axis by the characteristic bubble collapse time, $R_i\sqrt{\rho/(P_c - P_0)}$, and the pressure (vertical) axis by the relative pressure of the ambient collapse pressure and the initial gas pressure inside the structure $P_c - P_0$.

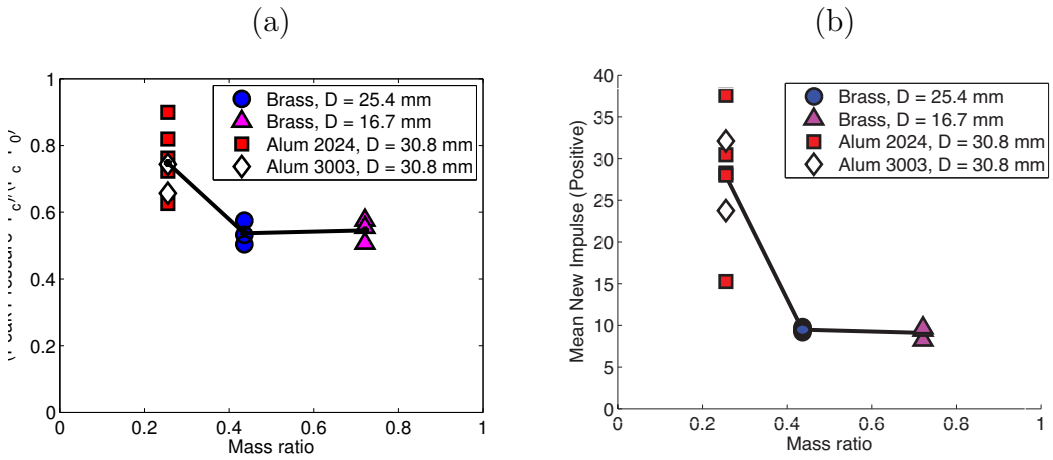

Figure 2.21: (a) The peak pressure for each mode 2 experimental run versus mass ratio, where the mass ratio is the mass of the structure over the mass of water that the structure displaces. (b) The pressure impulse for each mode 2 experimental run versus mass ratio. The pressure impulse was computed for the positive pressure peak for twice the time range of the first zero crossing to the peak pressure.

models, it was decided to also examine the variation of the pressure impulse, which is usually a more stable measurement, versus the mass ratio. The time range in the computation for the impulse was taken as twice the time from the upward zero crossing to the peak pressure, starting at the upward zero crossing. Fig. 2.21 (b) shows this pressure impulse versus the mass ratio for each mode 2 implosion. The pressure impulse for the two brass cylindrical models (B2D25 and B2D16) are nearly the same. However, the pressure impulse for the aluminum model implosions (models A2A2 and A2A3) were, on average, higher than those for the brass model implosions and had a much larger range. The cause of the large range of peak dimensionless pressure values and pressure impulses for the aluminum cylindrical models was not known. It should be noted that the ambient implosion pressure had a small range (from 26.4 to 28.7 bar or 5% of the average, 27.4 bar) while the dimensionless peak pressure had a relatively large range (from 0.63 to 0.90 or 20%

of the average).

2.4.2 Natural Implosions: Constant Available Energy

In this section, the results of implosion modes 2, 3, and 4 (B2D25, B3D25, and B4D25) for the Brass 260 cylindrical models with the same diameter and the same available energy are presented. One of the cylindrical model designs used in the previous section on mode 2 implosions is repeated here for comparison with the mode 3 (B3D25) and 4 (B4D25) implosions. Therefore, the plots will not be repeated in this section except when making a comparison. Fig. 2.22 and Fig. 2.23 show one representative run for a mode 3 and 4 implosion, respectively. As in the previous section, these figures show the eight meridian plane pressure sensors as well as still frames from the high-speed movie matched in time with three of the key features in the pressure record. The key features in the collapse for these higher mode-cylindrical models, as can be seen in the figures, are the same features discussed in the previous section for mode 2.

Fig. 2.24 shows one representative run for each of three cylindrical models (B2D25, B3D25 and B4D25). The collapse times and pressure amplitudes are clearly different for each geometry. For each run shown, there is a variation in the pressure records for each of the sensors. A similar analysis to that performed in the previous section is carried out here. Using polar coordinates, the azimuthal direction (pressure sensor positions) and the time (radial direction) are visualized. Refer to the previous section for the details on the construction of the plots. Fig. 2.25 (a) and (b) show one representative case in mode 3 and 4, representatively. Unfortunately,

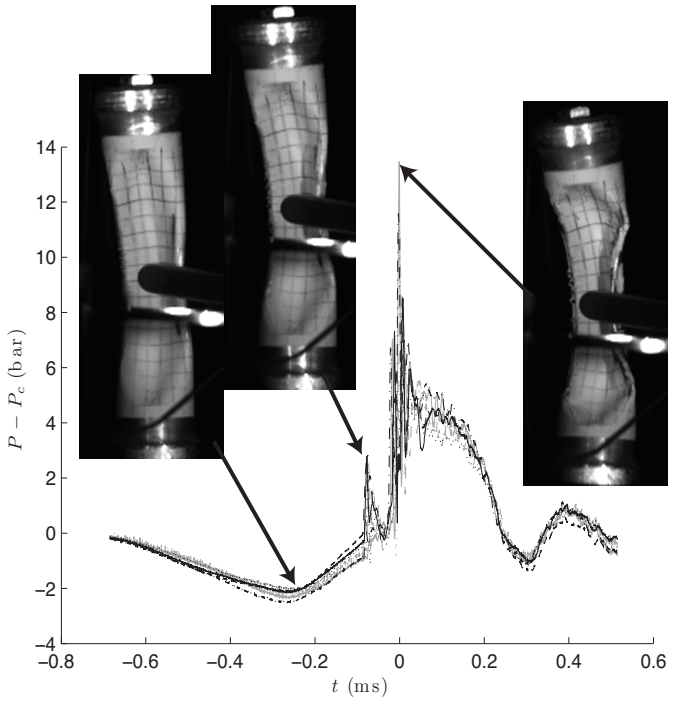

Figure 2.22: Each line represents one of the eight meridian pressure sensors for B3D25r1. Three still frames from the high-speed video are shown at the times corresponding to the minimum pressure peak, first small positive peak and the maximum positive peak. As the walls close in, there is a drop in pressure. The first small positive peak occurs when the walls first impact each other. The large positive pressure peak occurs when the collapse is complete. For a complete set of pressure records and still frames, see Appendix A.

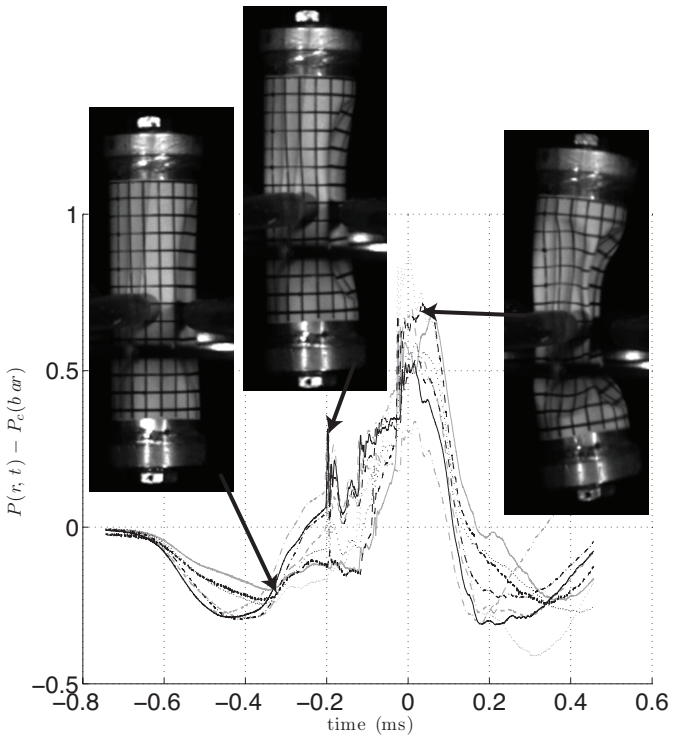

Figure 2.23: Each line represents one of the eight meridian pressure sensors for B4D25r1. Three still frames from the high-speed video are shown at the times corresponding to the minimum pressure peak, first small positive peak and the maximum positive peak.

due to the greater number of lobes in the cross sectional shape, the final deformed shape with respect to the azimuthal direction was not accurately measured.

When examining the final deformed cross-sectional shapes of the cylindrical models, it was found that the lobes were not azimuthally symmetric for modes 3 and 4. Some representative cylindrical models are shown in Fig. 2.26. Some of the final deformed cross sections for mode 3 had two lobes that appeared to be pinching, and some of the mode 4 cylindrical models appeared to have 3 lobes very close together. A couple mode 4 cylindrical models appeared to have 3 lobes, but one lobe was very thick and looked as it would develop into two lobes.

It was already shown in Fig. 2.20 that the mode 2 cylindrical shell pressure waves scale in time and pressure for different material and geometry. An average of the eight meridian plane sensors is taken as the one representative curve for each experimental run for the cylindrical models that have diameters of 25.4 mm. Fig. 2.27 shows the same time and pressure scaling as Fig. 2.20, where the time is scaled by $R_i\sqrt{\rho/(P_c - P_0)}$ and the pressure is scaled by $P_c - P_0$. The scaling of time looks appropriate but the pressure scaling yields peaks that are different in magnitude. Some of the speculated causes in the discrepancy in normalized pressure peak magnitude are different amounts of deformation per unit length of the model, of heat dissipated and of radiated energy as pressure waves. In this experiment, only the pressure waves are measured, so no concrete conclusion can be drawn about the deformation or the dissipated heat.

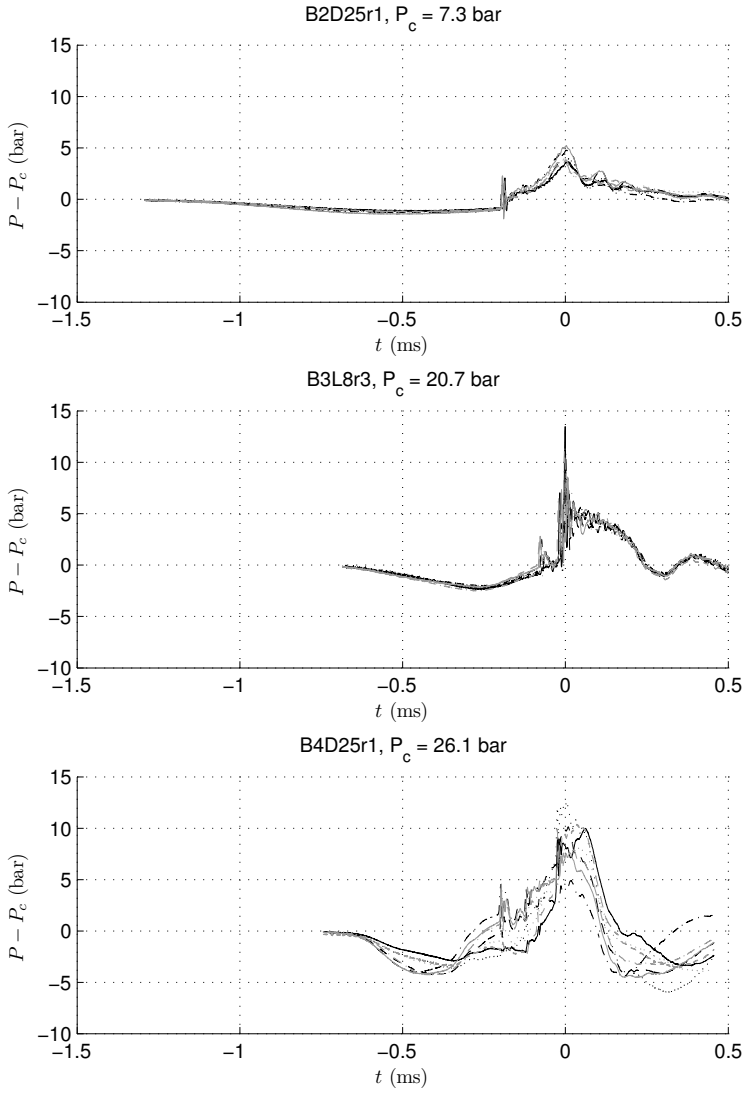

Figure 2.24: A comparison of one representative run for each geometry B2D25r1, B3L8r3, and B4D25r1. As expected, the collapse times and maximum peak pressures for each of these cylindrical models are different.

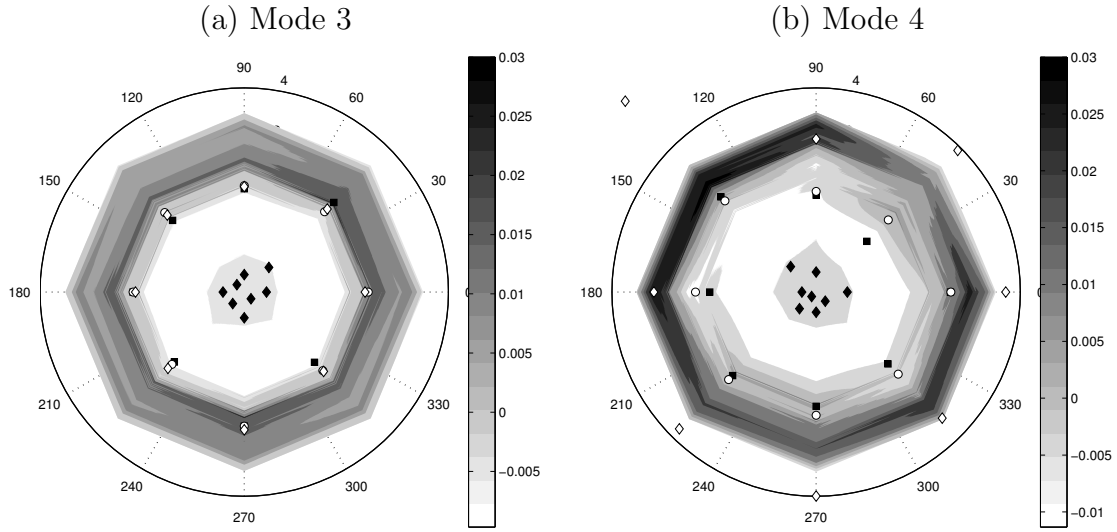

Figure 2.25: (a) One representative pressure contours for mode 3, B3D25r3. (b) One representative pressure contours for mode 4, B4D25r1.

2.4.3 Natural Implosions: Constant P, Constant V

The final discussion of results presents the cylindrical models that have the same available energy, the same collapse pressure, and the same volume of air. These brass 260 cylindrical models collapsed in implosion modes 2 and 4 (B2D16 and B4D25). Both models have been discussed in the previous two sections and are presented here for comparison. Fig. 2.28 shows one representative run for each of the two cylindrical models in this study. The collapse times and pressure amplitudes are observed to be different.

It was already shown in Fig. 2.20 that the mode 2 cylindrical shells of different material and geometry scale in time and pressure, and it has been shown in Fig. 2.27, that for constant available energy and constant diameter cylindrical models, the pressure waves do not scale for modes 2, 3, and 4. In this case, the available energy is constant by keeping the internal volume and the collapse pres-

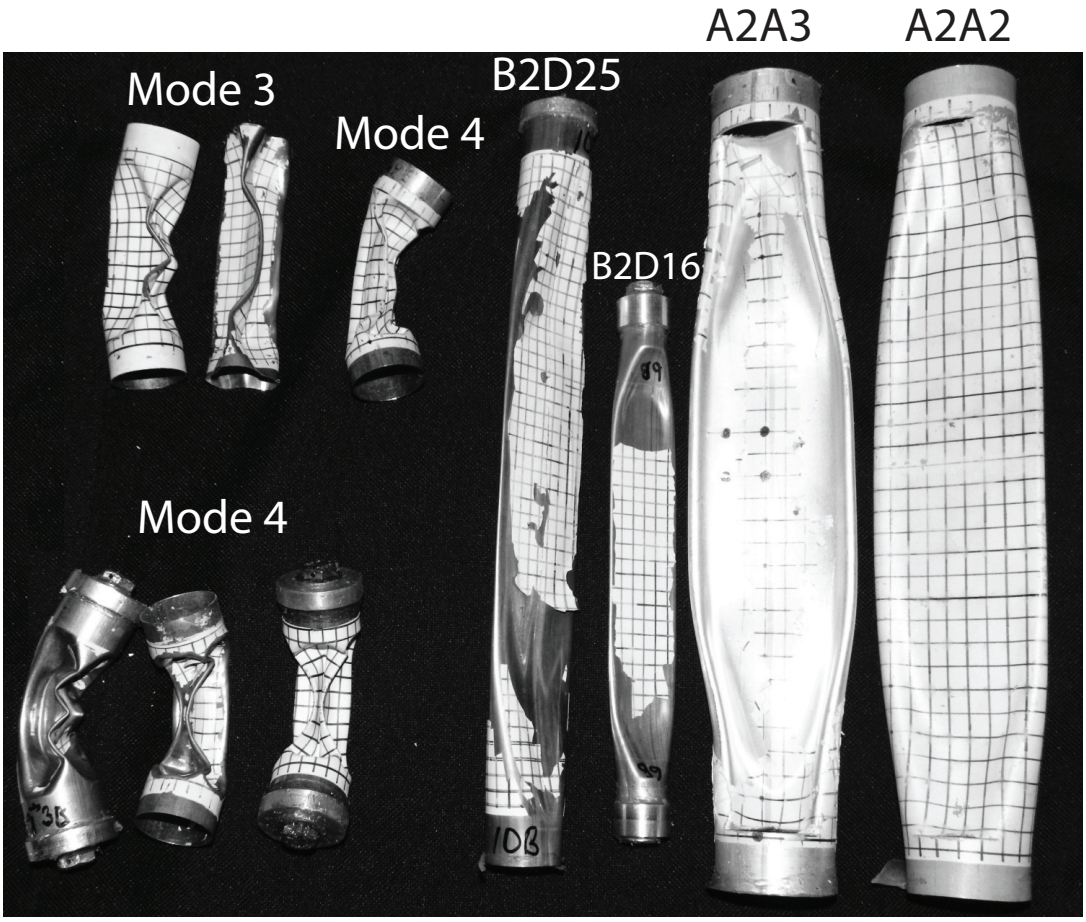

Figure 2.26: This photograph shows representative cylindrical models after they were imploded. For the mode 2 cases, only one representative model is shown since all repeated runs appear to be similar. For the higher modes, there are more repeated models shown because of the variation in the final deformed shape. It should be noted that the paint for these models came off the cylindrical models during the collapse event due to the high deformation.

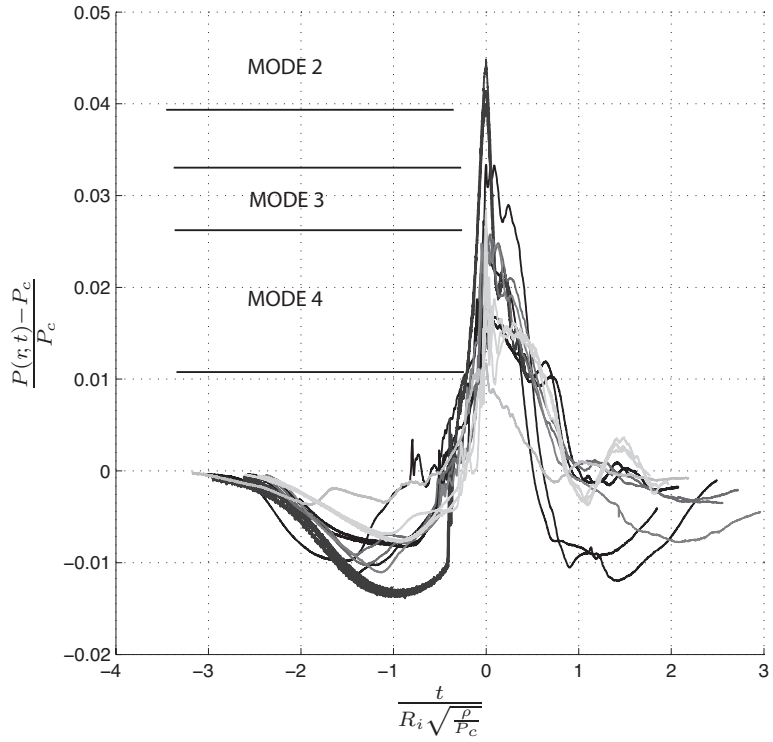

Figure 2.27: An average of the meridian plane pressure sensors for the cylindrical models with constant available energy collapsing in modes 2, 3, and 4 are scaled in the time axis by the characteristic bubble collapse time, $R_i\sqrt{\rho/(P_c - P_0)}$, and the pressure (vertical) axis by the relative pressure of the ambient collapse pressure and the initial gas pressure inside the structure, $P_c - P_0$. It is seen that the time scales match, but the pressure peaks do not. The highest pressure peak is for mode 2 and the lowest pressure peak is for mode 4.

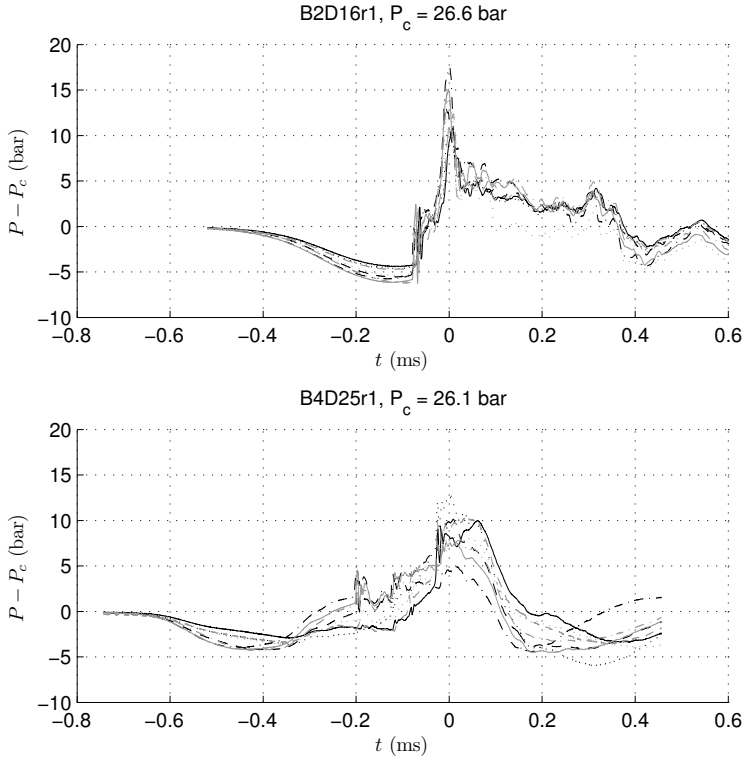

Figure 2.28: To compare constant available energy cylindrical models with nearly the same collapse pressure, pressure versus time curves for all eight meridian plane sensors are shown for two representative runs. The specific runs are B2D16r1 and B4D25r1.

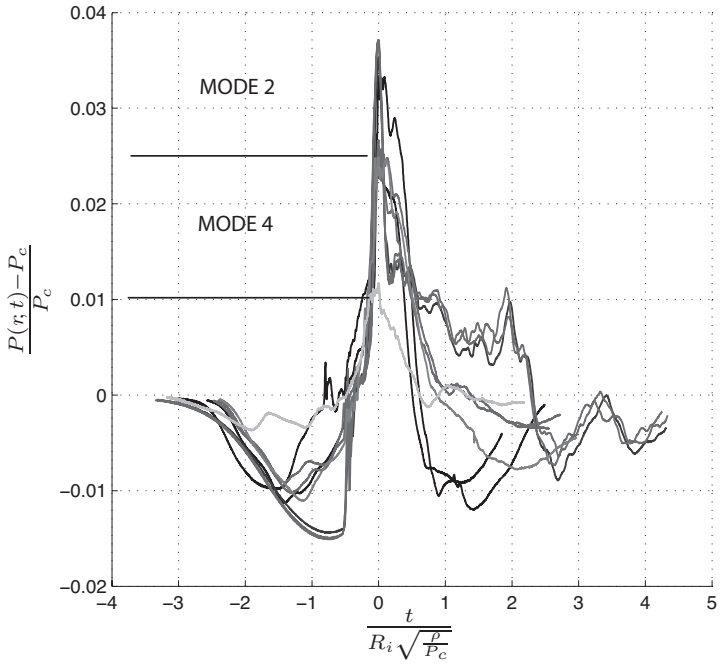

Figure 2.29: An average of the meridian plane pressure sensors for the cylindrical models collapsing in mode 2 and 4, with constant P_c and V, are scaled in the time axis by the characteristic bubble collapse time, $R_i\sqrt{\rho/(P_c - P_0)}$, and the pressure (vertical) axis by the relative pressure of the ambient collapse pressure and the initial gas pressure inside the structure, $P_c - P_0$.

sure nearly the same. An average of the eight meridian plane sensors is taken as the one representative curve for each experimental run for the cylindrical models in this comparison. Fig. 2.29 shows these curves with the maximum peaks lined up at time zero, where the time is scaled by $R_i\sqrt{\rho/(P_c - P_0)}$ and the pressure is scaled by $P_c - P_0$. The scaling of time looks appropriate but the pressure scaling yields peaks that are different in magnitude.

2.5 Conclusions and Future Work

An experimental study of the implosion of cylindrical shell structures in a high-pressure water environment was performed with the aim to determine the

effect of geometry and material on the resulting pressure waves. High-frequency underwater blast sensors were used to record dynamic pressure waves at the same non-dimensional distance from the meridian plane of the cylindrical models. The cylindrical models are made from brass 260 alloy and aluminum 2024 alloy and 3003 alloy. Cylinder length-to-diameter (L/D) ratios between 2.3 and 10 were examined, which resulted in implosion modes of 2, 3, and 4. The process of collapsing cylindrical shell structures was carefully documented in terms of high-frequency pressure waves, and the motion of the collapsing walls was correlated with the pressure waves.

The linear theory (from Sturm [56]) that predicts the elastic instability limit and the mode number at which a cylindrical model will implode was not accurate for the models in this experiment probably due to slight differences in the end conditions (which arise from the method of mounting the cylindrical models in the experimental facility and the design and installation of the model end caps). Therefore, it was necessary to empirically map out certain regions of the elastic instability curves, particularly in the region near the transition between modes 3 and 4. Using the experimental predictions, the models having the same available energy (P_cV) were chosen more accurately.

For the models that collapsed in mode 2, the azimuthal distribution of the pressure peak and pressure impulse did not correlate with the orientation of the final deformed collapse shape. When comparing the pressure waves and in particular the collapse times and peak pressure magnitudes varied significantly from one model design to another. However, when the average of the eight meridian plane pressure sensors was scaled in time with the characteristic gas bubble collapse time

$\left(R_i\sqrt{\rho/\left(P_c - P_0\right)}\right)$ and scaled in pressure by the relative pressure between the ambient collapse pressure and the initial gas pressure inside the structure $(P_c - P_0)$, the pressure waves are remarkably similar. The normalized collapse times are nearly identical and the pressure peaks are within the run-to-run variation of one of the models tested. These results may indicate that during collapse, the stiffness of the out-of-round metal structure is minimal compared to the hydrodynamic forces.

A similar investigation was performed for cylindrical models that were constructed from the same material (brass 260) and tube stock (the same diameter and wall thickness) but with model lengths chosen to collapse in modes 2, 3 and 4 with the same available energy (P_cV). In these experiments it was not possible to reliably measure the final orientation of the deformed collapsed model shape for modes 3 and 4. When comparing the pressure waves for these cylindrical models, the collapse times and pressure wave magnitudes were very different. The averages of the eight meridian plane pressure sensors for each run were scaled in time and pressure, using the same characteristic variables mentioned above. The time scaling appeared to be accurate, but scaled pressure magnitudes varied significantly from one model design to another. This result might be caused by the variation in energy required to deform the model and the percent volume change during collapse from one model to another, both of which would change the energy that went into the pressure waves.

The final comparison was performed for cylindrical models with constant available energy, but where the collapse pressures (P_c) and internal volumes (V) were

nearly constant. For these experiments, two different diameters of brass cylindrical models were used and these models collapsed in mode 2 and 4 shapes. Scaling of the pressure waves in time and pressure as discussed in the previous paragraph yielded similar results. The mode 4 cylindrical models yielded a lower pressure amplitude when scaled and underwent more deformation per unit length than the mode 2 cylindrical models. Even though the available energy was the same for the two cylindrical models, different amounts of energy were radiated away as pressure waves.

From the scaling of the pressure waves for the three experimental studies, it was found that the time scaling was appropriate for all runs. This means that the collapse time of the air inside the structure is independent of the structure once it undergoes large deformations and becomes weak. On the other hand, the pressure scaling was appropriate for the mode 2 implosions only. The amount of deformation per unit length is the same for all mode 2 implosions. Therefore, the same percentage of energy is expected to be used to deform the structure, leaving the same amount of energy to be radiated away as both heat and pressure waves. The mode 2 experimental results show that the same amount of scaled energy is radiated away from the structure as pressure waves. In the constant available energy experiments, different mode numbers are observed for different geometries of cylindrical models. For different mode numbers, the deformation per unit length is different. Since the mode 2 cylindrical models have the least amount of deformation per unit length, then it is expected that less energy is required for deformation and more energy is available to be radiated away as pressure waves. The scaling for the pressure is typ-

ical for collapsing bubbles and therefore, does not inherently consider the structure deformation. A more extensive study on mode 3 and 4 implosions with different materials and geometry may answer this question.

Chapter 3
The Explosion-Induced Implosion of Cylindrical Shell Structures in High-Pressure Water

3.1 Abstract

An experimental study of the explosion-induced implosions of cylindrical shell structures in a high-pressure water environment was performed. The shell structures were filled with air at atmospheric pressure and placed in a large water-filled pressure vessel. The vessel was then pressurized to various pressure levels $P_\infty = \alpha P_c$, where P_c is the natural implosion pressure of the model and α is a factor that ranges from 0.8 to 0.9. An explosive was set off at various standoff distances, d_0, from the model center line, where d_0 varies from $1.4R$ to $10R$, and R is the predicted maximum radius of the explosion bubble. High-speed photography (27,000 fps) was used to observe the explosion and resulting shell structure implosion. High-frequency underwater blast sensors recorded dynamic pressure waves at several positions. The cylindrical models were made from aluminum (diameter $D = 39.1$ mm, wall thickness $w = 0.89$ mm, length $L = 240$ mm) and brass ($D = 16.7$ mm, $w = 0.36$ mm, $L = 152$ mm) tubes. The pressure records were interpreted in light of the high-speed movies. It was found that the implosion can be induced by one of two mechanisms: the shockwave generated by the explosion or the hydrodynamic pressure field of the explosion bubble during its collapse and re-expansion. Whether an implosion is caused by the shockwave or the explosion bubble's hydrodynamics pressure field depends on the maximum bubble diameter and the stand-off distance.

3.2 Introduction

3.2.1 Underwater Explosions

Robert H. Cole's [17] book published in 1948, which is still relevant today, gives a detailed description of underwater explosions. An explosion is a chemical reaction in an inherently unstable material that occurs extremely fast and produces a large amount of heat. An explosion is triggered by introducing a sufficient amount of energy to this explosive material. The chemical reaction is initiated in a small area, which then triggers the chemical reaction to the rest of the explosive material [17].

When an explosion takes place in water, the water is considered compressible. The sudden increase in pressure caused by the explosion generates a shockwave, or a steep-fronted compression wave. This shockwave radiates outward relieving the high pressure of the explosive reaction at speeds that could be of the order of several times the (linear) acoustic wave speed in water (1482 m/s). As the wave front moves outward, the magnitude of the pressure drops rapidly to acoustic values. The speed of propagation of the wavefront also decreases with the distance traveled eventually approaching the speed of sound in water[17].

When the shockwave encounters a boundary or obstacle, it reflects back. On rigid boundaries, the interaction between the reflected and incoming wave is constructive (due to the rigid nature of the boundary); therefore the pressure amplitude is doubled close to the wall. Reflected waves from a free surface interact destructively with the incoming wave, due to the constant pressure condition at the free

surface [17].

Immediately following the detonation of an explosion, a bubble of explosive byproduct gases is generated. The first stage of the gas bubble is an expansion in which the pressure inside decreases rapidly. Due to the effect of inertia, the bubble over-expands and at its maximum size, its internal pressure is less than the local ambient pressure. The bubble then begins to collapse due to the imbalance of pressure on the two sides of the fluid-gas interface. Upon reaching the minimum volume, the pressure in the bubble is much higher than ambient and it expands again. A number of these oscillations persist until all energy is lost to radiation, chemical or physical changes in the gaseous products, actual loss of gaseous products in the form of small bubbles, or turbulence (which can be caused by viscous drag of the bubble moving upward due to buoyant forces). With each bubble collapse, a positive pressure pulse is emitted, and with each cycle, the bubble maximum radius and frequency of oscillation decrease [17, 1].

The Principle of Similarity for blast waves is widely used when presenting results from explosion experiments. The Hopkinson-Cranz scaling law is an extension of the Principle of Similarity, where the ambient conditions are assumed to be invariant. These scaling law is often called the "cube-root" law. The customary scaled distance is

$$Z = R/W^{\frac{1}{3}}, \tag{3.1}$$

the customary scaled time is

$$T = t/W^{\frac{1}{3}}, \tag{3.2}$$

and the customary scaled impulse is

$$\zeta = I/W^{\frac{1}{3}}, \tag{3.3}$$

where Z, T, and ζ are constants, R is the characteristic length, t is the characteristic time, I is the characteristic impulse, and W is the mass of the explosive [3]. Using this scaling relation, the size of the bubble created by an explosion can be calculated.

In order to scale the bubble size based on changes in ambient pressure (while keeping the explosive mass constant), the Rayleigh-Plesset equation can be used. The Rayleigh-Plesset equation is the potential flow (incompressible and irrotational) solution to the problem of an oscillating (collapse and re-expansion) gas bubble in water. It is a solution to Laplace's equation,

$$\bigtriangledown^2\phi = 0, \tag{3.4}$$

where $\mathbf{u} = \bigtriangledown\phi$ (i.e., the velocity, u, is the gradient of the velocity potential, ϕ). The kinematic boundary condition is that the particles at the air-water interface remain on the interface or

$$\frac{d\mathbf{x_p}}{dt} = \bigtriangledown\phi\left(\mathbf{x_p}, t\right), \tag{3.5}$$

where $\mathbf{x_p}$ is the position vector of a particle, $\mathbf{p}$, that is on the interface. The dynamic boundary condition is that the pressure across the interface is continuous and using Bernoulli's equation this can be expressed as

$$\frac{D\phi}{Dt} = \frac{1}{2}\ \left|\bigtriangledown\phi\right|^2 + \frac{P_\infty - P_b}{\rho}, \tag{3.6}$$

where P_∞ is the pressure far away from the bubble, ρ is the density of the fluid

(water) and P_b is the pressure inside the bubble, given by the polytropic law

$$P_b = P_0 + P_{g_0} \left(\frac{V_0}{V} \right)^{\gamma}, \tag{3.7}$$

where P_0 is the vapor pressure, V_0 is the initial bubble volume, V is the instantaneous bubble volume and γ is the isotropic constant ($\gamma = 1.3$). Assuming that the initial bubble radius is the radius of the detonator, R_0, and that the initial velocity of the bubble at $t = 0$ is $\dot{R}_0 = 0$, the Rayleigh-Plesset equation can be used to find a relationship between the parameters describing the initial state of the bubble and the maximum bubble radius:

$$\frac{P_{g_0}}{(P_\infty - P_0)} = (1 - \gamma) \left[\left(\frac{R_{max}}{R_0} \right)^3 - 1 \right] \left[\left(\frac{R_{max}}{R_0} \right)^{3-3\gamma} - 1 \right]^{-1}. \tag{3.8}$$

Using Eq. 3.1, the maximum bubble radius can be scaled based on different sizes of explosives. Using Eq. 3.8, the effect of the ambient pressure on the maximum bubble radius can be estimated.

Keller and Kolodner [35] modified the above theory to account for the compressibility of the water. Their modified theory predicted damped bubble oscillations of diminishing period, and their predictions agreed with experimental data.

3.2.2 Explosions and Gas Bubbles in Proximity to Rigid Structures

The detonation of an underwater explosive can cause serious damage to nearby structures. Since the 1950s, the dynamic response of submerged structures loaded by underwater explosions have been a topic of interest. An underwater explosion can cause damage by two mechanisms; the shockwave and the oscillations of a gas bubble formed by the explosive byproducts.

Huang and Wang [34] simulated three-dimensional, transient, spherical acoustic waves interacting with a cylindrical elastic shell structure. They found that the pressures at the fluid-shell interface could be negative indicating the possibility of cavitation.

Geers and Felippa [31] used Doubly Asymptotic Approximations (DAAs), which are differential equations for the boundary element analysis of the interaction of a structure surrounded by an infinite fluid, to explore the interaction of shell structures with a surrounding liquid. They found that the second-order form of the DAA accurately predicted the free-vibration modes of a submerged spherical shell.

Kwon and Fox [37] compared numerical simulations to experimental results of the nonlinear dynamic response of a cylinder subjected to a far-field underwater explosion. They found through experimental strain measurements that the cylinder rotated as a result of the explosion either due to an asymmetric flow field or due to improper rigging. In the numerical simulations, they discovered three modes of dynamic motion exhibited by the explosion-loaded cylinder: the accordion mode, breathing mode, and whipping mode.

Brett et al. [6] conducted small-scale experiments of the deformation of submerged cylinders subjected to a nearby explosion. They measured the pressure pulses in the liquid and the accelerations of the structure walls, and quantified the deformation of the cylinder. It is important to note that the cylinder was sufficiently strong that the deformation did not include implosion of the cylinder. From the pressure records in the experiments, Brett et al. argue that cavitation occurred near the wall of the structure during the explosion event. In the pressure record,

there is first very large-amplitude peak with a short time duration, the shockwave. Immediately following the shockwave is a shorter peak, which is the reflection of the shockwave off the structure. Following that is a slight dip in pressure below the ambient pressure, which led Brett et al. to hypothesize that there were cavitation bubbles in the water surrounding the structure. These cavitation bubbles then collapse, causing another high pressure peak. If the structure is not damaged due to the shockwave, the resulting gas bubble oscillations can cause damage to the structure. The pressure pulses that result from the bubble oscillations have a smaller amplitude but a longer time duration than the shockwave, therefore, these pressure pulses can have an impulse comparable to the shockwave. Another mechanism for damage due to the oscillating gas bubble is related to its asymmetric collapse and the formation of a re-entrant jet under some conditions. In this mechanism, the structure causes an obstruction of the water flow and produces a re-entrant water jet to form on the side of the bubble farthest from the structure. This jet pierces the opposite side of the bubble during the implosion and causes very high pressures on the structure [6].

Sato et al. [50] studied the behavior of a gas bubble near a rigid boundary in an oscillatory pressure field using numerical simulations. The study assumed an inviscid, incompressible, irrotational liquid surrounding a gas bubble that follows a polytropic gas law. The bubble migration (toward or away from the rigid wall) was found to be strongly dependent on the frequency of the oscillating pressure field. In this oscillatory pressure field, they also found that a liquid micro jet is formed during both the collapse process and the rebound process. Additionally, they found

that the period and amplitude of the bubble oscillations were dependent on the distance of the bubble from the rigid wall and to the time-dependent pressure field within the liquid.

Zhang et al. [66] simulated the collapse of an initially spherical cavity (the internal pressure of the bubble was held constant) near a rigid wall and followed the formation of the reentrant liquid jet. Their numerical method was based on conventional and hyper-singular boundary integral equations, which allowed for the continuous simulation of the bubble motion including the impact and penetration of the re-entrant jet. Their investigations showed that the bubble surface is transformed into a ring bubble (toroidal shape) that is smoothly attached to a vortex sheet during the impact of the re-entrant jet. This penetration interface becomes surrounded by a high-pressure region. Theoretical analysis and the numerical simulations proved that the impact of the jet on the bubble surface caused a loss in kinetic energy in the flow field. The authors believed this lost kinetic energy would be radiated away as pressure waves in a compressible liquid. In addition, they found that the flow field was highly sensitive to the initial distance from the bubble center to the wall. It is important note that in these calculations, the volume of the bubble monotonically decreased to zero as the collapse occurred since, as mentioned above, the pressure in the bubble was held constant.

Zhang and Duncan [67] expanded the previous work to model the internal gas pressure, which is dependent on the instantaneous bubble volume. Qualitatively, the results were found to be similar in that a re-entrant jet was formed during the final stages of the collapse creating the toroidal shaped ring bubble and that a shear

layer developed along the interface of the impact. However in this later work, it was found that the bubble reaches a minimum volume (and a re-entrant jet begins to form) and the high internal gas pressures cause a rebound in the bubble. During this rebound, Zhang and Duncan found that the pressure on the wall reached a maximum value (in the previous work, this maximum pressure value on the wall could not be computed).

Popinet and Zaleski [46] studied the effect of viscosity on the jet formation of collapsing bubbles near solid boundaries. In comparisons with experiments, they found that the damping of radial oscillations of the gas bubble cannot be attributed to viscous dissipation alone. They speculated that both acoustic and thermal dissipation need to be considered in order to accurately capture the dynamics of the oscillating bubble. In their parametric study of the effect of viscosity, they found that the jet impact velocity decreases as the viscosity increases. There is a critical Reynolds number below which the jet impact will not occur. This critical Reynolds number was found to be dependent on the initial bubble radius and the relative distance between the bubble and the wall.

Wang and Khoo [60] used an indirect boundary element method to model three-dimensional explosion bubbles. The simulations examined a single explosion bubble, two symmetric explosion bubbles close to one another (both away from and near a free surface), an explosion bubble near a rigid sphere (near a free surface), and an explosion bubble near a wall to determine the effect of nearby objects on the shape of the bubble as it collapsed. For the simulation of the explosion bubble near a rigid wall, Wang and Khoo [60] compared their results to experimental data. During

the expansion of the bubble in both the simulation and experiment, the bubble flattened along the side boundary closest to the wall. As the bubble collapsed, it lost its vertical symmetry due to gravity effects. A re-entrant jet was formed on the opposite edge of the bubble from the wall, and the jet moved toward the wall in the simulation. Unfortunately, due to optical limitations, the jet was not seen in the experimental data [60].

3.2.3 Present Work

Numerous studies have been conducted on underwater explosions, underwater explosion bubbles, and explosions near rigid structures. However, little research has been conducted on the combination of underwater explosion loading on cylindrical shell structures that become unstable and implode. The object of the present experiment is to combine the work presented above with the experiments conducted in Chapter 2 to understand the failure of a cylindrical shell structure due to a nearby explosion. There are two mechanisms that are predicted to cause the failure of the cylindrical shell structure, the explosion shockwave and the oscillating gas bubble. High-speed movies combined with pressure records will give insight into the collapse process of a cylindrical shell structure subjected to a nearby explosion.

3.3 Experimental Details

For this experiment, models that were studied in the natural implosion phase of the experiment are used. In each experiment, the ambient pressure in the water tank is raised to some fraction of the elastic instability limit of the model, then a

small (29 to 203 mg) explosive charge is detonated at varying stand-off distances from the model.

3.3.1 Explosives: Reynolds Detonators

Reynolds detonators are Exploding Bridgewire (EBW) detonators and are manufactured by hand by Reynolds Industries Systems, Incorporated (RISI). The detonators consist of two layers of explosive materials. The explosive materials contained in the detonator cap are Pentaerythritol tetranitrate (PETN, $C_5H_8O_{12}N_4$) (initiating explosive) and Cyclotrimethylenetrinitramine (RDX, $C_3H_6N_6O_6$) (output explosive). PETN is sensitive to shock and friction while RDX is more stable.

For the experiments in this dissertation, both RP-87 and RP-80 EBW detonators were used. The RP-87 contains 26 mg of PETN and 43 mg of RDX with a stainless steel cap outside the brass sleeve. The RP-87 was used in the first set of experiments at low ambient pressures. The RP-80 contains 80 mg of PETN and 123 mg of RDX with an aluminum cap outside the brass sleeve. Two gold bridgewires are embedded in the PETN parallel to one another. The other ends of the bridgewires are connected to lead wires which are in turn connected to a firing module.

To ignite the explosive, the lead wires are connected to an FS-17 firing module, also manufactured by RISI. The FS-17 sends a high voltage (3000 V) across the bridgewire. The high voltage causes the bridgewires to evaporate in the detonator cap, creating a shockwave that initiates the detonation of the PETN and then the RDX.

3.3.2 High-Frequency Pressure Measurements

The ambient water pressure in the tank was obtained from measurements of the pressure of the nitrogen gas using a slow-response pressure transducer (Honeywell, Model TJE, Range 0 to 1,000 psig, resolution 1 psi), discussed in Sec. 2.3.3.

The dynamic pressure waves in the water were measured with up to 9 underwater blast sensors that use a Tourmaline crystal sensor (PCB Piezoelectronics, Inc. models #138A02 and 138A01). These are the same pressure sensors discussed in Sec. 2.3.3. These pressure sensors are arranged into three different configurations.

Fig. 3.1 shows the positions of the pressure sensors in the configuration used in the first experiment. The cylindrical model was placed at the center of the experimental facility. Eight pressure sensors were mounted to the ring described in Sec. 2.3.3. The axis of the ring was aligned with the vertical axis of the the tank, and the ring was displaced down by 22.86 cm with respect to the center of the tank. Two pressure sensors, A and B, were placed at a distance for 25.4 cm from the center of the cylindrical shell structure. Pressure sensor A was placed on the same side of the cylinder as the Reynolds detonator, and pressure sensor B was on the opposite side. Pressure sensors C and D were placed at a distance for 55.88 cm from the center of the cylindrical shell structure; Pressure sensor C was on the same side of the cylindrical model as the Reynolds detonator, and pressure sensor D was on the opposite side. Finally, one pressure sensor (not shown in Fig. 3.1) was placed directly below the center of the cylindrical model at a distance of 50.8 cm.

In the second configuration, shown in Fig. 3.2 (a), only six pressure sensors

were used. This configuration was used for the second set of experiments that were conducted on brass cylindrical shell structures. Two pressure sensors were placed near the tank walls, and the remaining four were placed at a radial distance of 30.5 cm from the detonator. As seen in Fig. 3.2 (a), one pressure sensor was placed such that the cylindrical model was in between the pressure sensor and the detonator. The reason for this placement was so the structure would block the shockwave pressure from the pressure sensor in the hopes that the implosion pressure signal from the structure could be seen in the pressure sensor.

The third configuration, shown in Figs. 3.2 (b), (c), and (d), was used for the final set of experiments which was conducted on aluminum cylindrical shell structures. In this configuration, nine pressure sensors were used. Like in the first configuration, two pressure sensors were placed near the wall. Three pressure sensors (E, F and G) were placed at a radial distance of 30.5 cm from the detonator, with one sensor (E) behind the cylindrical shell structure, as shown in Fig. 3.2 (b). Three pressure sensors (A, B, and D) were placed at a radial position of 5.08 cm from the detonation, shown in Fig. 3.2 (c), which in these experiments is the stand-off distance from the detonator to the cylindrical shell structure. Therefore, three pressure sensors can record the shockwave pressure at the same radial location as the cylindrical model. Three pressure sensors (A, B, and C), shown in Fig. 3.2 (c), with two also located at 5.08 cm from the detonator, are placed 2.86 cm from the center axis of the cylindrical shell structure. Again, the reason for the placement of sensors C and E behind the structure was so the structure would block the shockwave pressure from the pressure sensor. The close proximity to the structure would also

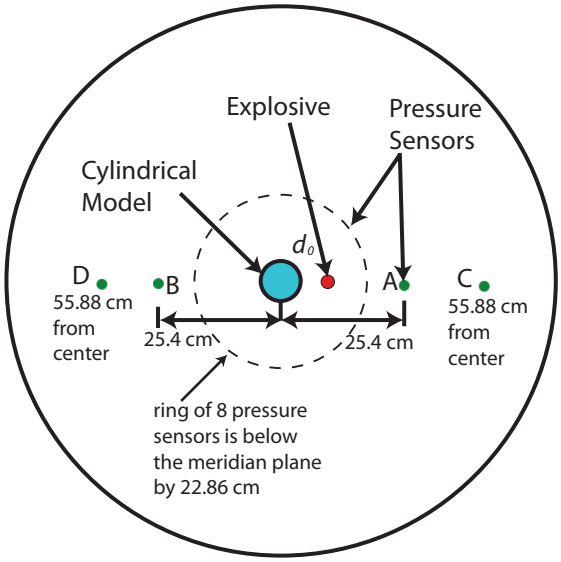

Figure 3.1: Pressure sensor positions for the preliminary experiment (First Configuration). The cylindrical model was placed in the center of the experimental facility, and the RP-87 detonator was placed in the meridian plane at a distance of 2.54 cm from the edge of the cylindrical model.

help to discern the implosion signal within the explosion event assuming that the structure collapses before the shockwave reflects back from the tank walls.

3.3.3 High-Speed Photography

The motion and deformation of the model during an explosion-induced implosion is recorded with high-speed digital photography, using a Phantom V12.1 camera (Vision Research, Inc.) with an 1280-by-800-pixel sensor and a maximum sampling rate of 6242 frames per second (fps) at full resolution. The camera was set to record 27,000 fps at an image size of 512 by 512 pixels. A timing system triggers the A/D system, camera, and detonation simultaneously, so that the pressure signals over the 37-μs period that each image is captured can be examined.

The camera is positioned to view the implosion through one of the glass win-

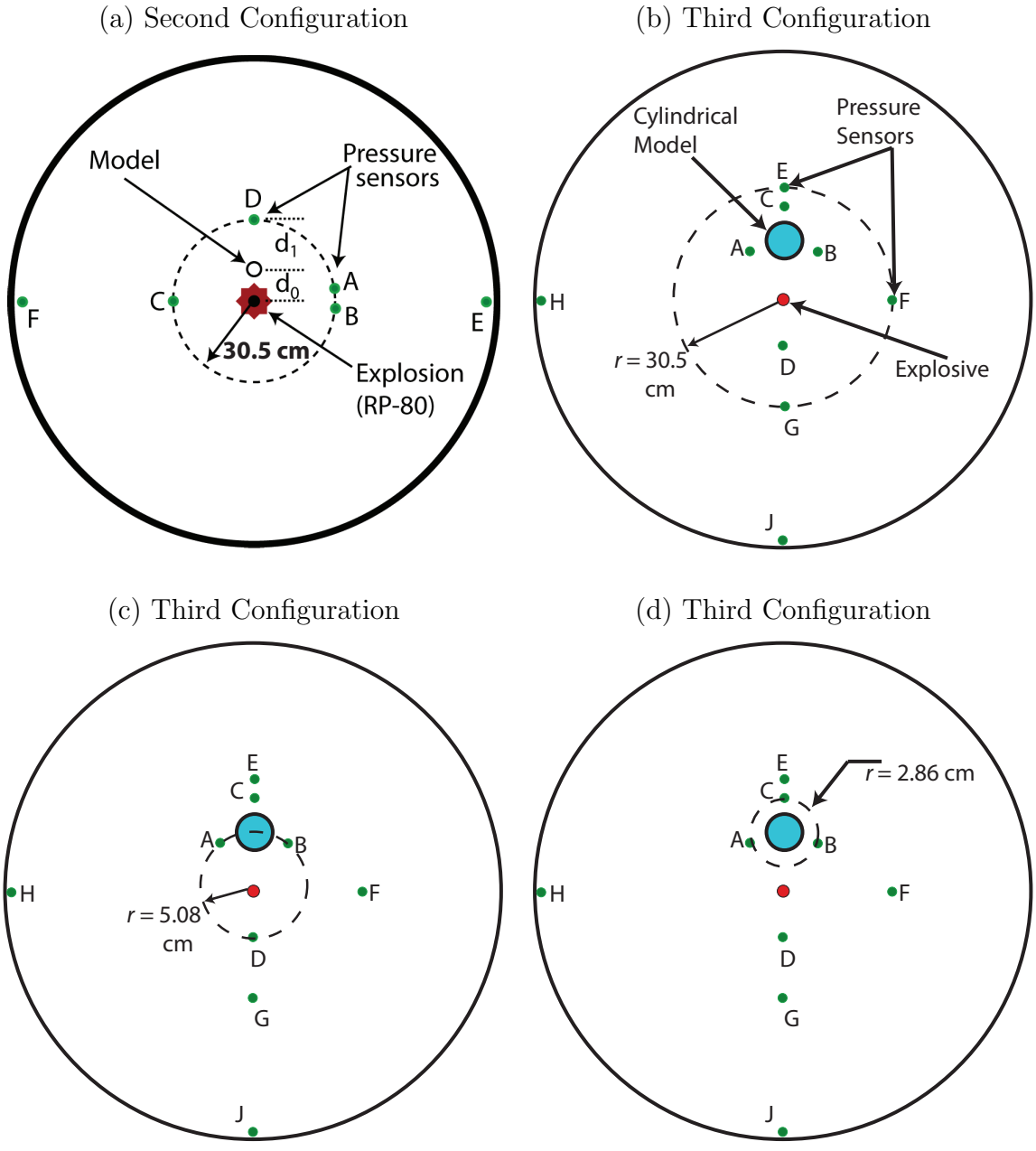

Figure 3.2: Second and third pressure sensor configurations for the explosion experiments.

dows in the mid-plane of the tank and the two adjacent windows are used to project light from two 650-W flood lamps onto the model (shown in Fig. 2.3 (b)). From the movies of the implosions, both qualitative information and quantitative measurements can be extracted. The qualitative information includes the orientation of the collapsed model with respect to the tank and explosive, the state of the model at any time, and via the relative timing of the explosion and implosion, whether the implosion is triggered by hydrodynamics of the collapsing bubble or the shockwave of the detonation. Quantitative measurements include the implosion time of the model, the maximum radius of the explosion bubble, and the oscillation period of both the model and the explosion bubble.

3.3.4 Test Procedures

To perform an experiment, the EBW detonator is placed in the center of the experimental facility, and the model and pressure sensors are placed in their desired positions. The front manhole and drain were closed, and the tank was filled with water through the 50.8-mm-diameter ball valve in the piping tree at the top of the tank until ≈5.7 L of air remained. The water ball valve was closed, and the tank was slowly pressurized with nitrogen gas through a solenoid valve in the piping tree. The ambient pressure was set to a predetermined value, $P_{amb} = \alpha P_c$, where α is a factor ranging from 0.8 to 0.9. The A-to-D pressure sensor system, camera, and explosive detonation were then triggered simultaneously with the zero referenced to the trigger initiation. Due to electrical delay, the detonation occurred 2-ns after the

trigger, and 1.5 s of data was recorded. Once the explosive detonated, the nitrogen inlet valve was closed and a separate valve opened to depressurize the tank. After each experiment, the water inlet valve was opened and the tank was drained through the valve at the bottom.

3.3.5 Plan of Experiments

Table 3.1 shows a summary of the explosion-induced implosion experiments that were conducted. The columns in the table show the run designation, the stand-off distance between the explosion and cylindrical model, whether the model collapsed or not, and whether a high-speed movie was taken. The run designation starts with either a "B" for models constructed from brass tubes or an "A" for models constructed from aluminum tubes. This followed by an "E" for explosion-induced implosions, the standoff distance (a number in centimeters) and the run number. Three experimental studies were conducted. In the first, the cylindrical model collapsed due to impact from the re-entrant bubble jet formed by the explosive-byproduct-gas bubble as seen in a high-speed movie. In the second set of experiments, the standoff distance between the explosive and cylindrical models was varied over a range of distances such that the gas bubble would not impact the structure. In these second experiments, no high-speed movies were taken and the maximum value of d_0 for the model to collapse was found. In the final set of experiments, the collapse of two models constructed with different materials and geometries was investigated under similar loading conditions.

Run	Material	Diam D (mm)	Standoff Distance d_0 (cm)	Ambient Pressure P_{amb}	Implosion?	High-Speed Movie?
BE25r01	Brass	25.4	2.54	$0.81P_c$	yes	yes
BE05r01	Brass	16.7	5.08	$0.9P_c$	yes	yes
BE05r02	Brass	16.7	5.08	$0.9P_c$	yes	no
BE10r01	Brass	16.7	10.16	$0.9P_c$	yes	no
BE12r01	Brass	16.7	12.7	$0.9P_c$	yes	no
BE15r01	Brass	16.7	15.24	$0.9P_c$	yes	no
BE17r01	Brass	16.7	17.78	$0.9P_c$	yes	no
BE17r02	Brass	16.7	17.78	$0.9P_c$	no	no
BE22r01	Brass	16.7	22.86	$0.9P_c$	yes	no
BE27r01	Brass	16.7	27.94	$0.9P_c$	yes	no
BE30r01	Brass	16.7	30.48	$0.9P_c$	yes	no
BE30r02	Brass	16.7	30.48	$0.9P_c$	no	no
BE33r01	Brass	16.7	33.02	$0.9P_c$	no	no
BE60r01	Brass	16.7	60.96	$0.9P_c$	no	no
AE05r01	Al 6061	3.81	5.08	$0.89P_c$	yes	yes
AE05r02	Al 6061	3.81	5.08	$0.89P_c$	yes	yes
AE05r03	Al 6061	3.81	5.08	$0.89P_c$	yes	yes
BE05r01	Brass	16.7	5.08	$0.9P_c$	yes	yes

Table 3.1: A summary of the explosion-induced implosion experiments. The names given have a "B" for brass or an "A" for aluminum. The next letter is either an "E" for explosion-induced or "N" for natural implosion. The next two numbers describe the stand-off distance, d_0, then there is an "r" representing the run number for the given conditions. These names will be used in plot legends and plot titles to give a quick reference to the cylindrical models in this table.

3.4 Results and Discussion

As described above, three sets of experiments were performed, which are summarized in Table 3.1. As was noted in the previous chapter, due to the destructive nature of these experiments, a new model must be used for each experimental run, therefore, run-to-run variations in the results are to be expected.

3.4.1 Explosion-Induced Implosions: Re-entrant Jet

As previously mentioned, one experiment (designated BE25r01) involving a cylindrical model having a diameter of 25.1 mm (the model design was designated B2D25 in the natural implosion experiments, $P_c = 7.3$ bar) was conducted. The ambient pressure in the experimental facility was set to $P_{amb} = 5.9$ bar, or 81% of its natural collapse pressure (P_c). Using this ambient pressure, the Hopkinson-Cranz scaling law (Eq. 3.1), and the Rayleigh-Plesset equation (Eq. 3.8), the maximum explosion bubble radius for the Reynolds detonator, RP-87, was calculated to be 3.92 cm.

The stand-off distance between the explosive and the wall of the cylinder was 2.54 cm. It was found however, that the bubble of explosive gases was more elongated in the vertical direction, therefore, the bubble did not make contact with the cylindrical model during its first expansion. A high-speed movie was taken at a rate of 27,000 frames per second. A set of images taken from the high-speed movies is shown in Fig. 3.3. Fig. 3.3 (a) shows the initial set up of the cylindrical model and detonator. It is important to note the orientation of the Reynold's Detonator provides an orientation for the nearly axisymmetric, but non-spherical explosion bubble. In this case, the axis of the cylindrical detonator is pointing down about about 15 degrees toward the axis of the model. Fig. 3.3 (b) shows the detonation of the RP-87. Fig. 3.3 (c) shows the explosive gas bubble at its first maximum bubble radius. The bubble is hard to see, as it appears to look like a cloud. Fig. 3.3 (d) shows the bubble at its first minimum bubble radius. In Fig. 3.3 (e), the oscillating

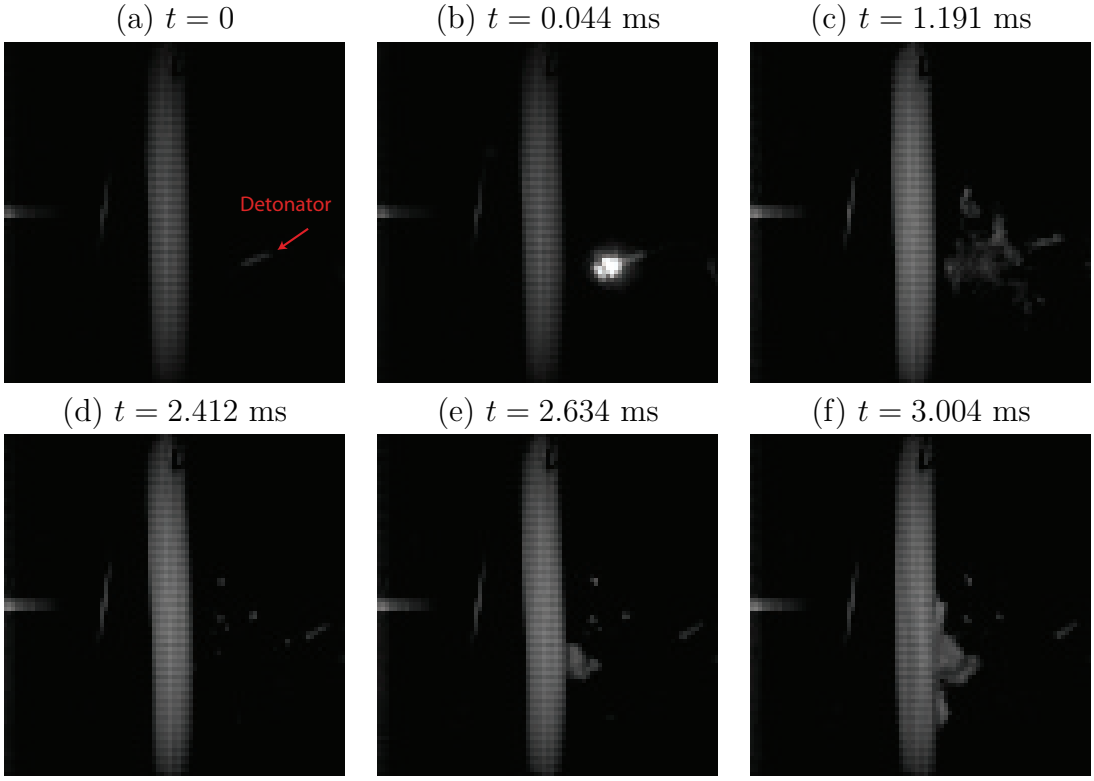

Figure 3.3: A sequence of images from the high-speed movie of the preliminary experiment of a brass cylindrical shell model implosion triggered by a Reynolds detonator, RP-87, at a 25.4 mm stand-off distance (d_0). The high-speed movie was taken at a rate of 27,000 frames per second. (a) the start of the experiment, (b) detonation of the RP-87, (c) oscillating gas bubble at its first maximum bubble radius, (d) oscillating gas bubble at its first minimum bubble radius, (e) re-expansion and new position of oscillating gas bubble, and (f) cylinder begins to collapses.

bubble re-expanding and its center shifting closer to the cylindrical shell structure. In Fig. 3.3 (f), the cylinder collapses due to the reentrant jet of the gas bubble during its second expansion.

From the pressure records obtained, the high-pressure wave from the explosion reached the pressure sensors on the ring (the closest pressure sensors to the explosive) at time, $t = 0.3$ ms, as measured relative to the time of detonation. Comparing this time with the sequence of images from the high-speed movies in Fig. 3.3 (f), it can be seen that the collapse of the cylindrical model occurs about 3 ms after the

detonation, which is more than 10 times later than the moment when the high-pressure wave reached the cylindrical model.

Fig. 3.4 (a) shows that the pressure records for the ring of pressure sensors have nearly identical peak pressure values, arrival time and time duration of the peak. This is expected since these pressure sensors are the same distance from the explosion event (see Fig. 3.1 for pressure sensor positions). Fig. 3.4 (b) shows records from the other pressure sensors, which are located at varying distances away from the explosion. As expected, the closest pressure sensor, A, shows the high-pressure wave arriving the earliest. The pressure peak magnitudes decrease with distance away from the explosion. The arrival time of the high-pressure wave to the pressure sensor is earlier for pressure sensors closer to the explosive.

3.4.2 Explosion-Induced Implosions: Stand-off Distance

The cylindrical model with the smallest diameter (designated B2D16 in the natural implosion experiments), which has the shortest collapse time in these experiments, was chosen for the rest of the experiments with the brass models since the collapse time with respect to the reflection time was small. However, as discussed before, this smaller cylindrical model requires a higher ambient pressure for its natural implosion. The available glass windows installed in the experimental facility were not designed to withstand the total pressure due to the combination of the required ambient pressure and the explosion overpressure, all the window ports in the experimental facility were covered with stainless steel plates.

(a) 8 Pressure Sensors in a Ring 22.86 cm below the meridian plane

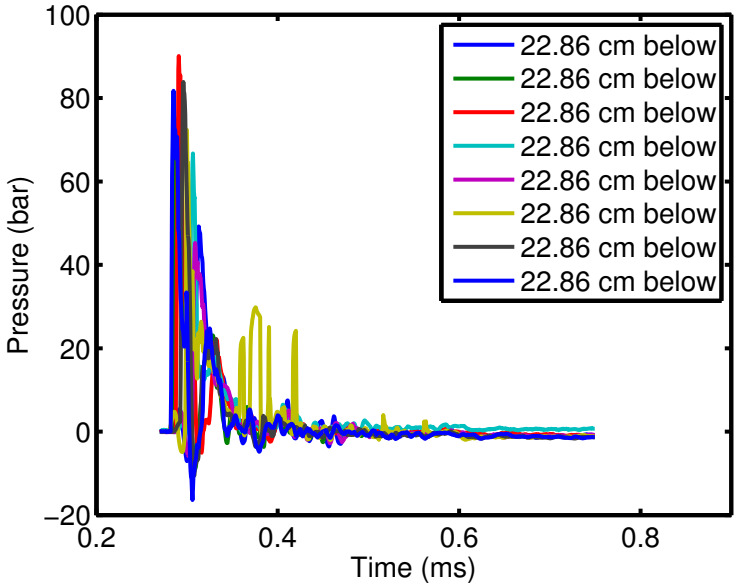

(b) Pressure Sensors on the Meridian Plane

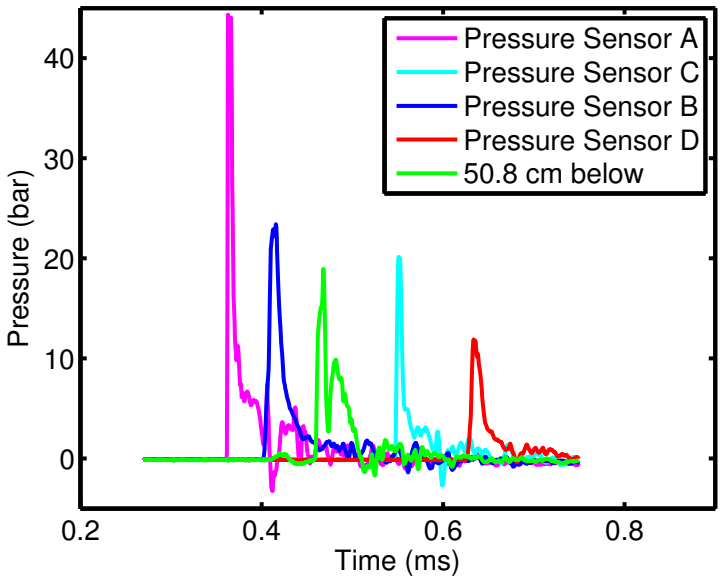

Figure 3.4: Pressure versus time record for the 13 pressure sensors used in the preliminary experiment, model BE25r01. (a) The eight pressure sensors mounted on a ring and placed 22.86 cm below the meridian plane of the tank (at the same distance from the explosion). (b) Pressure Sensors A-D are in the meridian plane. Pressure Sensor A and C are on the side of the cylindrical model where the explosive is located, see Fig. 3.1, and Pressure Sensor B and D are on the opposite side if the cylindrical model. The final pressure sensor is directly below the cylindrical model at a distance of 50.8 cm.

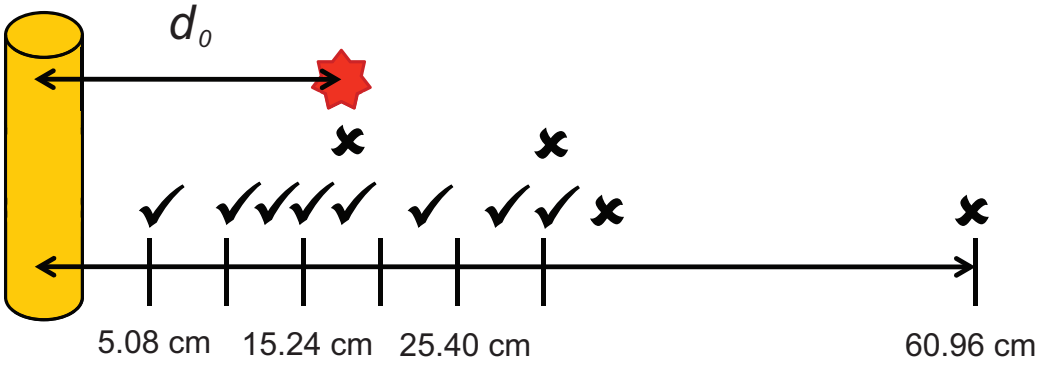

Figure 3.5: This schematic summarizes the stand-off distances for the set of experiments with the 16.7-mm diameter brass models with the detonator (RP-80) placed in the center of the experimental facility and the stand-off distance between the detonator and the cylindrical shell structure varied between 5.08 cm and 60.96 cm. The ambient pressure in the experimental facility was held constant at $P_{amb} = 24.1$ bar. The "x"-marks indicate that the model did not implode and the check-marks indicate the model did implode. As can be seen, a wide range of stand-off distances greater than the predicted maximum radius for the explosion bubble were used.

In the set of experiments with the brass cylindrical models of diameter 16.7 mm, the detonator (RP-80) was placed in the center of the experimental facility and the stand-off distance between the detonator and the cylindrical shell structure was varied between 5.08 cm and 60.96 cm. The ambient pressure in the experimental facility was held constant at $P_{amb} = 24.1$ bar. For this ambient pressure and detonator, the explosive bubble maximum radius ($R_{bub} = 3.56$ cm) was predicted using Eqs. 3.1 and 3.8. Therefore, it was expected that the bubble should not impact the structure on the first bubble expansion. A summary of these experiments is shown in Table 3.1 and visualized in Fig. 3.5. It is noted that for two stand-off distances, $d_0 = 17.78$ cm and $d_0 = 30.48$ cm, two repeated experimental runs were carried out. For both of these standoff distances, the structure collapsed in one of the runs and not in the other. Because there was no high-speed video, it was unknown what

caused the discrepancy in these results.

The pressure sensor positions for this set of experiments are shown in Fig 3.2 (a). Fig. 3.6 (a) to (d) shows the pressure versus time recorded by pressure sensors A, B, C, and D, respectively, for all 11 experimental runs. As seen in each set of pressure records, there is a slight spread in the arrival time (a range of 0.02 ms). Given the speed of sound waves in water (1,480 m/s) this arrival time corresponds to a range of distances of 29 mm and it is believed that the this is caused by small variations in the relative position of the sensors and explosions from run to run. In addition, the arrival time for the shockwaves seen by pressure sensors A, B, and C is nearly the same. This is to be expected since the pressure sensors are nearly at the same distance from the explosion. The magnitude of the pressure peaks are not the same in a given run when comparing the three pressure sensors. Consistently, pressure sensor C has a much higher peak pressure. It is noted that unlike the preliminary experiments, the Reynolds detonator for these experiments was pointed vertically up in all runs, so the lead wires formed a vertical line moving downward away from the detonator cap. It is thought that the high pressure in sensor C might be caused by repeatable non-uniformity in the pressure wave resulting from the blasting cap design.

Fig. 3.7 shows the pressure records for all the sensors from each experimental. The data from each run are displaced vertically by a small amount on the same plot to illustrate the repeatability from run to run. These pressure records, which only show early times in the event, cannot be used to predict whether or not the structure collapsed. At later times, the shockwave reflection does not allow discernment of

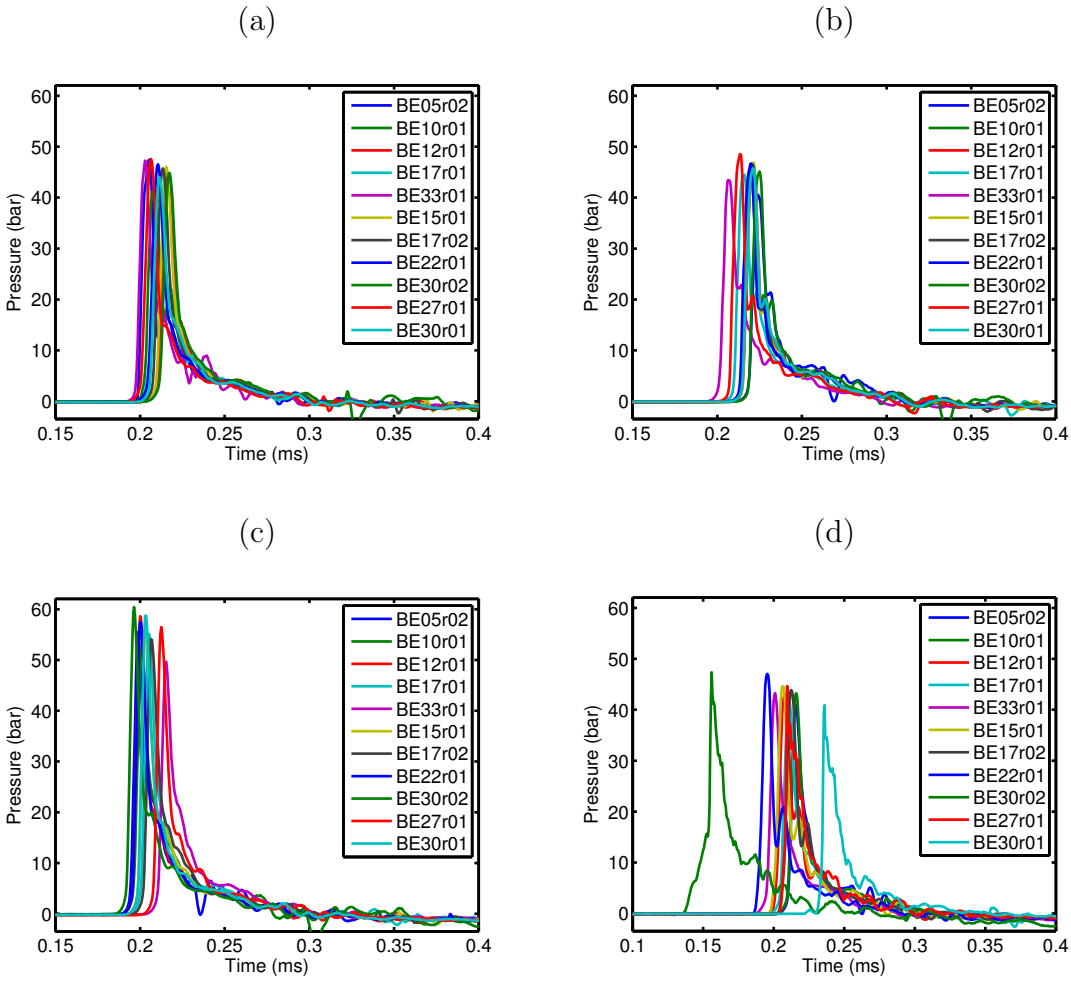

Figure 3.6: Pressure records for the four pressure sensor locations for the set of brass model experiments with the detonator (RP-80) placed in the center of the experimental facility and the stand-off distance varied between 5.08 cm and 60.96 cm. (a) Pressure sensor A, (b) Pressure sensor B, (c) Pressure sensor C, and (d) Pressure sensor D located 30.5 cm from the explosion.

the pressure signal from the implosion of the cylindrical model.

Once these experiments were completed, a new set of windows for the experimental facility was designed out of 7.62-cm-thick optically clear acrylic. Because the acrylic windows were thicker than the glass windows, a new window mounting system was designed and constructed. Once these new windows were installed, one additional run with a 16.7-mm brass tube model was conducted. Because this experiment was performed last, the third configuration for the pressure sensors was used, see Fig. 3.2 (a), (b), (c) and (d). Fig. 3.8 shows a sequence of images from the high-speed movie, taken at 27,000 frames per second. These images show the cylindrical model and detonator at the start of the experiment, the detonation of the RP-80, the bubble at the first maximum bubble radius, the bubble during the first minimum bubble radius, re-expansion of the bubble, and the end of the cylindrical structure collapse.

Fig. 3.9 shows the pressure records for BE05r02. The first pressure peaks in Fig. 3.9 (a) for sensors have a maximum value that is cut-off due to the limited range of the sensor used and the small distance between the sensors and the explosive. In Fig. 3.9 (b), the pressure record for sensor C is shown. The peak pressure is diminished because the cylindrical shell structure is between the explosive and the sensor and so the structure shields the sensor from the full shockwave. The second peaks in these records corresponds to the reflection of the high-pressure wave from the rigid tank walls. Fig. 3.9 (c) shows the pressure records obtained at pressure sensor locations E, F, and G (as seen in Fig. 3.2 (b)). The arrival of the high-pressure wave occurs at nearly the same time for each sensor as they are nominally

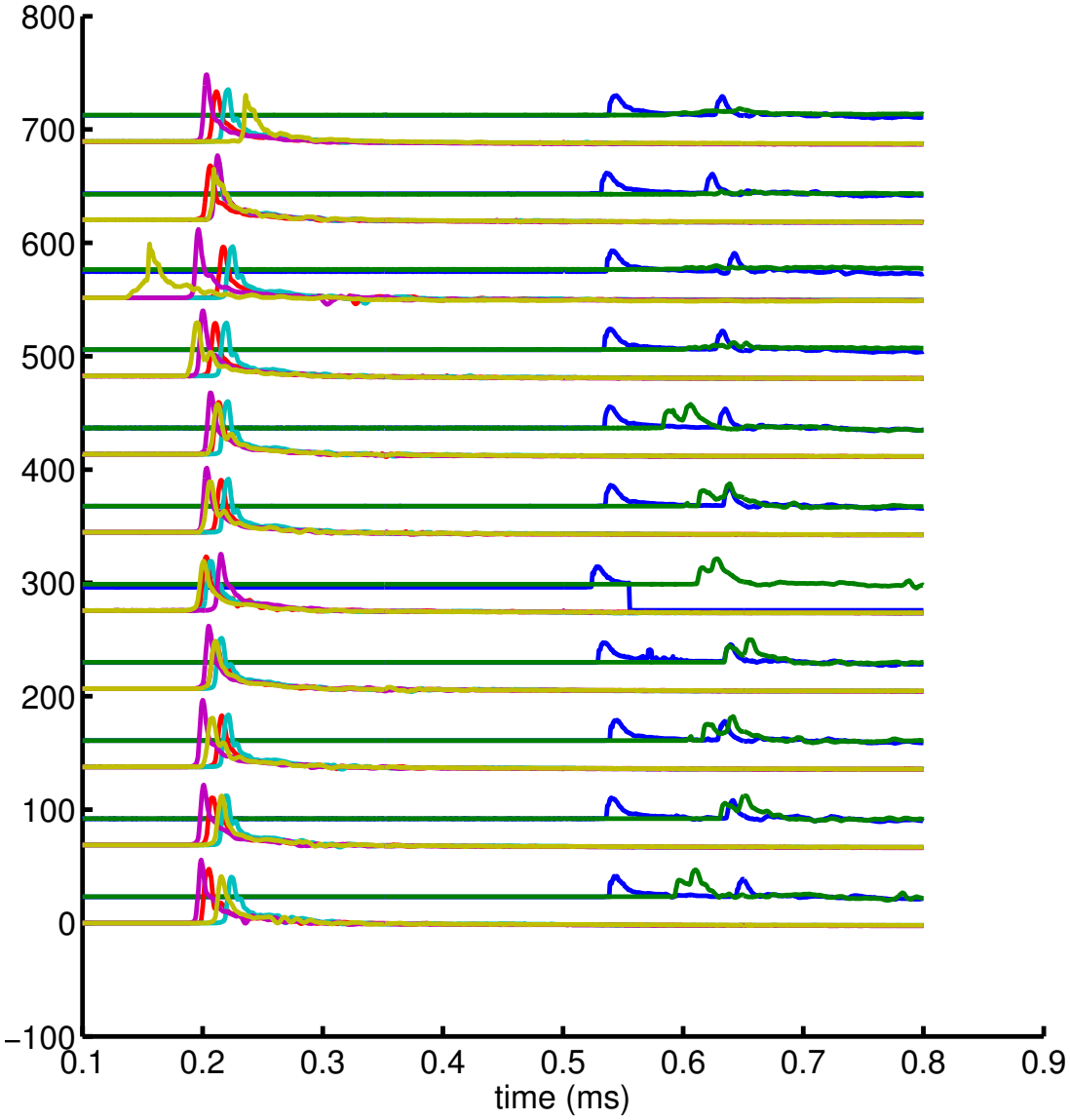

Figure 3.7: The pressure records for all the sensors from each experimental run. The records from each run are displaced vertically by a small amount to illustrate the repeatability from run-to-run. There is no visible difference between models that did or did not collapse.

(a) $t = -0.048$ (b) $t = 0$ ms (c) $t = 0.764$ ms

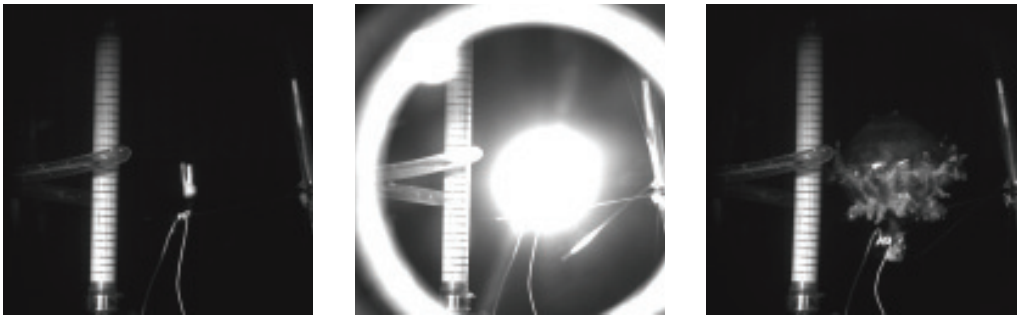

(d) $t = 1.337$ ms (e) $t = 1.624$ ms (f) $t = 2.006$ ms

Figure 3.8: A sequence of images from the high-speed movie of BE05r02. The high-speed movie was taken at a rate of 27,000 frames per second. (a) The start of the experiment, (b) detonation of the RP-80 , (c) the bubble reaches its maximum radius at 0.764 ms. (d) The bubble reaches its first minimum radius, (e) re-expansion of the gas bubble, and (f) the end of the cylinder collapse.

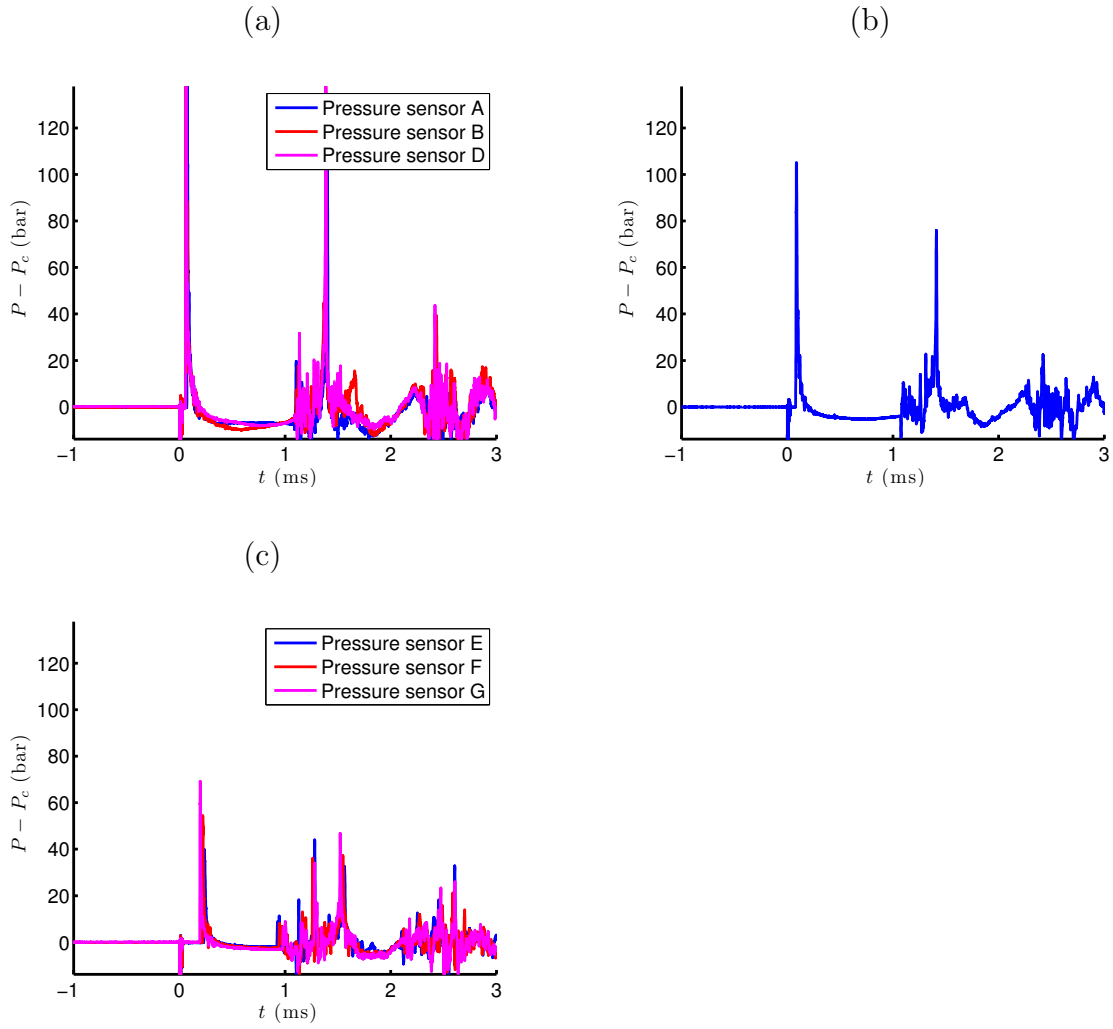

Figure 3.9: Pressure records for BE05r02. (a) Pressure sensors A, B, and D at 5.08 cm from explosion (b) Pressure sensor C, 2.86 cm from the cylindrical shell structure and located on the opposite side of the model from the explosion. (c) Pressure sensors E, F and G at 30.5 cm from the explosion.

the same distance away from the explosion event.

3.4.3 Explosion-Induced Implosions: Aluminum Cylindrical Models

In this set of experiments, the detonator (RP-80) was placed in the center of the experimental facility, and the stand-off distance between the detonator and the cylindrical shell structure was kept constant at $d_0 = 5.08$ cm. A summary of these experiments is shown in Table 3.1. In the first three aluminum models listed in Table 3.1, implosions were induced using a nearby explosion. These experiments are compared to the explosion-induced implosion of the brass cylindrical model in the last section (designated BE05r01). In all cases, high-speed movies of the implosion events were taken.

Fig. 3.10 (a), (b) and (c) show the pressure records for the three pressure sensors (A, B, and C) located closest to the cylindrical model for each explosive run with the explosion-induced implosions (see Fig. 3.2 for pressure sensor locations). The first pressure peaks (those from the shock wave from the explosion) have a maximum value that is cut-off due to the limited range of the sensor used. The second peaks in these records is the reflection of the shockwave from the rigid tank walls. In Fig. 3.10 (c), the first peak pressure is diminished because the cylindrical shell structure shields the sensor from the full shockwave. Fig. 3.10 (e) and (f) show the pressure records for the three pressure sensors (E, and F) located at a radial distance of 30.5 cm from the detonator for each of the three repeated runs. The arrival of the shockwave occurs at the same time for each sensor as they are the

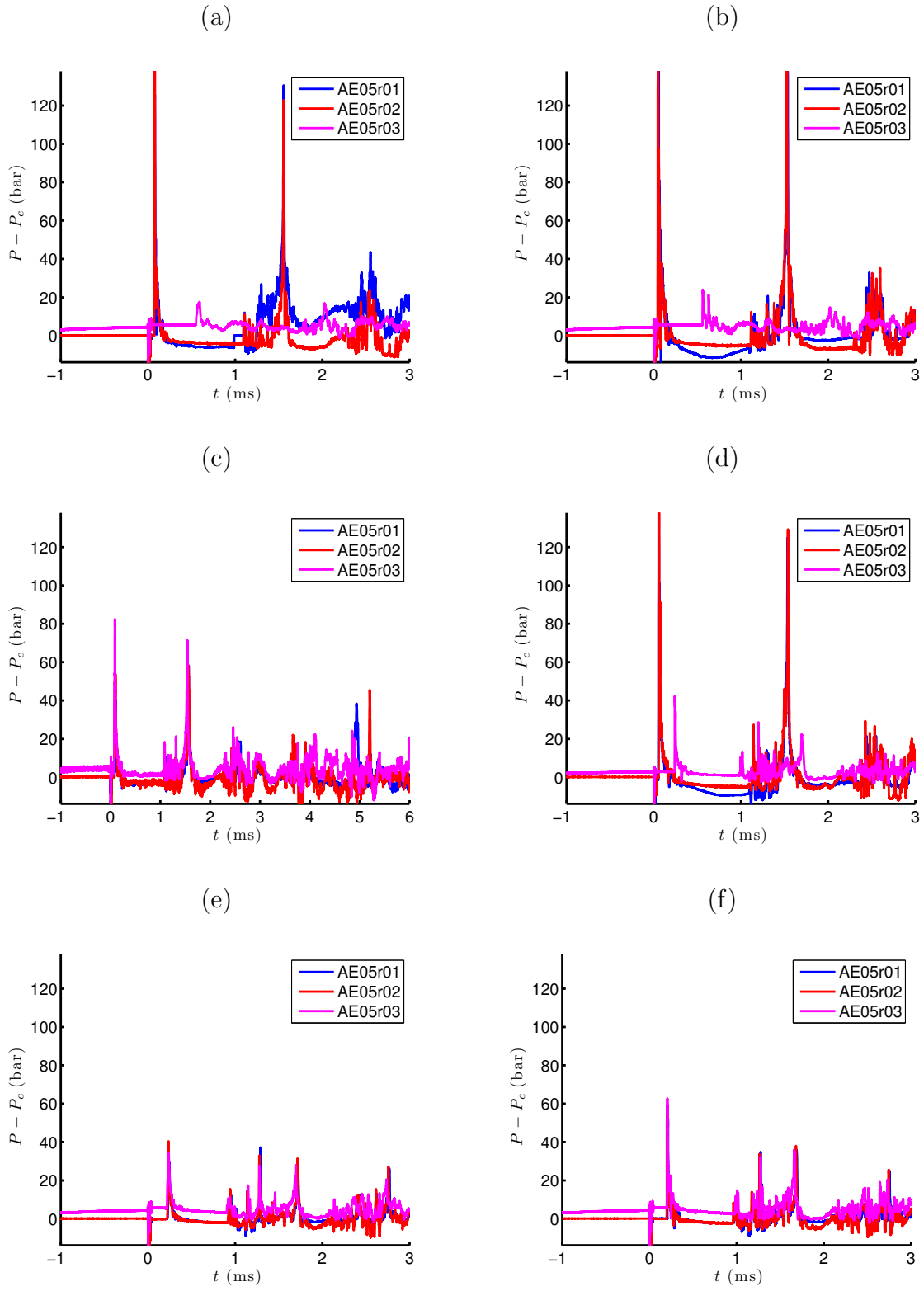

Figure 3.10: Pressure records for the pressure sensor positions (A to F) shown in Fig. 3.2 (b) for AE05r01, AE05r02 and AE05r03.

same distance away from the explosion event. The peak values for pressure sensors F, the pressure peaks are between 60 and 70 bar. The first peak value for pressure sensor E was about 40 bar. This lower pressure magnitude was due to the structure shielding the sensor from the explosion.

Figs. 3.11, 3.12, and 3.13 show a sequence of images from the high-speed movie of AE05r01, AE05r02, and AE05r03, respectively. The images show the characteristic events in the experiments: the start of the experiment, the instant when the detonation occurs, the instant when the explosion gas bubble reaches maximum size, the instant when the explosion gas bubble reaches minimum size, the second re-expansion of the gas bubble, and the end of the implosion of the cylindrical model. Comparing run-to-run, it is observed that the characteristic events occur at almost the same time, ranging from 0 to 0.096 ms apart. The time at which the cylinder collapses more variation from run-to-run than the other mentioned events. Furthermore, it is noted that the oscillating gas bubble does not make contact with the cylindrical model.

3.4.4 Explosion-Induced Implosions: Investigation of Failure Mechanisms

As discussed in the previous sections, the cylindrical models collapsed much later than the detonation of the explosive. In the first experiment, it was found that the cylindrical model collapsed due to the re-entrant jet of the explosive gas bubble. In the second experiment, the process of the collapse was recorded in one

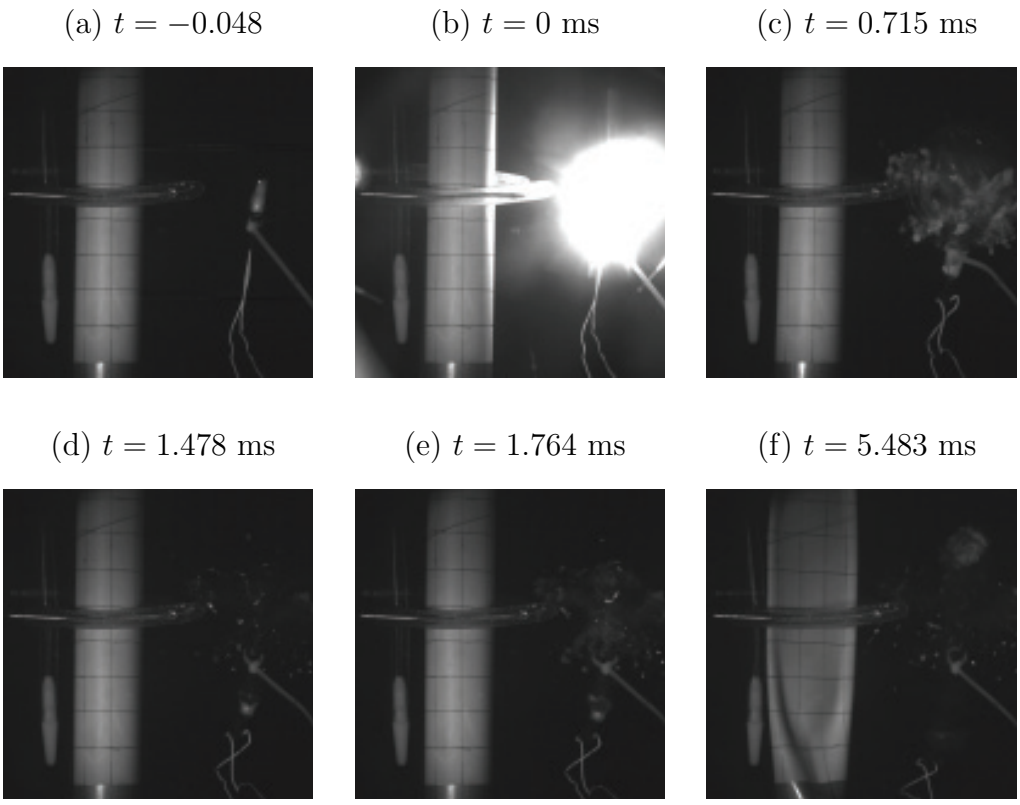

Figure 3.11: A sequence of images from the high-speed movie of AE05r01 (a) Start of the experiment. (b) Detonation of the RP-80. (c) First maximum bubble radius of the oscillating explosive gas bubble. (d) First minimum bubble radius of the oscillating explosive gas bubble. (e) The oscillating bubble is re-expanding. (f) Cylindrical shell structure collapses.

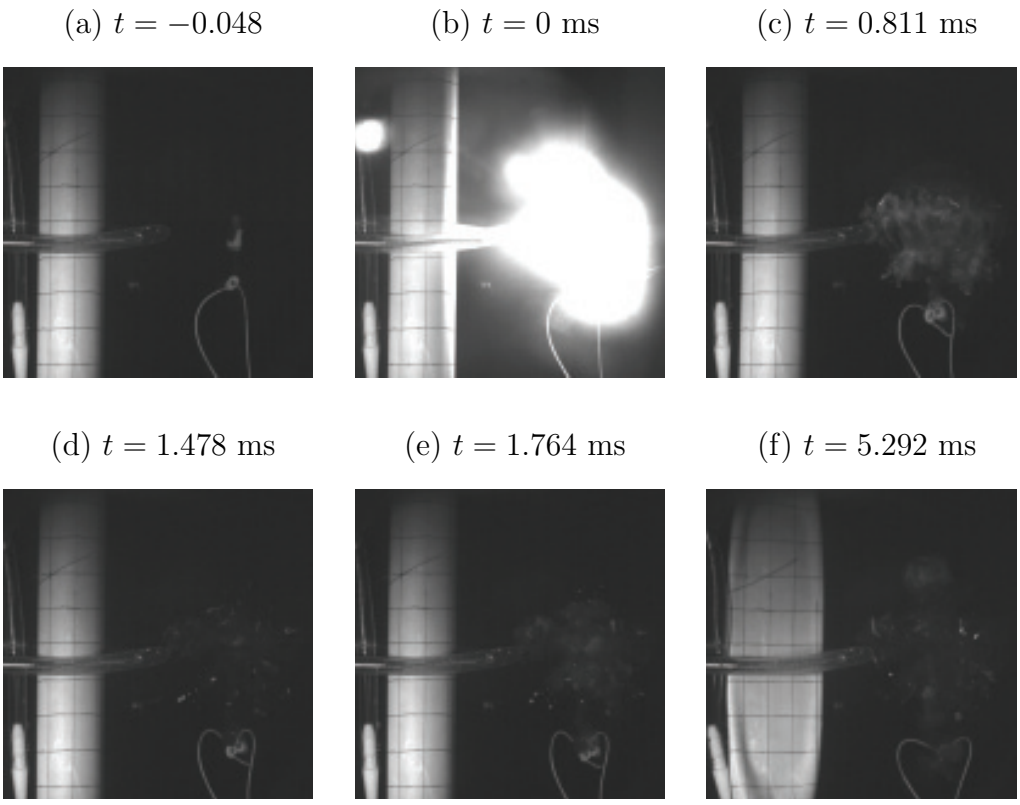

Figure 3.12: A sequence of images from the high-speed movie of AE05r02 (a) Start of the experiment. (b) Detonation of the RP-80. (c) First maximum bubble radius of the oscillating explosive gas bubble. (d) First minimum bubble radius of the oscillating explosive gas bubble. (e) The oscillating bubble is re-expanding. (f) Cylindrical shell structure collapses.

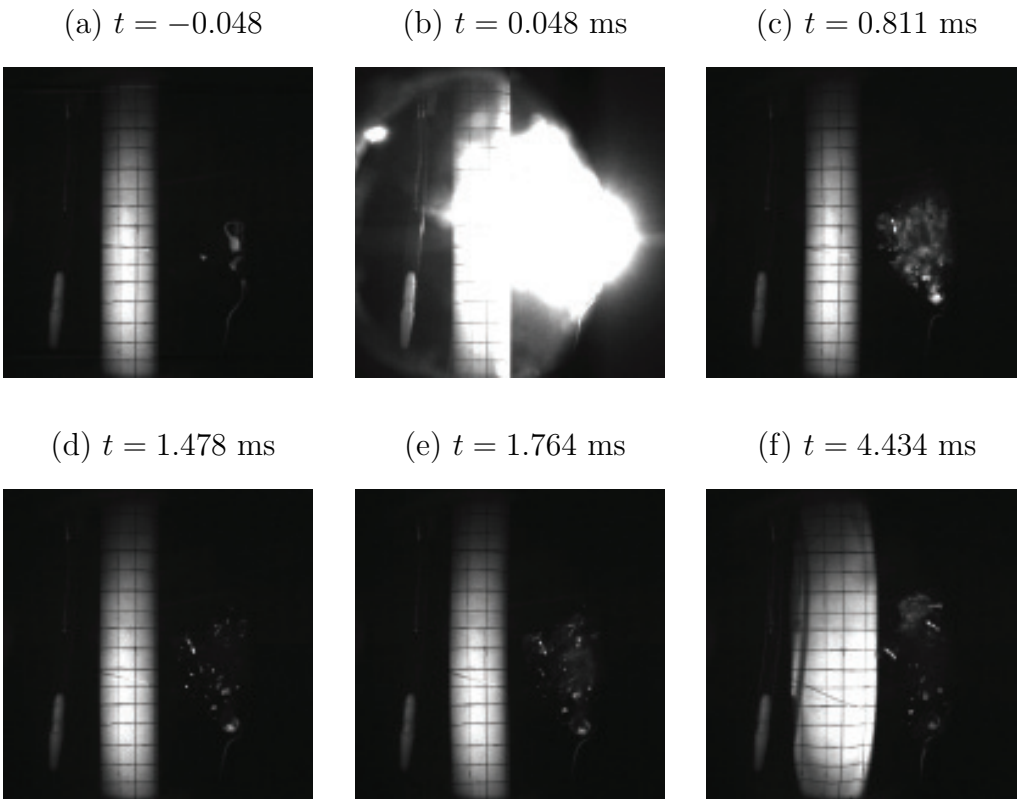

Figure 3.13: A sequence of images from the high-speed movie of AE05r01 (a) Start of the experiment. (b) Detonation of the RP-80. (c) First maximum bubble radius of the oscillating explosive gas bubble. (d) First minimum bubble radius of the oscillating explosive gas bubble. (e) The oscillating bubble is re-expanding. (f) Cylindrical shell structure collapses.

experimental run. In the final experiment, three repeated runs were documented using high-speed movies.

If the cylindrical model reached resonance with the explosion bubble, the structure could become unstable and implode. For cylindrical shell structures, the two likely modes of resonance are breathing and whipping. As seen in the high-speed movies, the cylindrical model oscillated for several periods before collapsing. From the high-speed movies, the oscillation frequency of the cylindrical model was measured and tabulated in Table 3.2 in the third column. The oscillation frequency of the gas bubble was also measured from the high-speed movies (shown in column five of the table). As expected, the frequency of the bubble oscillations and the cylinder oscillations are close in magnitude. One can speculate that the bubble drives the cylinder oscillations. An extension of this idea is that the bubble drives the cylinder to resonance. To test this idea, the natural frequencies of the cylindrical shells were computed in ANSYS for the breathing mode and bending (whipping) mode. These frequencies are tabulated in the second and third columns of Table 3.2, respectively. These natural frequencies of the structure are much higher than the frequencies measured from the experiments.

The calculation of the natural frequencies (breathing and whipping modes) of the cylindrical models was performed using an ANSYS model. Due to the complex geometry of the cylindrical shell structures (containing heavy end caps at both ends), a closed-form analytical solution is not possible. In order to provide some validation of the ANSYS calculations, the natural frequency of a slender cylindrical model ($L/D = 20$, where slender requires $L/D \geq 10$) was computed both in ANSYS and

by using Euler-Bernoulli beam bending theory. The resulting bending frequency for the slender cylindrical model (aluminum 6061 with no end caps, $D = 38.1$ mm, $w = 0.89$ mm) was 402 Hz in the ANSYS model and 406 Hz in the Euler-Bernoulli beam bending theory. These values are nearly identical. The cause of the deviation of these two frequencies can be attributed to the cross-sectional warpage that is taken into account in the ANSYS model and neglected in the Euler-Bernoulli beam bending theory. Due to the thin wall of the cylindrical model, neglecting the cross-sectional area warpage is not a good assumption.

The cylindrical models that are used in these experiments do not qualify as slender beams ($L/D \geq 10$), therefore, the linear Euler-Bernoulli beam theory is not valid. However, the Euler-Bernoulli beam bending theory was used to estimate the frequency of the cylindrical shell structure with a lumped mass at both ends to help verify the ANSYS results. The frequency calculated by ANSYS is tabulated in the table. The frequency calculated with Euler-Bernoulli beam bending theory was 1484 Hz (for AE05 models), which shows reasonable agreement to 1526 Hz calculated by ANSYS.

In addition to the vibrational modes of the cylindrical structure, the natural collapse pressure of the cylindrical models can be explored. The ambient pressure in the experimental facility was about 90% of the natural collapse pressure of cylindrical models. The high-pressure wave of the explosion exceeds the natural collapse pressure of the cylindrical model for a short time. In the natural explosion experiments, the pressure is raised quasi-statically. The time duration of the high-pressure wave of the explosion is much shorter in comparison. One pressure sensor was placed

Model	$f^{theory}_{\text{breathing}}$ (Hz)	$f^{theory}_{\text{bending}}$ (Hz)	$f^{meas}_{\text{structure}}$ (Hz)	f^{meas}_{bubble} (Hz)	Δt_{Pc} (ms)	w_{Pc} (cm)
BE25r01	N/A	N/A	N/A	794.8	N/A	N/A
BE05r01	2727.7	1199.2	666.7	983.6	0.08	11.7
AE05r01	2220.4	1526.3	789.5	800	0.165	24.6
AE05r02	2220.4	1526.3	833.3	800	0.16	23.8
AE05r03	2220.4	1526.3	769.2	1000	N/A	N/A

Table 3.2: A summary of the theoretical frequencies of breathing mode and bending mode of the structure compared with the measured frequency of the structure oscillation and measured frequency of the bubble oscillations. The amount of time and spatial width of the explosion pressure wave exceeding the natural collapse pressure.

at the same radial distance from the explosive as the cylindrical model. Therefore, the pressure versus time of the location of the cylindrical model is known. From this pressure record, the time duration that the peak pressure of the explosion exceeds the natural collapse pressure can be measured. These values are tabulated in Table 3.2 in column six. The final column in the table is the estimated spatial thickness of the pressure peak that exceeds the natural collapse pressure based on the time duration in column six and the sound speed in water. These thicknesses are listed in the last column of the table.

3.5 Conclusions and Future Work

Three experimental studies were conducted. The first experiment, conducted at low pressure, imploded due to impact from the re-entrant jet from the explosion bubble. The last two images shown in Fig. 3.3 show that this jet impact/implosion occurred during the second bubble collapse.

In the second set of experiments, the standoff distance between the explosive and cylindrical models was varied such that the gas bubble would not impact the

structure and no re-entrant jet was formed. In these second experiments, no high-speed movie was taken and the maximum value of d_0 for the model to collapse was found to be $d_0 = 8.6R_{\text{bub}}$. In these experiments, it was not known at what time after the explosion event the cylindrical model imploded, because high-speed movies were not taken (due to the limitation of the experimental facility). There was only one run (BE05r02) where a high-speed movie was taken, which shows the cylindrical model imploding much later (2 ms later) than the shockwave arrival to the structure. There was no significant difference in the pressure records for runs when an implosion occurred and did not occur. This suggests that the implosion signature is lost in the multiple reflections of the shockwave and bubble pulsations.

In the final set of experiments, the collapse of models with different geometry and material was investigated under similar loading conditions. Despite the difficulty in obtaining exact model and pressure sensor placement and in obtaining repeatable explosions, the high-speed movies show that the timing of the characteristic events are repeatable to within 48 to 96 microseconds (one or two movie frames). The cylindrical model, as seen in the high-speed movies, oscillated for several cycles before collapsing. These oscillations were driven by the oscillating explosion gas bubble. From the movies, a transverse (whipping) mode vibration was observed. However, it was not clear whether a breathing mode vibration also existed. The oscillation frequency was measured from the high-speed movies and was found to be about half the natural frequency for the whipping mode and one third of the natural frequency of the breathing mode (as determined by ANSYS calculations).

The time duration of the peak pressure from the explosive that exceeded the

natural collapse pressure of the cylindrical models was measured from the pressure records. These times give a lower limit for the amount of time the local pressure around the model is above the natural collapse pressure of the model. In these experiments, the pressure at the location of the cylindrical model exceeded the natural collapse pressure for about 0.16 ms. During this time, the cylindrical model did not collapse even though the pressure was significantly higher than the natural collapse pressure. In fact, the peak pressure was at least 4.5 times higher than the natural collapse pressure of the model. The aluminum cylindrical models did not collapse until 4 ms after the high-pressure wave passed.

In the future, it is suggested that these experiments be carried out in the field, where reflections of the pressure waves from the boundary will not be present. Additional parameters can be varied in the experiments such as ambient pressures and size of explosives.

Chapter 4
The Impact of a Plunging Breaker on a Partially Submerged Cube
4.1 Abstract

The impact of a plunging breaking wave (wavelength ≈ 1.2 m) on a partially submerged cube (with dimensions $L = 0.3048$ m) is studied experimentally. The free surface shape upstream of the cube during the wave impact was measured with a cinematic Laser-Induced Fluorescence (LIF) technique employing a high-speed digital camera, a laser light sheet and fluorescent dye mixed with the water. Measurements were taken with the cube submerged by $0.5L$ at three horizontal positions ranging from $x_{cube} = x_b - 0.28$ m to $x_{cube} = x_b - 0.13$ m, where x_b =6.75 m is the breaker location in the absence of the cube as measured from the back face of the wedge of the wave maker (The breaker location is defined here as the horizontal position of the jet tip as it hits the front face of the wave). Measurements were also taken with the cube submerged by $0.3L$ at one horizontal position, $x_{cube} = x_b - 0.28$ m. Within the range of positions that were explored, the wave impact behavior fell into two categories. In the first behavior category, which occurred with the cube in the two horizontal positions closest to the wave maker for both depths of submergence, the free surface between the front face of the cube and the wave crest forms a circular arc that converges to a point and then forms a high-velocity vertical jet (speeds ≈ 3 m/s). In the second category, which occurred with the cube at the farthest position from the wave maker, the plunging jet begins to overturn and impacts the front face of the cube. It was found that for the cube positions

with category one wave impact behavior, the evolution of the water surface shape between the cube and the wave crest was nearly identical.

4.2 Introduction

4.2.1 Literature Review

The impact of large-amplitude water waves on structures has been investigated by a number of researchers. The literature on wave impact on vertical walls mounted to the bottom boundary in shallow water has been reviewed by Peregrine [44]. Wave breaking is a strongly nonlinear transient two–phase process that is not easily modeled with rigorous theoretical or numerical treatments and makes well-controlled repeatable experiments very difficult. In fact, it was not until the 1970s that accurate numerical modeling of the overturning of a water wave (without the presence of a nearby structure) was achieved using potential-flow, boundary element calculations, see for example Longuet-Higgins and Cokelet [33], Cooker and Peregrine [20] and Dold and Peregrine [25]. When an incident wave has a small slope (i.e., when the wave height over the wavelength is vanishingly small), linear theory gives a good description of the impact of the wave on the wall, including the pressure on the wall [44]. However, when the incident waves are even moderately steep the wave impact and wall pressure cannot be accurately predicted by linear theory.

Without the presence of a wall, a plunging breaking wave can occur when, due to various nonlinear effects, the wave steepens rapidly forming a jet that curls over and plunges back into the front face of the wave. If a bottom-mounted vertical wall is placed in the flow field, the breaking process can change dramatically depending

on the location of the wall. If the wall is placed where the wave is most vertical, an identical wave will be changed dramatically. The water surface at the contact point on the water is pushed upward by the wall. This rising water causes the height of the crest (measured as the vertical distance from the water surface contact point on the wall to the wave crest) to reduce progressively; the water surface appears as if it is converging to a point. Peregrine [44] predicted vertical accelerations of the water at the wall to exceed $1000g$ (where g is gravity), when the water surface approaches the convergence point. This would require pressure gradients exceeding $1000\rho g$ (where ρ is density). From these gradients, Peregrine estimated wall pressures much greater than $10\rho g\,(h + H)$, or 10 times the hydrostatic pressure at the bottom, where h is the height of the crest measured from the still water level and H is the depth of the still water. It is important to note that high pressures are attributed to the convergence of the surface to a point, as there is no plunging jet formed to impact the wall at this wall position. Due to the high vertical accelerations, a violent vertical jet is formed at the convergence point. Peregrine named this phenomenon *flip-through*.

Chan and Melville [16] observed three different wave impact behaviors, including flip-through. They conducted an extensive experimental study of the impact of deep-water waves (wavelength much less than the water depth) on a vertical wall that spanned the width of the tank and extended to the tank bottom. In their experiments, three distinct wave impact behaviors were observed based on the position of the wall relative to the breaking point of the wave: (I) a region of wall positions where a strong vertical jet is formed during impact and high impact pressures are

observed (flip-through), (II) a transition region where a jet forms and hits the wall, entrapping an air pocket; and (III) a region where the crest has already plunged into the fluid before impacting the wall and a double-peak impact pressure record is observed due to a secondary jet impacting the wall ahead of the crest. It should be noted that Peregrine's [44] two-dimensional numerical calculations and Chan and Melville's [14, 16] experiments exhibited flip-through behavior even though the incident wave generation was very different. Another difference between the simulations and experiments was the presence of bubbles and droplets in the experiments, which are likely caused by surface tension, three-dimensionality of the flow and the boundary layer on the wall.

The pressure on a wall during wave impact can be attributed to both the hydrodynamics of the wave impact that causes high impulsive pressures and the dynamics of entrained air (to be discussed in more detail later). The peak pressure is dominated by inertia and lasts for about 1 millisecond in the laboratory and 10-100 milliseconds in the ocean [44].

Chan and Melville [16] found large variability in the observed pressure records in repeated runs in their experiments, which they attributed to varying amounts of air entrained from the wave breaking process. According to Peregrine [44], this variability can also be attributed to small disturbances, such as surface roughness on the wall or small residual surface waves and water motion from previous experimental runs that can reduce the impact pressures. Early researchers, Bagnold [2] and Richert [48], also saw variability in peak pressure measurements. They were the first to compute the pressure impulse of wave impact and found it to be a more re-

peatable metric than the pressure alone. The pressure impulse is simply the integral of the pressure over the time duration of the impact,

$$P(\mathbf{x}) = \int_{t_{before}}^{t_{after}} p\left(\mathbf{x}, t\right) \mathrm{d}t. \tag{4.1}$$

Because the peak pressure occurs in such a short time scale, the nonlinear, gravity and viscosity terms become negligible compared to the local acceleration and pressure gradient terms from the equation of motion. The resulting equation,

$$\rho \frac{\partial \mathbf{u}}{\partial t} + \nabla p = 0, \tag{4.2}$$

is simpler to integrate over the appropriate domain for pressure impulse models.

Cooker and Peregrine [20] developed a pressure impulse model by using a simplified wave shape consisting of a step function in water, height H, during a constant-velocity (U) impact with a vertical wall. They found a relatively small pressure impulse, $0.54\rho UH$ per unit length of the wall. This low pressure impulse is attributed to the effect of the constant pressure of the free surface behind the step. This result indicates that the shape of the wave at distances more than $0.5H$ from the wall is not important. Experimental studies, undertaken by Chan [15], show that the pressure-impulse estimates of Cooker and Peregrine have some limitations. Using the pressure-impulse field to estimate the pressure field, it was found that the most violent peak pressures have a maximum of $2P/\Delta t$, where P is the impulse as defined in Eq. 4.1.

Using a two-dimensional pressure impulse model, Cooker and Peregrine [21] showed that the pressure impulse decays logarithmically with depth down the wall

for the limiting case of infinite water depth. Wood and Peregrine [63] obtained results for three-dimensional pressure-impulse models and found the forces and pressures are reduced compared to two-dimensional impact [44]. Other solutions using the pressure-impulse model include the effects of the proximity of other surrounding rigid boundaries (studied by Peregrine and Kalliadasis, [45] and Wood and Peregrine [62, 63]) and the effect of the porosity of the breakwater (modeled by Wood and Peregrine [64]).

During a wave impact event, air can be entrained when the wave breaks before impacting the wall or when the plunging jet impacts the wall before breaking thus entrapping a pocket of air. The compressibility of this air pocket can cause two features in the pressure record on the wall: first, an increase in the time duration of the pressure peak (and a decrease in the magnitude of the peak) and second, pressure oscillations following the peak [44]. Peregrine [44] explains that the increase in the time duration of the pressure peak can be attributed to the extra time it takes to compress and re-expand the trapped air pocket. The trapped air bubble acts as a elastic spring. Water rebounds or "bounces-back" imparting an increased pressure impulse on the wall. Wood et al. [65] experimentally measured an increased pressure impulse on the wall when an air pocket was present. Laboratory experiments have shown that oscillations in pressure following the peak are related to the trapped air [44].

Wave impact studies by Bagnold [2], Chan and Melville [16] and Peregrine [44] suggest that the highest impact pressure peaks are produced when the least amount of air is entrapped. Subsequent studies afterward have confirmed Bagnold's

observations, see Richert [48], Blackmore and Hewson [5], Kirkgöz [36, 49], Hattori et al. [32] and Bullock et al. [8]. During a flip-through wave impact, which by definition forms no air pocket, some of the energy from the incoming wave is converted into the upward jet. In cases when an air pocket is entrapped by the incoming wave, energy that would have gone into the upward jet is instead used to break up the air pocket. This might lead to a reduction in the jet height [44].

Bagnold was the first to propose an air pocket model. The model was based on the adiabatic compression process of a pocket of entrapped air between a breaking wave and a solid structure. The water surface slows down as it compresses the air pocket, creating a high pressure zone in the air pocket, which can give rise to a Raleigh-Taylor instability. Simple linearized models of the acoustic modes for a semicircular air pocket were constructed by Topliss et al. [57] and Zhang et al. [68]. It was found that the oscillation period of the air pocket compared well to experimental observations.

Bullock et al. [9] conducted experiments with both salt and fresh water in the same wave flume for cases where an air pocket is entrapped during wave impact. They found that though the pressure peaks were reduced by 10% in salt water, the pressure-impulse remained nearly the same compared to fresh water.

Lamarre and Melville [39] and Bullock et al. [8] measured a wide range of air-volume fractions in breakers generated in the laboratory and those found in the field. They concluded that there are difficulties in scaling the air volume fractions between laboratory and field conditions and suggest that simple Froude scaling is not sufficient.

A number of wave impact studies were directed toward assessing the effectiveness of breakwaters for protection against damage due to tsunamis. Oshnack et al. [42] conducted a large-scale experimental study of the effectiveness of small seawalls. Lukkunapasit and Ruangrasamee [40] found that low retaining walls (1 m high) were effective at dissipating tsunami energy. Dalrymple and Kreibel [23] discussed the idea of the upward splash of the wave impact deflecting the wave momentum upward and thus reducing damage to structures on the other side of the seawall. They observed that there was increased damage after a tsunami at positions directly behind the pedestrian openings in seawalls, confirming that the seawalls do in fact deflect the wave and reduce damage.

4.2.2 Present Work

In the present work, the impact of a breaking wave on a partially submerged cube (dimensions $L = 0.305$ m) was explored in a wave tank (14.8 m long, 1.15 m wide with a water depth of 0.91 m). Two-dimensional plunging breakers were produced in deep water by a dispersive focusing method that is similar to Rapp and Melville [47]. Only one wave maker motion was used in all the experiments. The impact the wave on the cube was studied with the cube placed at a number of horizontal positions relative to the breaker location (without the cube in the tank) and two depths of submergence. It is important to note that the cube does not span the entire width of the wave tank or extend to the bottom of the tank. Therefore, the wave impact problem is three-dimensional, and the physics of the wave impact process are different from those in the works cited previously where a two-dimensional

problem was analyzed with a wall that extended to the bottom of the tank. In the present experiments, only wave impacts in Regions I and II (from Chan and Melville's [16] description of wave impact behavior) were observed. Wave profiles were measured with a cinematic Laser-Induced Fluorescence (LIF) technique that utilized two synchronized high-speed cameras at two viewing angles. The evolution of the water surface shape in front of the cube, including the position and velocity of the water contact point on the vertical centerline of the front face of the cube are analyzed. Pressure measurements were not performed here, but will be discussed in the Future Work section (Sec. 4.5)

4.3 Experimental Details

In the present section, the wave tank (Sec. 4.3.1), the wave generation technique (Sec. 4.3.2), the wave profile measurement technique (Sec. 4.3.3), the repeatability of the wave generation process (Sec. 4.3.4) and the outline of the experiments (Sec. 4.3.5) are discussed in detail.

4.3.1 Deep-Water Wave Experimental Facility

The experiments are performed in a wave tank that is 14.8 m long, 1.1 m wide and 2.2 m deep with a water depth of 0.91 m. The waves are generated by a programmable wave maker consisting of a vertically oscillating wedge that is located at one end of the tank, see Fig. 4.1. The front face of the wedge is tilted forward by 30° (the normal to the front face points downward at angle of 30 degrees from horizontal) and the back face of the wedge is vertical and very close to the end wall

of the tank. The wedge was driven by a ball-screw and servo-motor mechanism. A computer-based feedback control system was used with a position sensor and a tachometer to control the motion of the wedge precisely. The wave maker motion is repeatable within $\pm 0.1\%$ in amplitude from run to run. Consequently, highly repeatable breaking waves are obtained in the tank.

A sloped beach is located at the end of the tank opposite to the wave maker. For the current experiments, the beach is used mainly to expedite calming of the water surface between experimental runs.

The wave tank also includes an instrument carriage that rides on precision rails mounted to the tops of the long side walls of the tank, see Fig. 4.1. Most of the wave measurement equipment was mounted on the carriage, which was held stationary during each experimental run.

Water treatment is critical in the present experiments for two main reasons. First, in the photographic LIF measurements of the free surface profiles, dust and particles on the free surface can produce inaccurate measurements. Second, the presence of surfactants can affect the behavior of the waves and the impact process. In order to maintain a clean water surface, a surface skimmer and diatomaceous-earth water filtration system was used between experimental runs. In this system, the skimmer is placed behind the beach, see Fig. 4.2, and the water is returned to the tank at the opposite end of the tank after filtration. The wave impact experiment was run at intervals of 30 minutes. In between runs, the filtration system was turned on for about 10 minutes and then turned off for 20 minutes to allow the residual water motions to subside.

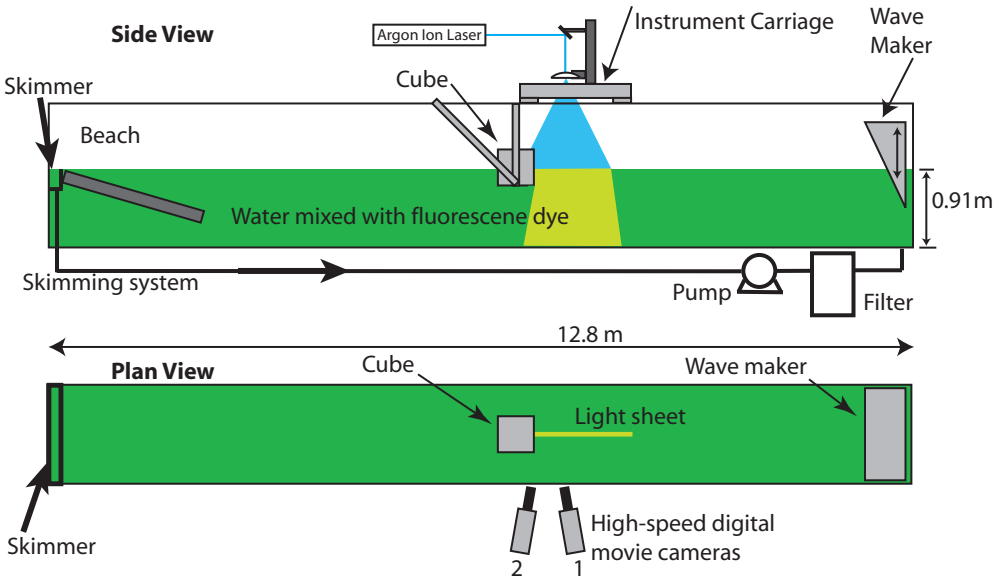

Figure 4.1: A schematic showing the tank, the wave maker, the cube and the lighting setup from the cinematic LIF measurements of the water surface profiles.

4.3.2 Wave Generation Technique

Water waves steepen and break due to energy input from the wind, nonlinear instabilities, directional energy focusing, dispersive focusing, interaction with current systems, and shoaling. The most common way of generating deep-water breaking waves in a laboratory wave tank is to use dispersively focused wave packets. This method provides the greatest control over breaking location and strength.

Dispersive focusing uses a frequency-modulated packet of waves that is generated by a mechanical wave maker. The wave packet must have high-frequency waves generated at the beginning of the packet and low-frequency waves at the end of the packet. Due to the frequency dispersion of water waves, the low-frequency waves, which have high phase speeds, catch up in space and time with the high-frequency waves, which have a lower phase speed. As the packet propagates, the entire wave

packet will focus to a narrow region of time (t_b) and space (x_b). The result is essentially one wave that contains the energy of all the waves initially in the packet. The concentration of energy in such a small region causes the wave to become very steep and leads to breaking if the initial waves are steep enough.

Longuett-Higgins [33] derived the basic technique of calculating the required distribution of wave frequencies in time that will converge at the breaking distance (x_b) at the same time using linear theory. Other researchers have modified Longuett-Higgins' technique. Davis and Zarnick [24] solved the inverse of the classical Cauchy-Poisson initial water surface elevation problem to calculate the wave packet that, if reversed in time, will eventually converge to a steep wave.

The breaking waves in this study were generated by the dispersive focusing method proposed by Longuet-Higgins [33] and later modified by Rapp and Melville [47]. This wave generation method has been used in a number of earlier studies in the Hydrodynamics Laboratory. The wave packet consists of the sum of N sinusoidal components and the wavemaker motion to produce these waves is given by

$$z_w = W(t)\frac{2\pi}{N}A\sum_{i=1}^{N}\frac{1}{k_i}\cos\left(x_b\left(\frac{\omega_i}{\bar{c}}-k_i\right)-\omega_i t+\frac{\pi}{2}\right), \tag{4.3}$$

where $W(t)$ is a window function which is described below, A is an adjustable constant called the wavemaker amplitude, x_b is the horizontal position of the breaking event (by linear theory) measured from the back of the wedge, t is time, k_i and ω_i are, respectively, the wavenumber, and frequency of each of the $i = 1$ to N wave components ($\omega = 2\pi f$ where f is the frequency Hz), and $\bar{c}$ is the average of the group velocities ($c_i = 0.5\omega_i/k_i$) of the N components. The frequencies are equally

spaced, $\omega_{i+1} = \omega_i + \Delta\omega$, where $\Delta\omega$ is a constant. The window function was chosen to give the wedge zero motion at times when the summation of components resulted in only a very small motion:

$$W(t) = 0.25(\tanh(\beta\bar{\omega}(t - t_1)) + 1)(1 - \tanh(\beta\bar{\omega}(t - t_2))), \tag{4.4}$$

where β is a constant that determines the rise rate of the window function, chosen as 5.0, and $\bar{\omega}$ is the average of the N frequencies, ω_i. The window function is nearly equal to 1.0 for most of the time between $t = t_1$ and $t = t_2$ and is zero at other times [27]. The times t_1 and t_2 were chosen to allow the lowest and highest frequency components ($i = 1$ and $i = N$, respectively) to be generated and to travel to position x_b:

$$t_1 = x_b\,(1/\bar{c} - 1/c_N)\,, \tag{4.5}$$

$$t_2 = x_b\,(1/\bar{c} - 1/c_1)\,. \tag{4.6}$$

In the wave maker motion equation (Eq. 4.3), the parameters within the argument of the cosine term are chosen from linear theory, while the other parameters were obtained by trial and error with the goal of producing a violent plunging breaker when the cube was not installed in the tank. The result was a strong plunging breaker generated from a wave packet with an average frequency, $f_0 = 1.15$ Hz. For this breaker, $N = 32$, $h/\lambda_0 = 0.35792$ (where h is the vertical distance between the mean water level and the vertex of the wedge and $\lambda_0 = 2\pi g/\bar{\omega}^2$, where g is gravitational acceleration), $H/\lambda_0 = 0.486$ (H is the mean water depth in the tank), $x_b/\lambda_0 = 10.0$, $N\Delta\omega/\bar{\omega} = 0.77$, and $A/\lambda_0 = 0.074$. The resulting profile of wedge height versus time that was used as the input to the wavemaker is shown in Fig. 4.2.

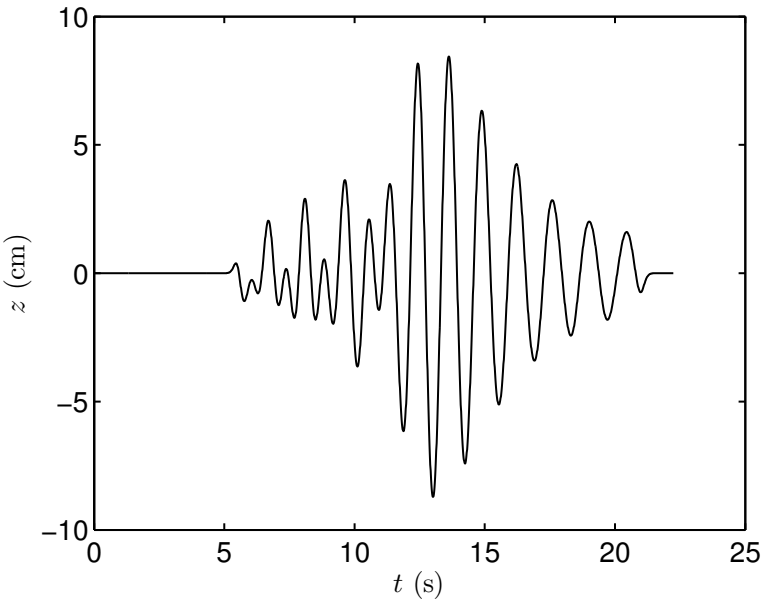

Figure 4.2: The wavemaker input showing the vertical height of the wavemaker versus time.

For deep water wave packets, linear theory gives a good prediction at positions close to the wave generator. As the wave packet moves down the tank, the wave amplitudes increase and the linear theory produces inaccurate results. Dommermuth et al. [26] developed a numerical model that simulates the wave generation and breaking process (up to plunging jet impact) using potential flow analysis. This model uses a high-resolution refined mixed Euler-Lagrangian solution scheme ignoring the effects of surface tension. The fully nonlinear calculations provide a more accurate prediction than linear theory as the wave approaches breaking.

4.3.3 Wave Profile Measurements

All wave profile observations and measurements were made photographically. White-light videos were obtained to qualitatively analyze of the wave-cube interaction. Videos using Laser-Induced Fluorescence (LIF) illumination were used to

obtain quantitative measurements of the surface wave profile evolution during the impact with the cube.

In the LIF measurements, a 6-Watt Argon-Ion laser operating at 5 W was directed through a series of optical lenses and mirrors to the top of the carriage. From the top of the carriage, a mirror, two spherical lenses and a cylindrical lens were used to direct the beam downward and deform it into a 1-mm-thick vertical sheet as it hit the water surface. The light sheet was centered along the width of the wave tank and expanded in the stream-wise direction, as shown in Fig. 4.1. The cameras were focused on the the intersection of the light sheet with the mean water level. Fluorescent dye was mixed into the wave tank in order to make the laser light sheet visible at the water surface. Two high-speed cameras (Phantom v640, Vision Research, Inc) were mounted on the instrument carriage. The cameras were mounted above the water surface, making a shallow viewing angle of 5° to 10° relative to the horizontal. Long-wavelength-pass optical filters were placed in front of the camera lenses. These filters absorb the laser light reflected from the water surface and pass the light from the glowing dye. The first camera was pointed slightly downstream and provided a view of the front and back of the propagating wave as the wave approached the cube. The contact point of the water surface and the cube is seen in this view as well as the resulting vertical splash after impact. However, when the wave begins to overturn and break, the plunging jet of the wave sometimes obstructs the view of part of the front face of the wave. The second camera was mounted to face slightly upstream and provided the missing view of the front face of the approaching wave. The second camera does not show the contact

point or the back of the wave. The two views together provide a complete picture of the wave breaking event at all times.

The cameras were set to take images at a rate of 300 frames per second with a resolution of 2560 by 1600 pixels with 12-bit gray levels. The cameras were synchronized in time and were set to start recording movies at the start of the wave maker control program. To initiate this camera image capture sequence, a switch closure was sent from the computer that controlled the wave maker to a delay box (Berekley Nucleonics) when the wave maker control program was activated. The delay box waited a specified delay time (for the experiments discussed, this ranged from 16 to 20 seconds based on the cube position) before sending a 5-Volt Transistor-Transistor Logic (TTL) signal to a function generator. The function generator then commenced sending a series of square waves with the desired frequency of the cameras. At each rising edge of the square wave, the two cameras recorded images. Using this external clock image sequencing allows precise control of the synchronization of the two cameras. It is important to note here that there was a delay caused by the computer between the time at which the button was pushed to initiate the wave maker program and the time at which the camera was triggered. This delay time was 0.12 seconds and was measured by comparing a high-speed video of the wave maker motion to the wedge motion as measured by the wave maker position sensor and recorded by the computer that controls the wave maker.

In order to process the data from the cameras, calibration images of a checkerboard were taken from both cameras – an example is shown in Fig. 4.3. The checkerboard was held in the same vertical plane that is occupied by the light sheet during

the LIF movies. These calibration images were used to find the number of pixels per centimeter, distortion caused by the viewing angle, and mean still water level. Fig. 4.4 shows a mapping from image units (pixels) to physical units (centimeters) from the checkerboard corner points found in Fig. 4.3. The mean water level in the calibration images was determined by fitting a straight line to the set points determined by eye to represent the contact line of the water surface on the calibration board. Additionally, the calibration images allow a map of physical locations in the image plane to be made from one camera to another in order to combine the results of both cameras. Before each run, still frames of the flat surface with the laser light sheet shining on the water surface were taken to confirm the mean water level for each experimental run.

The images from the high-speed movies were downloaded to a desktop computer and an in-house Matlab code was used to process the images. The image processing starts with the adjustment of the image contrast before applying the Matlab function "Edge." A threshold value of the intensity gradient magnitude was chosen, and the edge function outputs an array of the same dimensions as the image with each pixel either 1 (a pixel with gradient magnitude above the threshold level) or a 0 (a pixel with gradient magnitude below the threshold level). Because the cameras were focused at the air-water interface that shows a sharp edge between the black air and the white water in the LIF images, the gradients at the water surface become very high.

A search algorithm was used to find the first point on the air-water interface starting on the right side of the image, then a nearest-neighbor algorithm was used

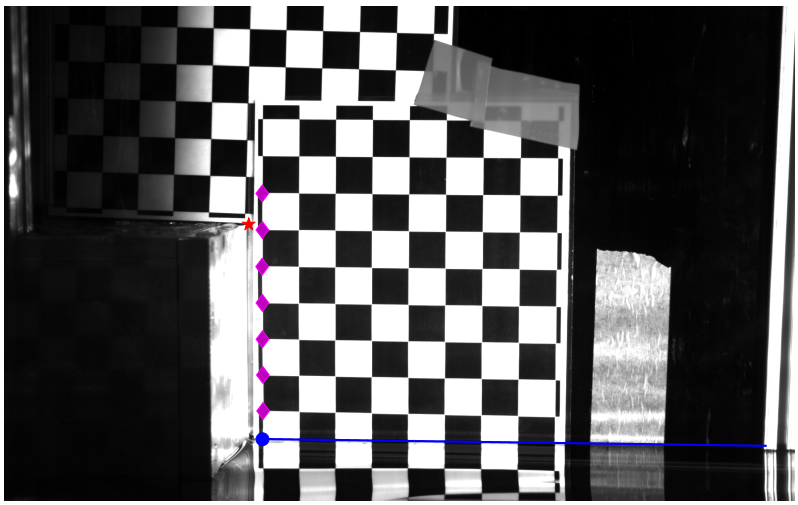

Figure 4.3: One calibration image (from camera 1) showing the checkerboard calibration grid and the mean still water level. The magenta diamonds show the corner points, the red star shows the point where the top edge of the cube passes through the plane of the calibration board, and blue circle shows a point on the mean water level below the corner points. The point corresponding to the red star is known to be 15.24 cm above the mean water level. The straight blue line was fit to the set of points determined by eye to represent the contact line of the water surface in the plane of the board.

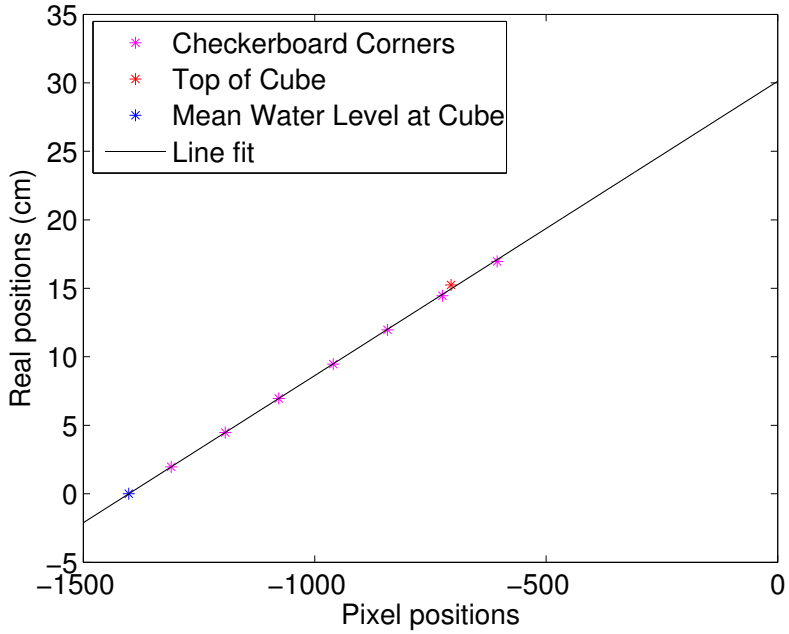

Figure 4.4: Calibration curve using the points taken from Fig. 4.3. A line was fit to these points in order to map the edge from the post-processing to real physical units.

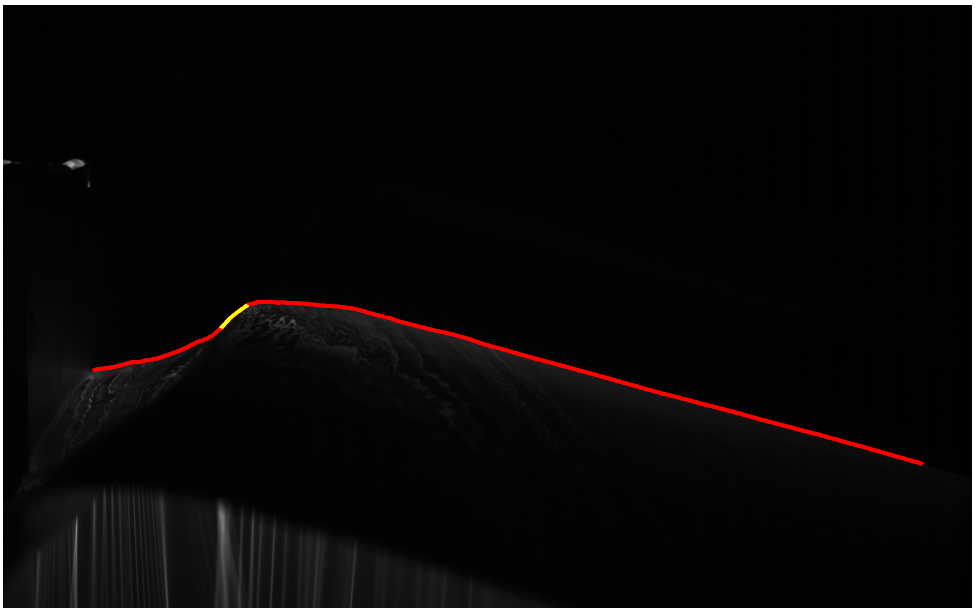

Figure 4.5: An example of the edge-detection technique showing the free-surface as detected by the edge-detection technique (red line) and the region where the free surface was approximated by a spline-fit (yellow) because it was obscured from the view of the camera..

to find the connecting points on the air-water interface until the front face of the cube was reached. If there was a disconnect in the free surface profile caused by a part of the wave surface obscuring the wave profile at the plane of the light sheet, a spline-fitting algorithm, requiring user-input to connect the discontinuity, was used. Fig. 4.5 shows a sample image where spline-fitting was used (shown in yellow).

4.3.4 Repeatability of Wave Generation

In order to demonstrate the repeatability of the wave generation in the wave tank, wave height versus time at two points in the tank were measured without the cube in the facility. Rather than using wave gauges, the LIF camera system was used as an overly robust method of taking these measurements. One LIF camera

was mounted on the instrument carriage using the same laser light sheet setup as described in Sec. 4.3.3. The carriage was moved to each measurement location relative to the wavemaker, and a checkerboard calibration target was used not only to calibrate the images to physical units, but also, by lining up the checkerboard relative to known locations on the tank, to precisely determine the position of the image relative to the wave maker.

LIF movies were processed using the technique described in Sec. 4.3.3. Because the water surface height was only required at one point, an average of seven the surface heights in pixel columns covering a horizontal distance of 0.8 mm along the light sheet was for the output "wave gauge" measurement shown in Fig. 4.6.

Fig. 4.6 shows the water surface elevation at the streamwise positions of (a) 561.8 cm and (b) 670.5 cm from the back edge of the wavemaker. Note that in Fig. 4.6 (a), there is a break in the curve that was due to the water surface moving below the image eld of view. As can be seen in the figures, the water surface versus time records are quite repeatable from run to run. Measurements of the maximum elevation in each run indicate a range of only 0.07 cm with a mean value of 8.68 cm for the 561.8 cm streamwise position and a range of 0.11 cm with a mean value of 8.35 cm for the 670.5 cm streamwise position.

4.3.5 Plan of Experiments

Table 4.1 shows a summary of the cube positions used in this study. For all runs, the same plunging breaking wave, discussed in Sec. 4.3.2, was used. The parameters that were varied in the experiments were the streamwise (x_{POS}) position

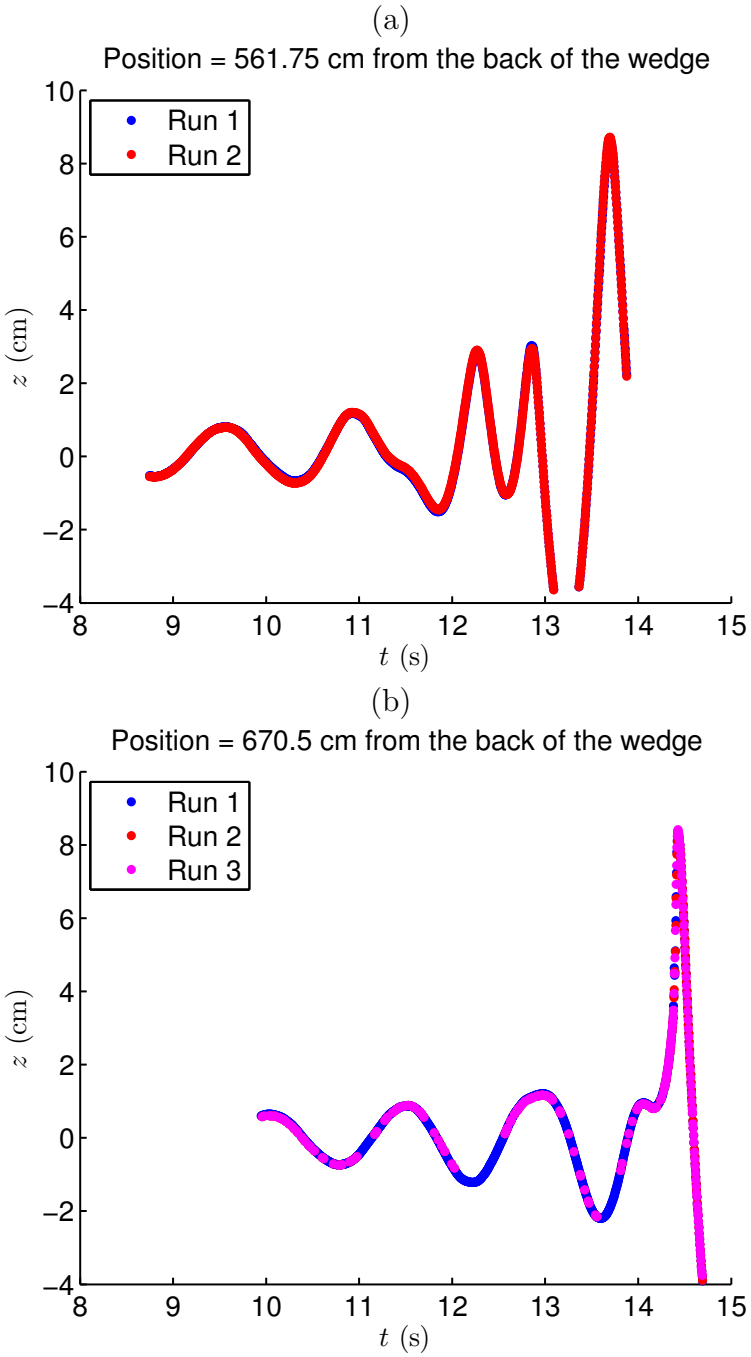

Figure 4.6: Repeatability of wavemaker without the presence of the cube in the tank. Water surface elevation, z verus t, where z is the free surface position referenced from the mean still water level and t is the time elapsed from the moment the wave maker input program is initiated, for positions (a) $x = 561.75$ cm (2 repeated runs) and (b) $x = 670.5$ cm (3 repeated runs) from the back edge of the wavemaker. Note that in (a), there is a break in the curve that was due to the water surface moving below the image field of view.

Position Number	x_{pos} (cm)	z_{pos} (cm)	Impact Region	# of Repeat LIF Runs
1	642	0	I	4
2	642	5.7	I	3
3	647	0	I	3
4	657	0	II	3

Table 4.1: A summary of the cube locations used in this study. The x_{pos} is the stream-wise position of the front face of the cube relative to the back of the wave maker. The z_{pos} is the height of the center of the cube relative to the mean water level. The next to last column, Impact Region, refers to the three regions defined by Chan [16] that are listed in Sec. 4.2.

measured from the back of the wedge wave maker to the front face of the cube and the depth of submergence (z_{pos}) measured as the vertical distance from the center of the cube to the mean water level. When $z_{\mathrm{pos}} = 0$, the center of the cube is at the mean water level and the cube is halfway submerged. The last column, "Impact Region," refers to the three regions defined by Chan and Melville [16] discussed in Sec. 4.2. Within the range of these experiments, most of the data fell in Region I, while for one cube position, it fell into Region II.

4.4 Results and Discussion

The results obtained for each of the four cube positions will be discussed in Secs. 4.4.1 through 4.4.3. These results include snapshots taken from white-light movies for both camera views and LIF measurements of the water surface evolution. Although two cameras were used to take LIF measurements of the wave impact event, only the movies from camera 1, which show the water contact point on the front face of the cube were analyzed, since they give a good view of nearly all of the wave profile. In Sec. 4.4.2, the convergence of the wave surface profiles to a

point (flip-through) are discussed for the Region I impact events and the case with Region II impact is discussed in Section 4.4.3. Measurements of the positions of the contact point between the front face of the cube and the free surface are presented in Sec. 4.4.4.

4.4.1 Region I Results

For three of the cube positions explored, the wave-cube interaction exhibited a Region I-type behavior. As the wave approaches the front face of the cube, the region between the wave crest and the cube surface forms an arc due to the influence of the wall not allowing the water to move in the streamwise direction. As the wave progresses toward the cube face, this arc closes and a jet forms with vertical velocity, parallel to the cube face (flip-through).

A sequence of four images from one white-light movie of the impact of the wave with the cube located at cube Position 1 is shown in Fig. 4.7. The interval between frames is 33.33 ms. The images were chosen such that the time instances at (c) coincides with the time that the curvature of the water surface changes to the upward jet, defined here as the moment of wave impact. Figs. 4.8 and 4.9 show similar sequences of eight images for Positions 2 and 3, respectively. Fig. 4.8 (a) - (d) show the view from camera 1, and Fig. 4.8 (e) - (h) show the view from camera 2, where each row corresponds to the same instant in time. The interval between frames is 33.33 ms. The images were chosen such that the time instances at (c) and (g) coincide with the time that the curvature of the water surface changes to the upward jet, defined here as the moment of wave impact.

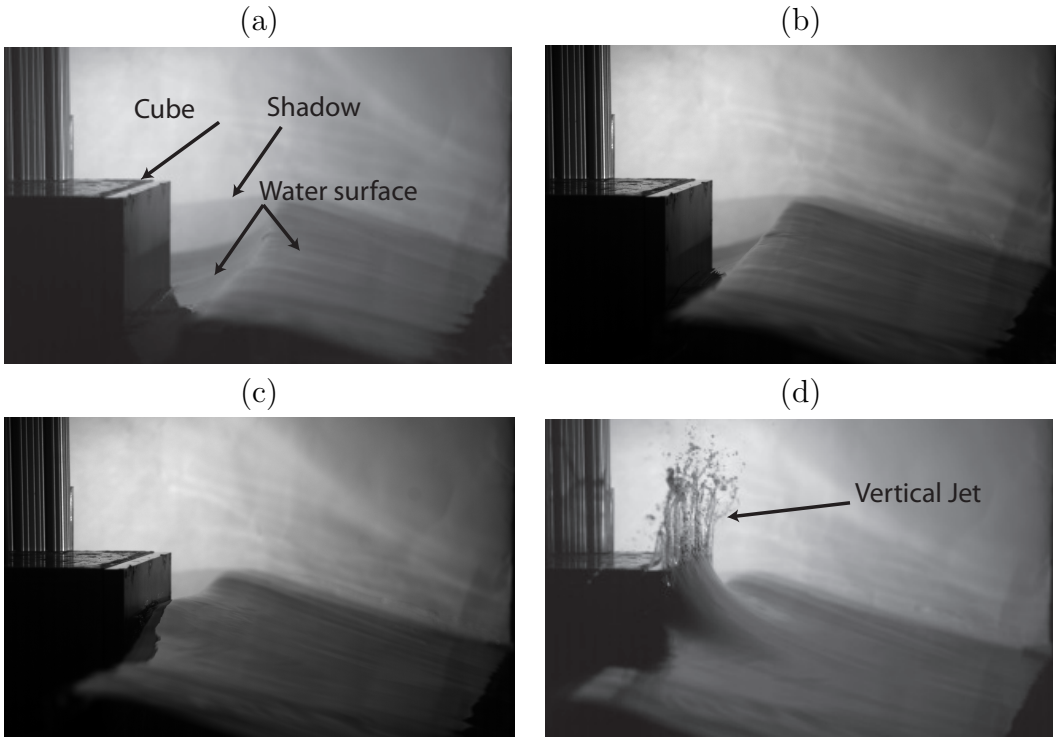

Figure 4.7: A sequence of four images from one high-speed movie (from camera 1) of the impact of a breaking wave on the cube at Position 1. In this cube position, the free surface between the water contact point and the wave crest focuses to a point (image c), thereby, creating a fast-moving vertical jet. The time interval between the photographs in 33.333 ms.

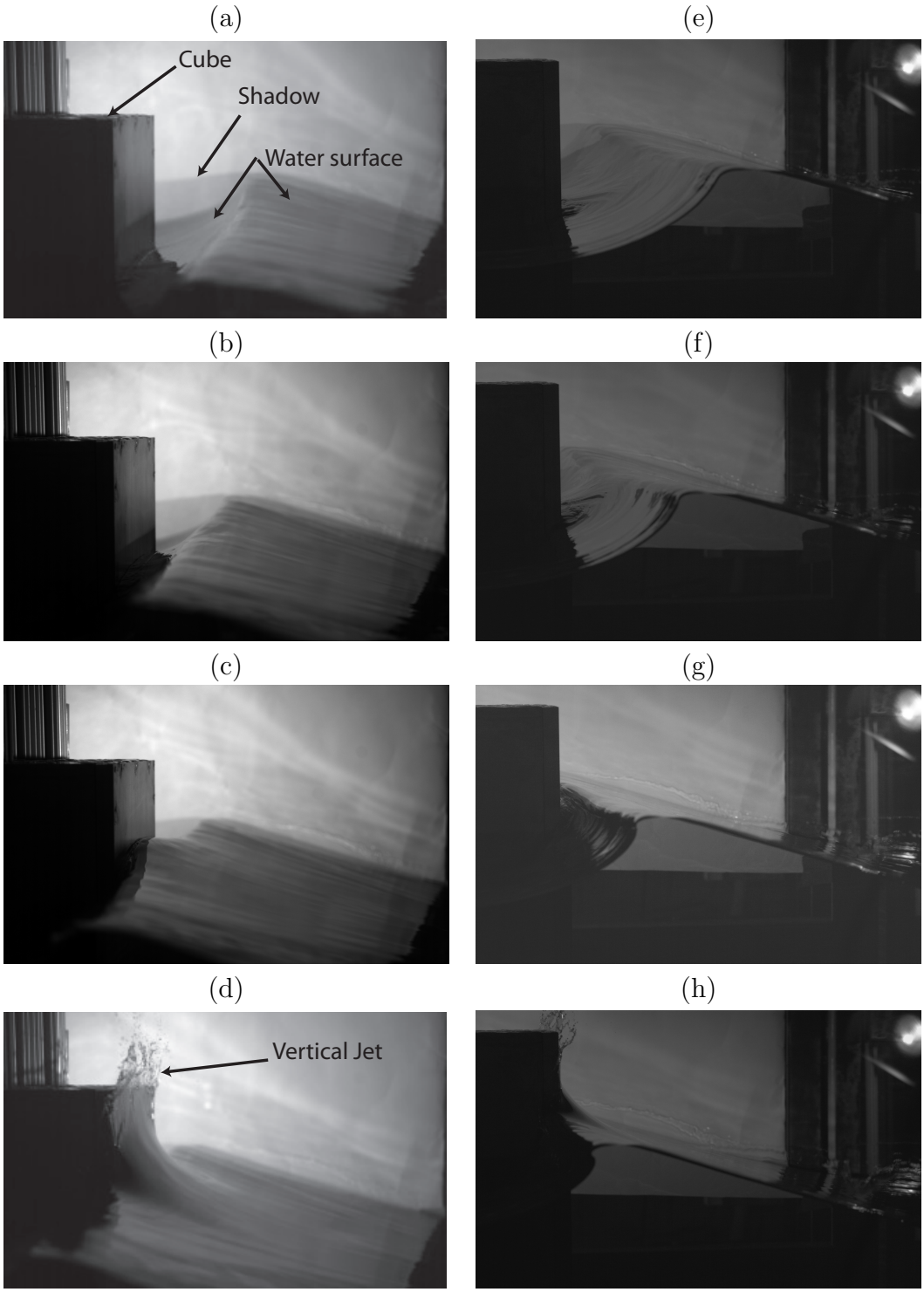

Figure 4.8: A sequence of eight images from two high speed movies of the impact of a breaking wave on the cube at Position 2. The left-hand side shows images taken with camera 1, while the right-hand side shows images taken with camera 2. The time interval between the photographs in 33.333 ms.

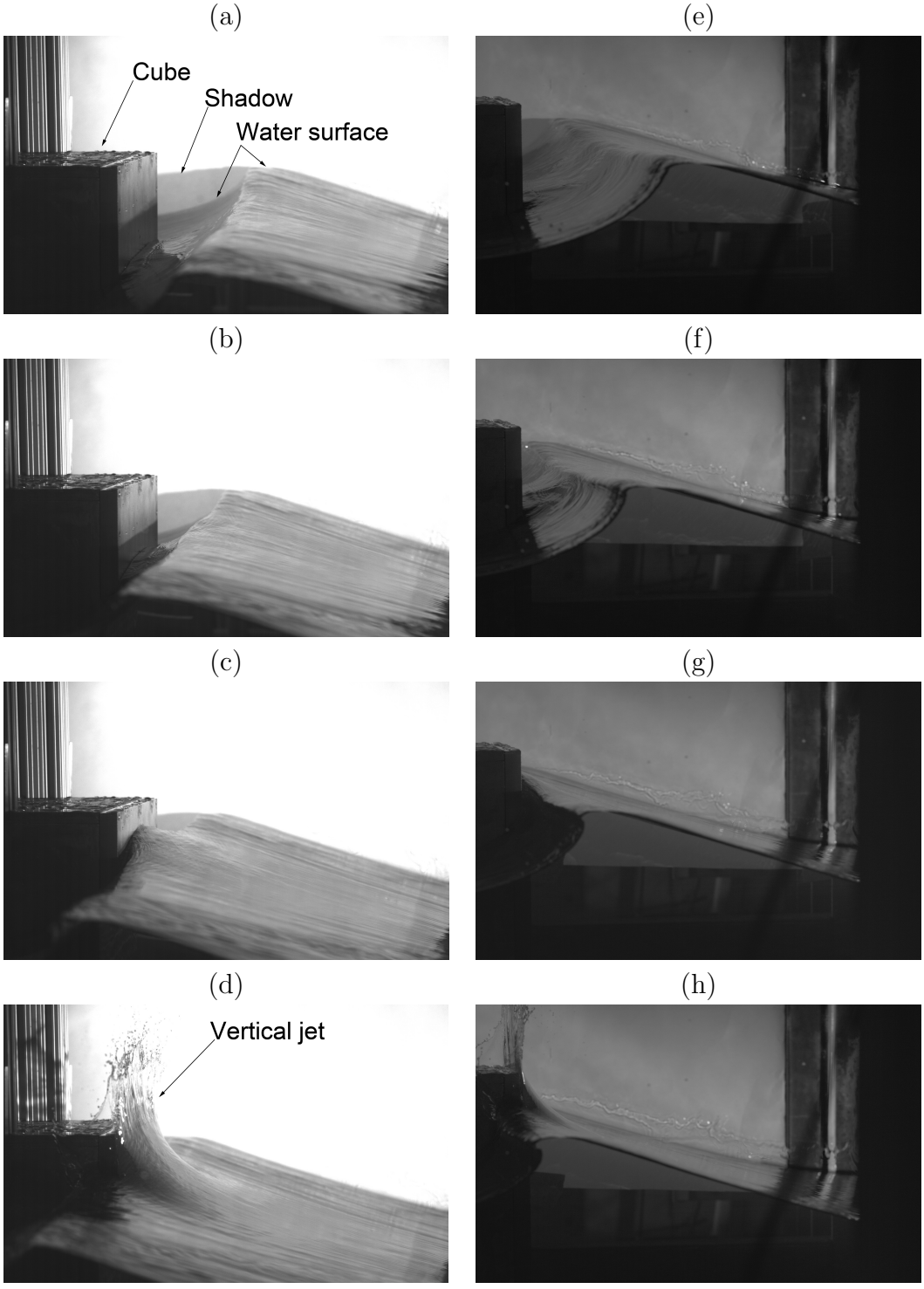

Figure 4.9: A sequence of eight images from two high speed movies of the impact of a breaking wave on the cube at Position 3. The left-hand side shows images taken with camera 2, while the right-hand side shows images taken with camera 1. Each row contains images from the same instant in time. The time interval between the photographs in 33.333 ms.

The profile shapes (from the LIF measurements) for one representative run for cube Position 1, are shown in Fig. 4.10 (a) up to the moment of wave impact (the instant when the water surface at the face of the cube has zero curvature) and the subsequent profiles showing the vertical jet are shown in Fig. 4.10 (b). The blue lines show the free surface with the magenta areas showing locations where spline fitting was used. Figs. 4.11 and 4.12 show the LIF measurements for one representative run for cube Positions 2 and 3, respectively.

To examine the repeatability of the surface profile histories for each cube position, the wave impact test was repeated 3 to 4 times at each location. Profile histories for the repeated runs up to the time of formation of the vertical jet are shown in Fig. 4.13 for Position 1, Fig. 4.14 for Position 2, and Fig. 4.15 for Position 3. As can be seen in these figures, the profiles are in close agreement, except at the forward face of the crest where the small amount of breaking before impact is seen to vary a bit from run to run. This effect was likely due to residual water motions in the wave tank. This residual motion can be reduced by increasing the calming period in between experimental runs.

4.4.2 Flip-Through Behavior

For the three cube positions analyzed here, the measured wave surface profiles were very similar (see Figs. 4.13, 4.14, and 4.15, corresponding to cube Position 1 (x_{cube} = 642 cm, z_{cube} = 0 cm), Position 2 (x_{cube} = 642 cm, z_{cube} = 5.7 cm) and Position 3 (x_{cube} = 647 cm, z_{cube} = 0 cm), respectively). Fig. 4.16 shows the first run of each of the three positions plotted in the same figure with

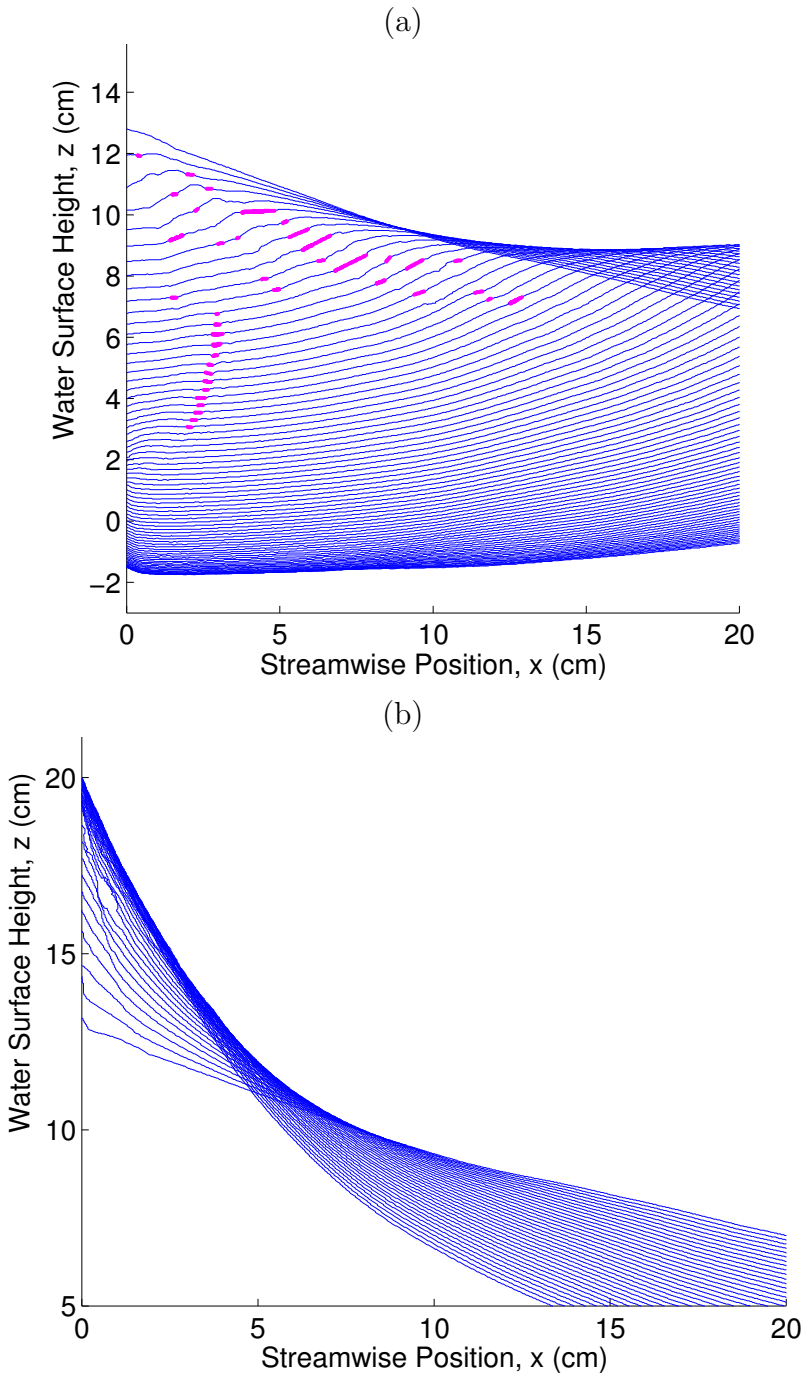

Figure 4.10: Sequence of profiles of the water surface during impact of the wave for Position 1, run 1. The time between profiles is 3.333 ms. For clarity, the earlier profiles, up to the point of formation of the vertical jet, are shown in (a) and the later profiles, after the point of formation of the vertical jet, are shown in (b). The small magenta areas on each curve are locations where spline-fitting was used.

(a)

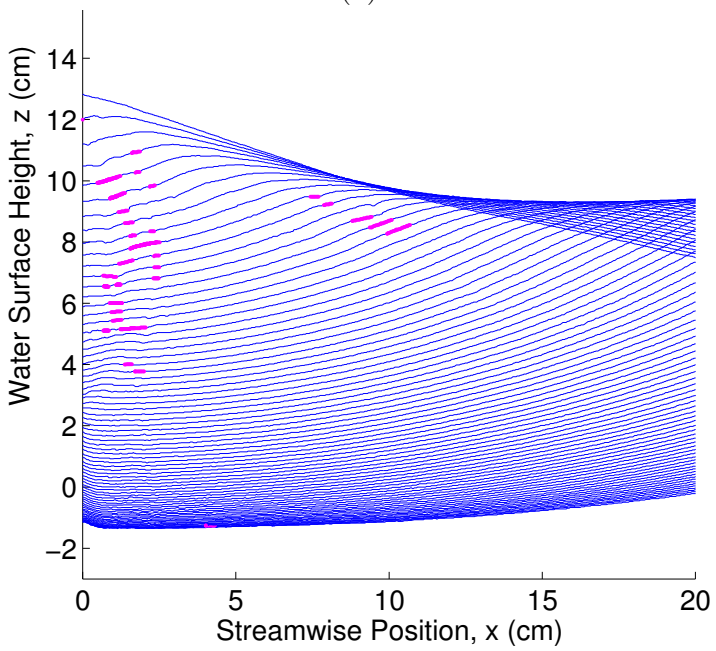

(b)

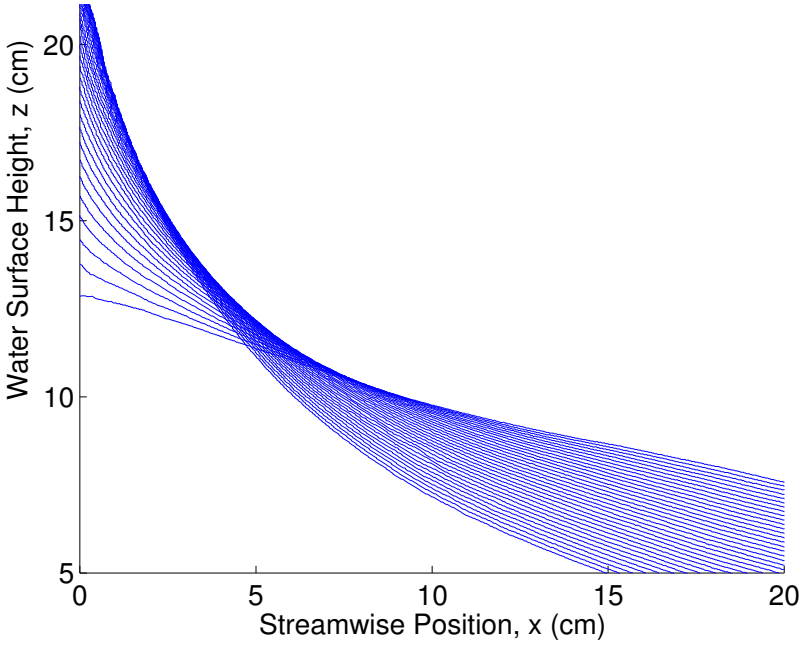

Figure 4.11: Sequence of profiles of the water surface during impact of the wave for Position 2, run 2. The time between profiles is 3.333 ms. For clarity, the earlier profiles, up to the point of formation of the vertical jet, are shown in (a) and the later profiles, after the point of formation of the vertical jet, are shown in (b). The small magenta areas on each curve are locations where spline-fitting was used.

(a)

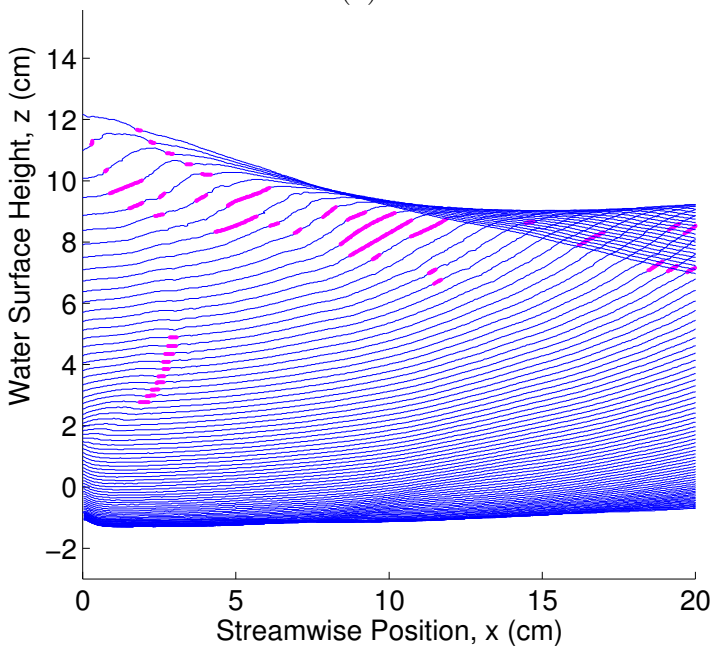

(b)

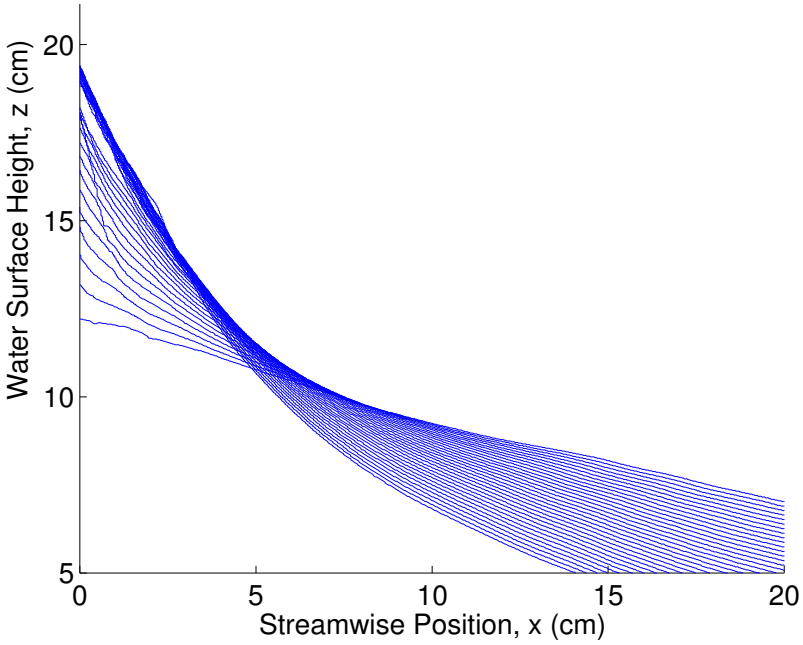

Figure 4.12: Sequence of profiles of the water surface during impact of the wave for Position 4, run 1. The time between profiles is 3.333 ms. For clarity, the earlier profiles, up to the point of formation of the vertical jet, are shown in (a) and the later profiles, after the point of formation of the vertical jet, are shown in (b). The small magenta areas on each curve are locations where spline-fitting was used.

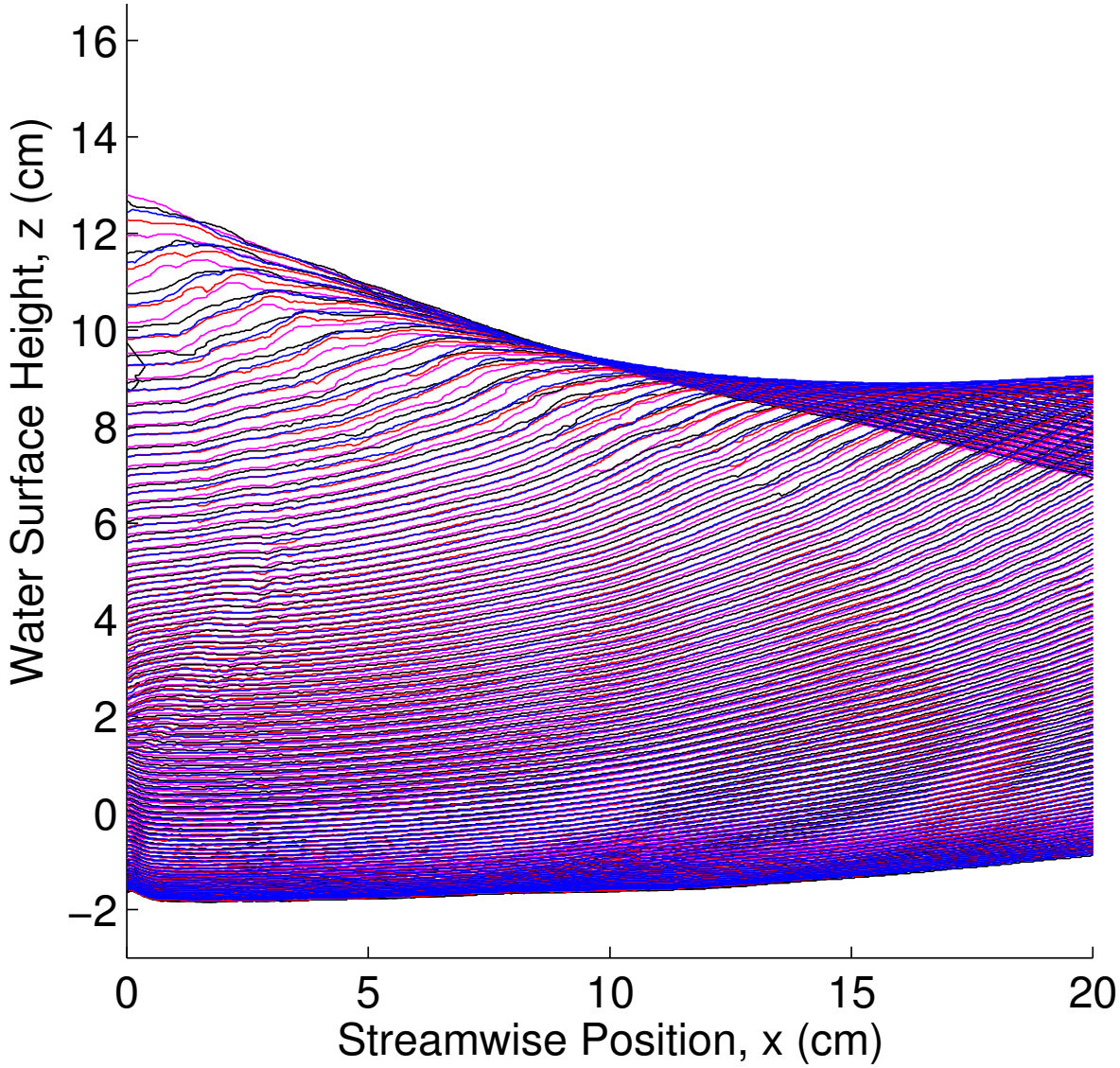

Figure 4.13: Sequence of profiles of the water surface during impact of the wave up to the point of formation of the vertical jet for Position 1 showing all four experimental runs. The time between profiles is 3.333 ms.

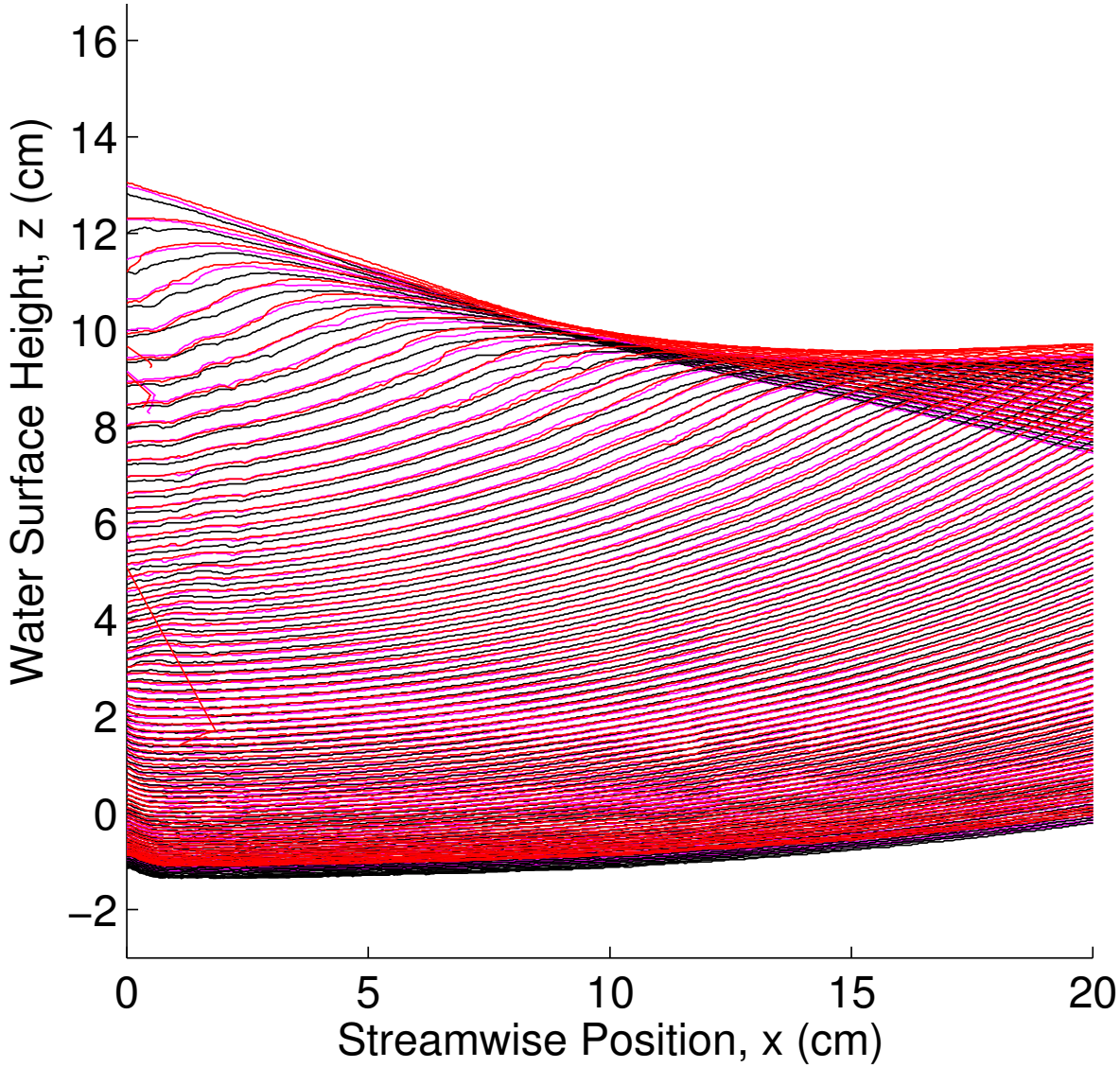

Figure 4.14: Sequence of profiles of the water surface during impact of the wave up to the point of formation of the vertical jet for Position 2 showing all three experimental runs. The time between profiles is 3.333 ms.

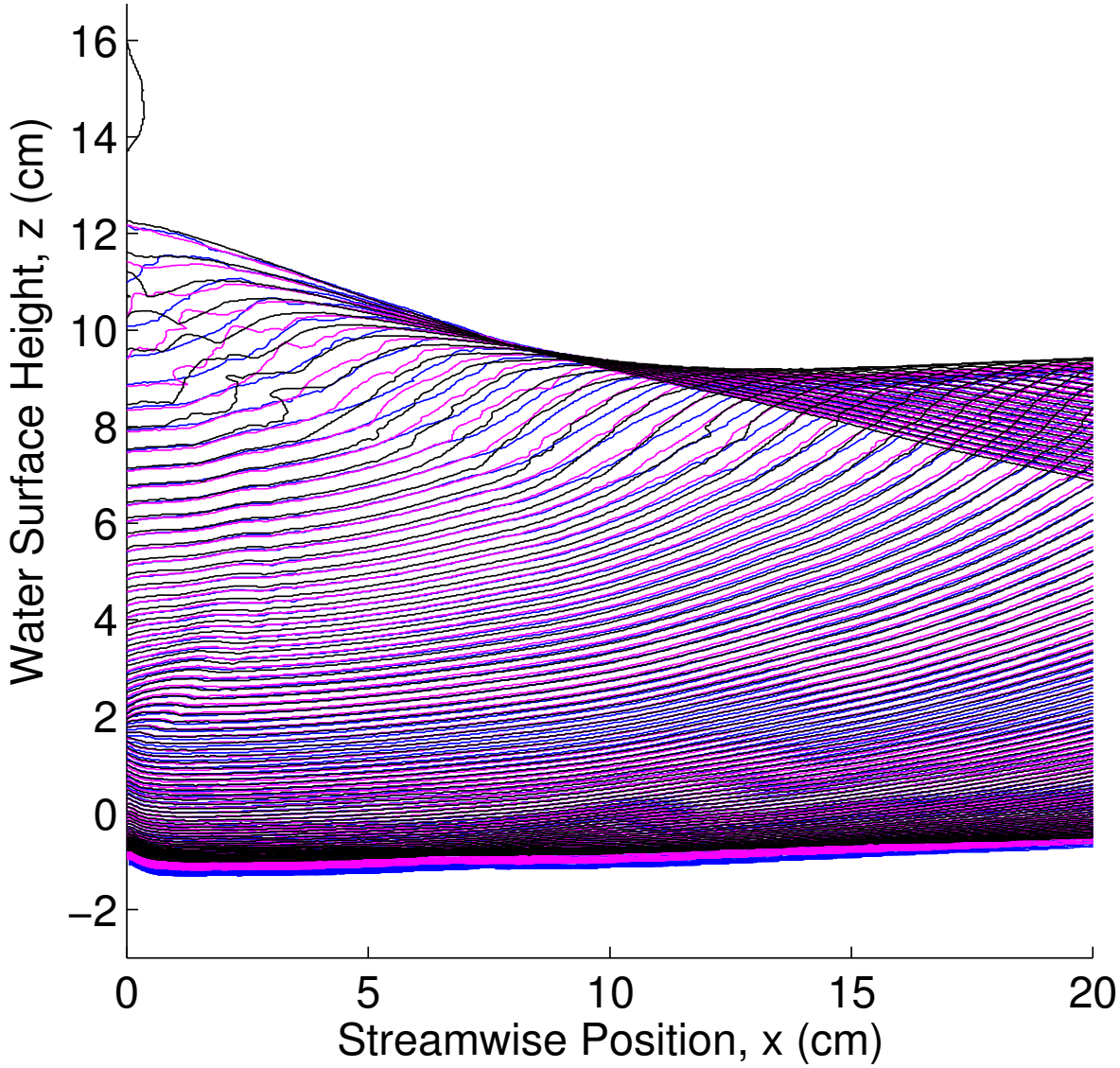

Figure 4.15: Sequence of profiles of the water surface during impact of the wave up to the point of formation of the vertical jet for Position 3 showing all three experimental runs. The time between profiles is 3.333 ms.

no post-shifting of the profiles in time or space. The wave surface profile evolution is quite similar for the three cases, even though the position of the cube varies by 5 cm between positions or 4% of the nominal breaker wavelength as given by linear theory, $\lambda = g/(2\pi f^2) = 118$ cm. This indicates that the flip-through behavior is relatively insensitive to the cube position.

It can be observed in the movies and surface profile histories that the water surface between the cube wall and the wave crest appears to be converging to a point. Furthermore, this water surface seems to have the shape of a circular arc whose radius is progressively decreased as the crest approaches the cube. To test this idea, circles were fit to the water surface between the cube wall and the wave crest. The circles were constrained to have their centers on the vertical line formed by the front face of the cube and the radius and vertical position of the center of the circle were obtained by a least squares fit to the profile data. Fig. 4.17 (a) shows the measured surface profiles (blue) for cube Position 1 (from Fig. 4.10) with these fits of the circular arc (shown in red). As can be seen in the figure, the circular arcs fit the profile data quite well up to the last three profiles where some wave breaking effects roughen the surface. Fig. 4.17 (b) shows a zoomed out version of Fig. 4.17 (a) to show that the red curves form large circles. As the wave approaches the cube, the radius of the circles decrease, and the center point of the circle moves down. Figs. 4.18 and 4.19 show the measured surface profiles (blue) for Positions 2 (from Fig. 4.11) and 3 (from Fig. 4.12), respectively, with circular fits to the front of the wave (shown in red). In Figs. 4.13, 4.14, 4.15, it was shown that that the wave profiles are repeatable, so profiles from only one representative run per cube

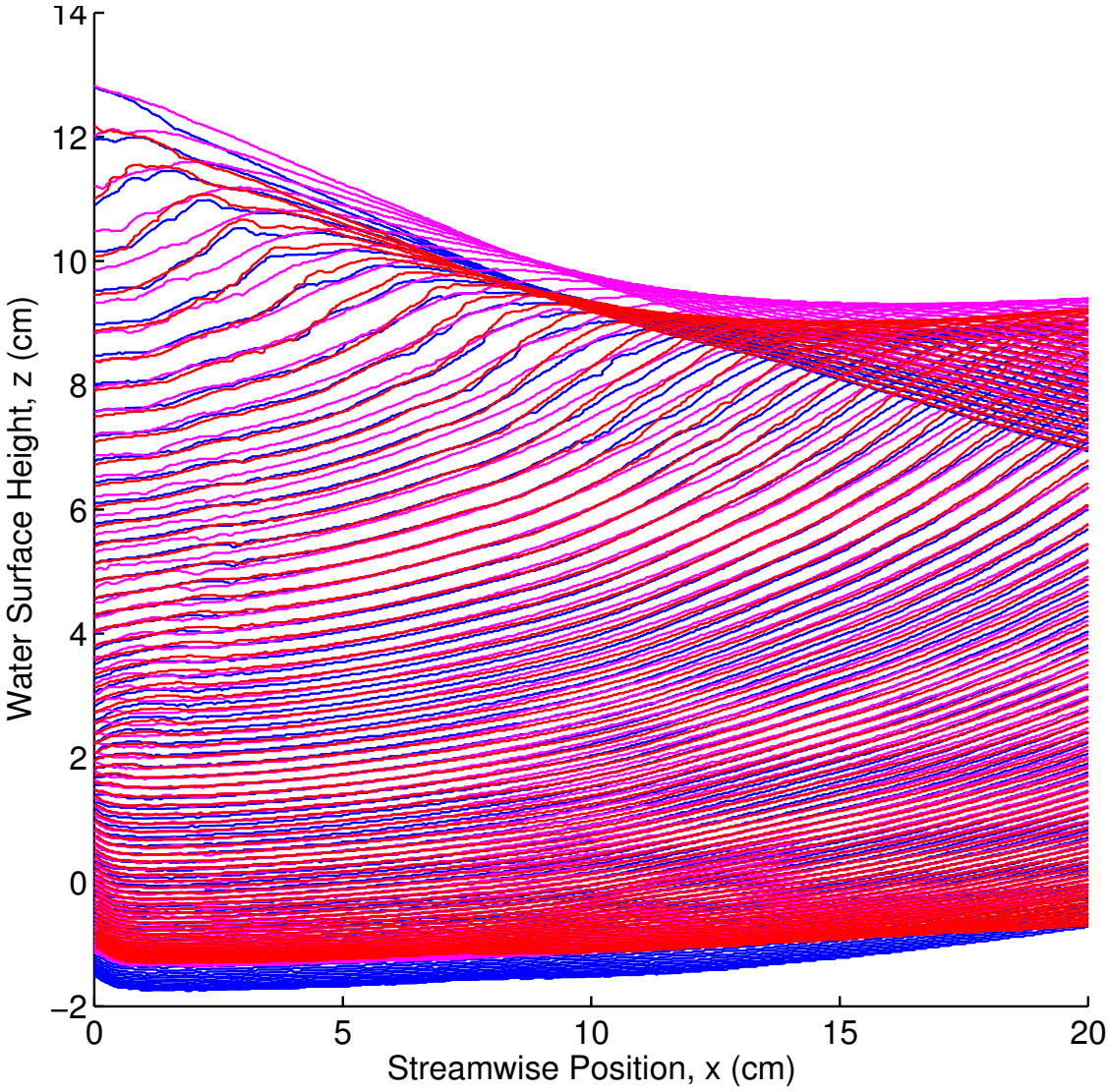

Figure 4.16: Sequence of water surface profiles for three representative runs for the three cube positions in Region I. Blue: Cube Position 1 (x_{cube} = 642 cm, z_{cube} = 0 cm), Magenta: Cube Position 2 (x_{cube} = 642 cm, z_{cube} = 5.7 cm) and Red: Cube Position 3 (x_{cube} = 647 cm, z_{cube} = 0 cm). Even though the positions of the cube vary by about 5 cm in the streamwise and vertical directions, the measured wave profiles do not differ substantially.

position was used to fit these circles.

In order to compare the results of the circular fits corresponding to the different cube positions, temporal histories of the radii and vertical heights of the centers of the circles are plotted in Figs. 4.20(a) and (b), respectively, for cube positions 1, 2 and 3. In these plots, $t = 0$ is taken as the time when the measured water surface profile in front of the cube face is projected to have zero curvature, as mentioned above this time is called the moment of wave impact. As can be seen in the Fig. 4.20 (a), the radius versus time histories are very close to one another and this similitude is more pronounced near $t = 0$. The data for Positions 1 and 2, in which the cube is at the same horizontal location, but different vertical locations are very similar quantitatively for all times. The radius versus time data, Fig. 4.20 (a), show that in all cases the radii decreases steadily from about 150 cm at $t = -0.25$ s to zero at $t = 0$. The curves of the height of the center of the circle versus time in Fig. 4.20 (b) also decrease steadily from about 150 cm above the mean water level at $t = -0.25$ s, but the height at $t = 0$ is nearly 13 cm for all three cases.

Within this range of cube positions, the wall strongly influences the shape evolution of the wave. At time $t = -0.15$ s, the radius of the circle for cube Position 3 appears to match the radius of the circles for cube Positions 1 and 2. To estimate the distance at which the wave profiles become similar for these cube positions, the time, $t = -0.15$ s corresponds to a position in space if the average phase speed of the wave, $v_p = 136$ m/s is assumed to be constant. This distance can be estimated at 20.4 cm ahead of the cube. The behavior of radius versus time for cube Positions 1 and 2 is similar, which is not surprising since the cube location

a

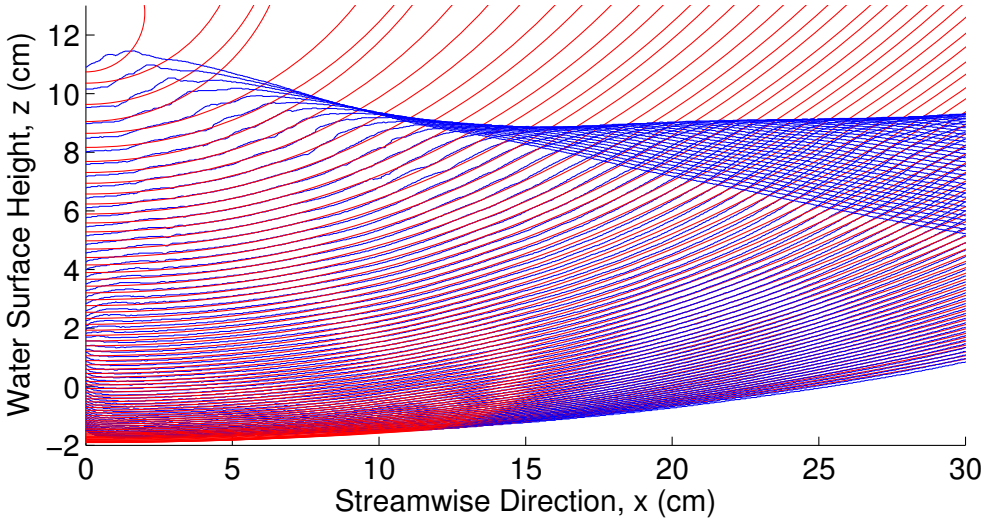

b

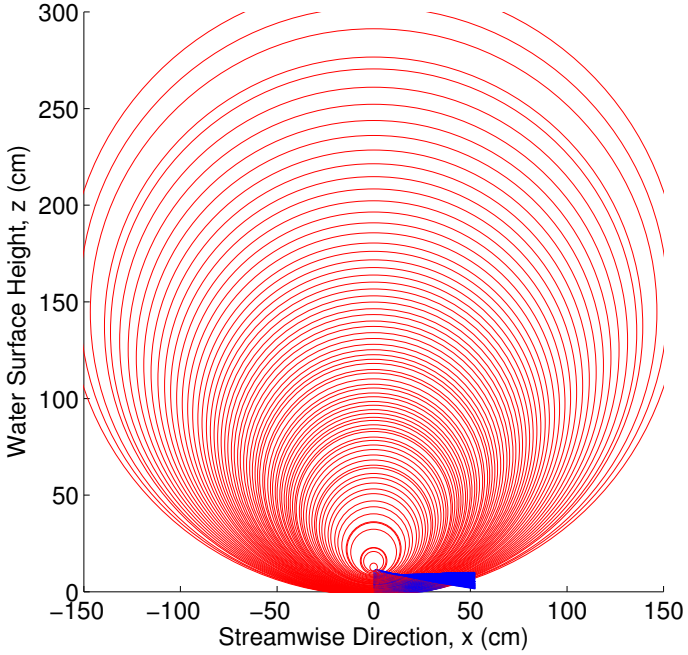

Figure 4.17: Measured surface profiles (blue) for cube Position 1 from Fig. 4.10 (a). The red curves show the circular fits to the area of the water surface between the front face of the cube and the wave crest. (a) shows the axes set to fit the blue measured profiles, showing only part of the circles, (b) shows the same plot zoomed out so that the entire circles are visible. The circles decrease in radius as the wave approaches the cube. The center point of the circle fit, which was set to be a point at $x = 0$ (along the vertical wall), moves downward as the wave approaches the cube.

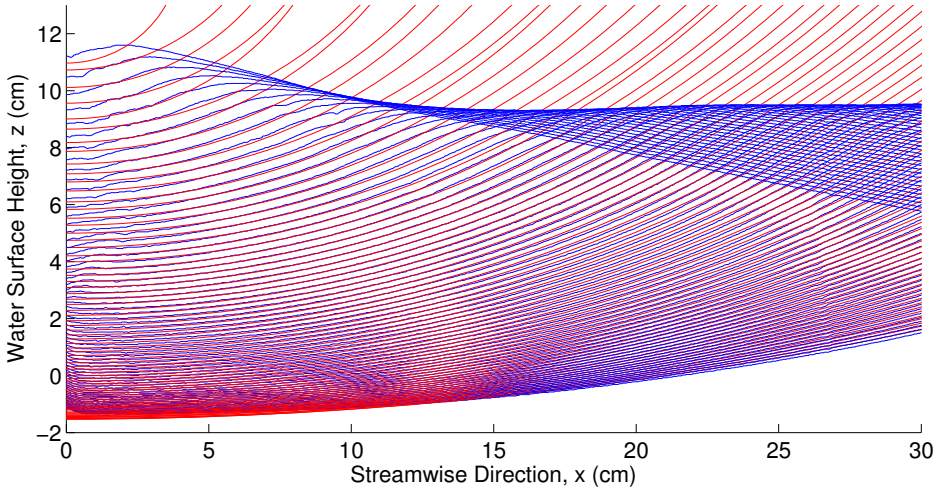

Figure 4.18: Measured surface profiles (blue) for Position 2 from Fig. 4.11 (a). The red curves show the circular fits to the area of the surface between the cube wall and the crest.

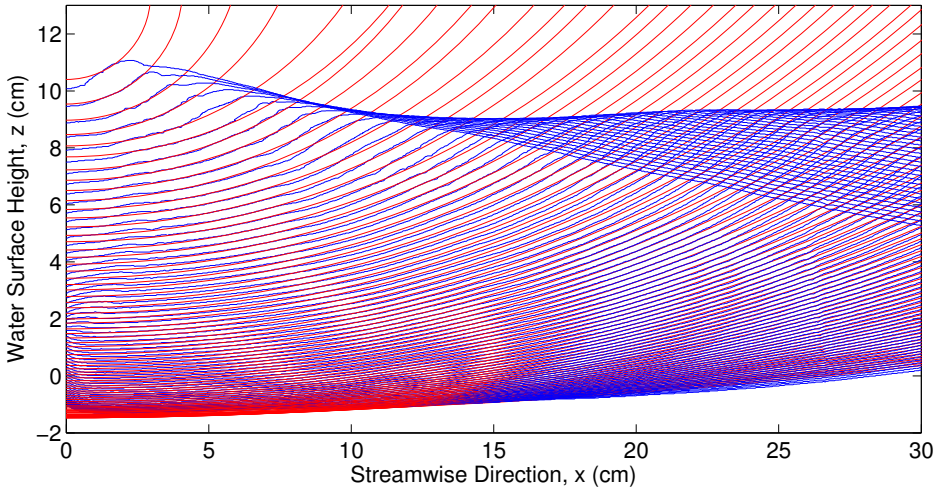

Figure 4.19: Measured surface profiles (blue) for Position 3 from Fig. 4.12 (a). The red curves show the circular fits to the area of the surface between the cube wall and the crest.

is in the same streamwise location relative to the breaking point of the wave. The depth of submergence at these small distances does not appear to affect the rate at which the quarter circle, formed by the wall and wave crest, shrinks over time. Fig. 4.20 (b) shows the vertical position of the circle center versus time for Positions 1, 2, and 3, which behaves similarly to the radius.

4.4.3 Region II: Position 4

A sequence of eight images from two white-light movies of the impact at cube Position 4 is shown in Fig. 4.21. Fig. 4.21 (a) - (d) show the view from camera 1, and Fig. 4.21 (e) - (h) show the view from camera 2, where each row corresponds to the same instant in time. The interval between frames is 33.33 ms, and the images were chosen such that the time instances at (c) and (g) correspond to the moment of wave impact as defined above. As the wave progresses toward the cube face, the crest steepens and begins to curl over (see Fig. 4.21 (g) and (h)). The wave impacts the front face of the cube as the crest overturns but before it plunges back into the water. Therefore, this cube position falls into the transition region, Region II.

The LIF movies for this case were processed and one representative sequence of water surface profiles from the contact point on the front face of the cube to a region upstream of the wave crest is shown in Fig. 4.22 (a) and (b). The wave profile shapes up to the moment when the vertical jet is formed are given in Fig. 4.22 (a) and the subsequent profiles showing the resulting water jet are given in Fig. 4.22 (b). These movies were harder to process due to the formation of the plunging jet just before the wave impacted the cube.

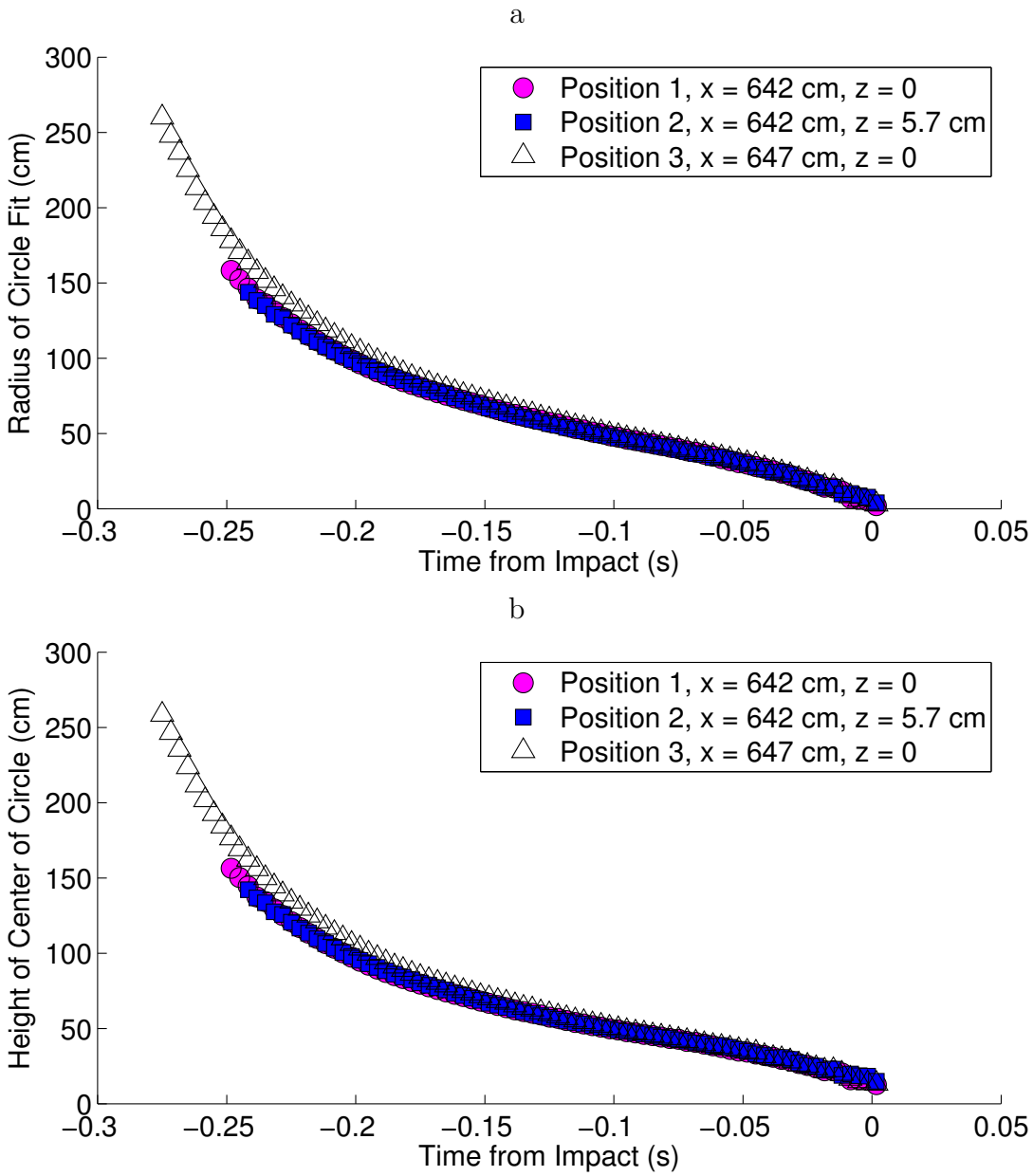

Figure 4.20: A comparison of the circular fit characteristics for one representative run for Positions 1, 2, and 3 in Region 1. (a) shows the radius versus time and (b) shows the vertical position of the circle center versus time. The time of impact was $t = 0$.

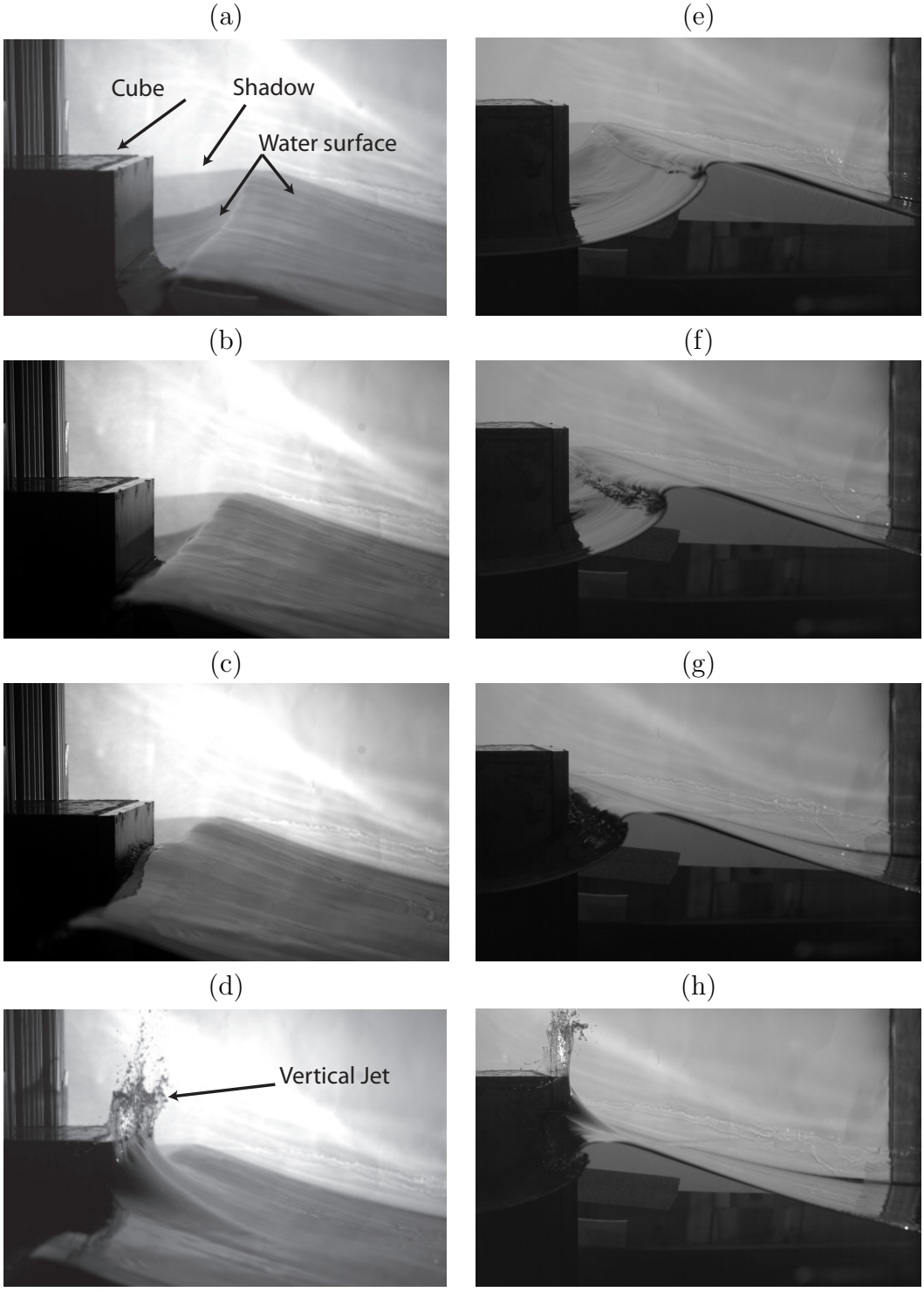

Figure 4.21: A sequence of eight images from two high speed movies of the impact of a breaking wave on the cube at Position 4. The left-hand side shows images from camera 2, while the right-hand side shows images taken from camera 1. Each row contains images from the same instant in time. The time interval between the photographs in 33.333 ms.

(a)

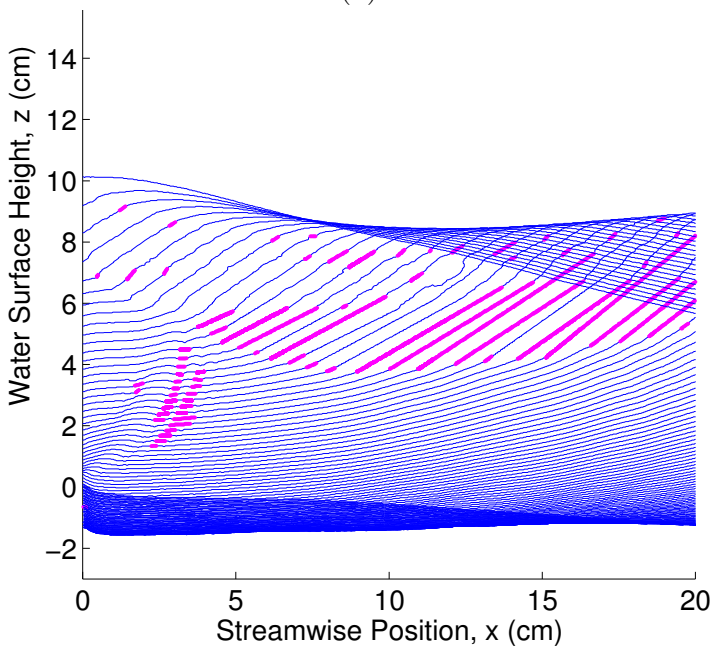

(b)

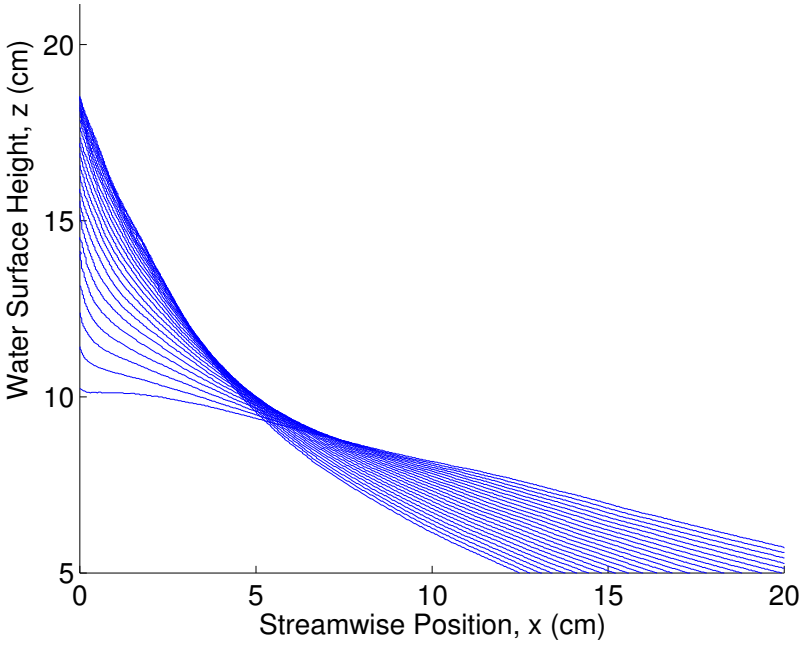

Figure 4.22: Sequence of profiles of the water surface during impact of the wave for Position 4, run 1. The time between profiles is 3.333 ms. For clarity, the earlier profiles, up to the point of formation of the vertical jet, are shown in (a) and the later profiles, after the point of formation of the vertical jet, are shown in (b). The small magenta areas on each curve are locations where spline-fitting was used.

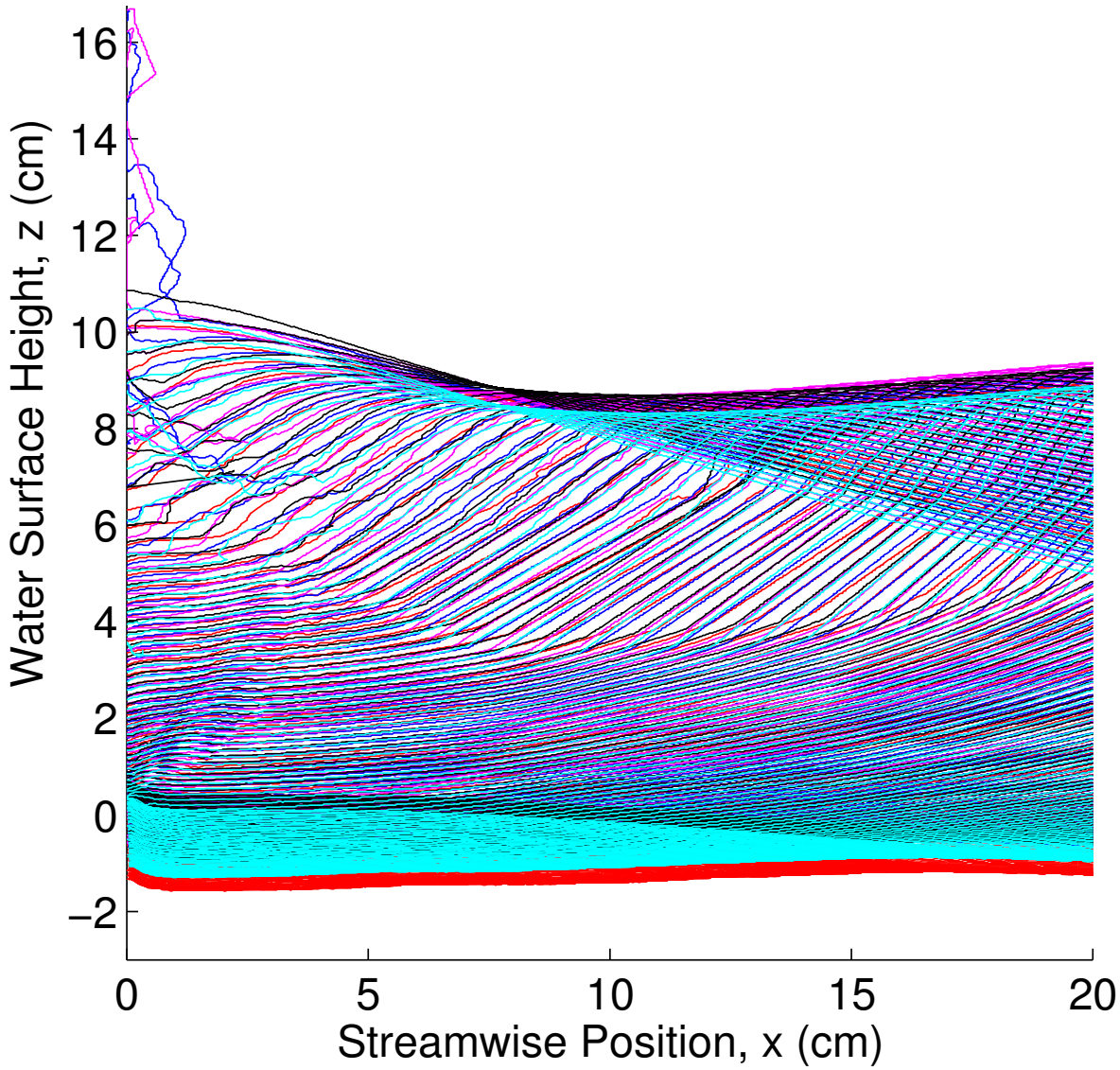

Figure 4.23: Sequence of profiles of the water surface during impact of the wave up to the point of formation of the vertical jet for cube Position 4. The time between profiles is 3.333 ms. Profiles are shown for all five experimental runs.

Water surface profiles up to the moment of impact for the other repeated runs were also obtained and Fig. 4.23 shows the five repeated runs for cube Position 4 plotted on the same figure. As can be seen from the figure, the profiles vary considerably from run to run, once the wave begins to break.

4.4.4 Contact Point

The height (z_c), vertical velocity (v_c), and acceleration (a_c) of the contact point of the water free surface on the front face of the cube are plotted versus time in Fig. 4.24, Fig. 4.25, and Fig. 4.26, respectively. The contact point height in each image was taken from the water surface profiles at the horizontal location corresponding to the front face of the cube. A 5-Point Central Difference Scheme was used to numerically compute the velocity, and a Second-Order Central Difference Scheme was used to compute the acceleration. The second derivative was very noisy due to the amplification of small changes from one point to another. The run-to-run variability is low for cube positions 1, 2 and 3, but is higher for position 4 due to the breaking that occurs before impact.

The water surface height rises continuously during the impact process, as shown for all four cube positions. The velocity of the contact point rises slowly at first but after reaching about v_p (the nominal wave phase speed as determined by linear theory, $v_p = g/(2\pi f)$) it rises nearly linearly to about $3v_p$ in about 0.02 s, yielding an average vertical acceleration on the order of 135 m/s^2, about $14g$.

Fig. 4.27 shows a comparison of the contact point height (z_c) and vertical velocity (v_c) versus time for each of the four cube positions. For each cube position,

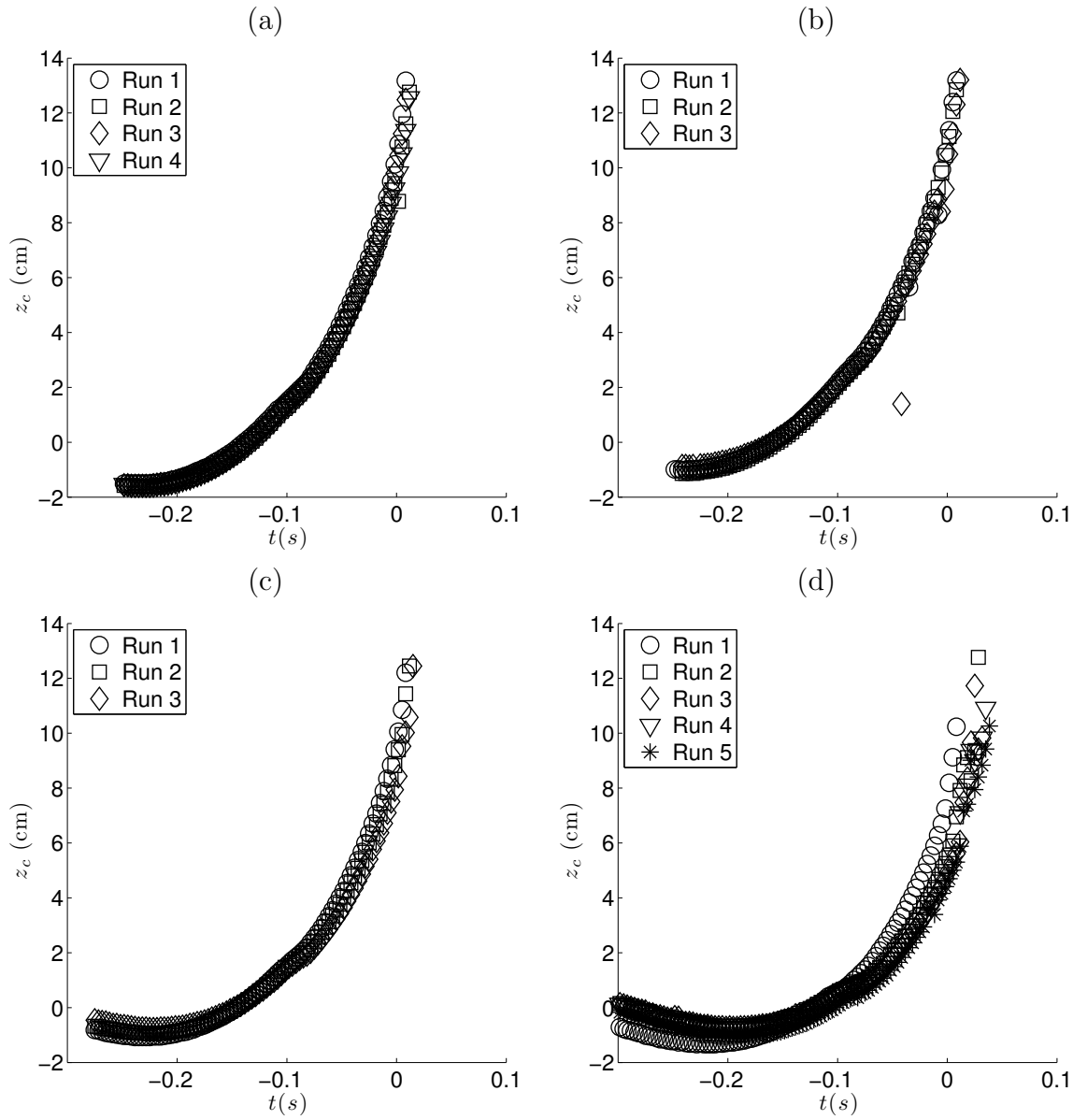

Figure 4.24: Contact point behavior. Contact point height, z_c, versus time for (a) Cube Position 1: $x_{cube} = 642$ cm, $z_{cube} = 0$, (b) Cube Position 2: $x_{cube} = 642$ cm, $z_{cube} = 5.7$ cm, (c) Cube Position 3: $x_{cube} = 647$ cm, $z_{cube} = 0$, and (d) Cube Position 4: $x_{cube} = 657$ cm, $z_{cube} = 0$. Each position shows three to five repeated runs to demonstrate the repeatability of the contact point motion. Time $t = 0$ is the time of impact.

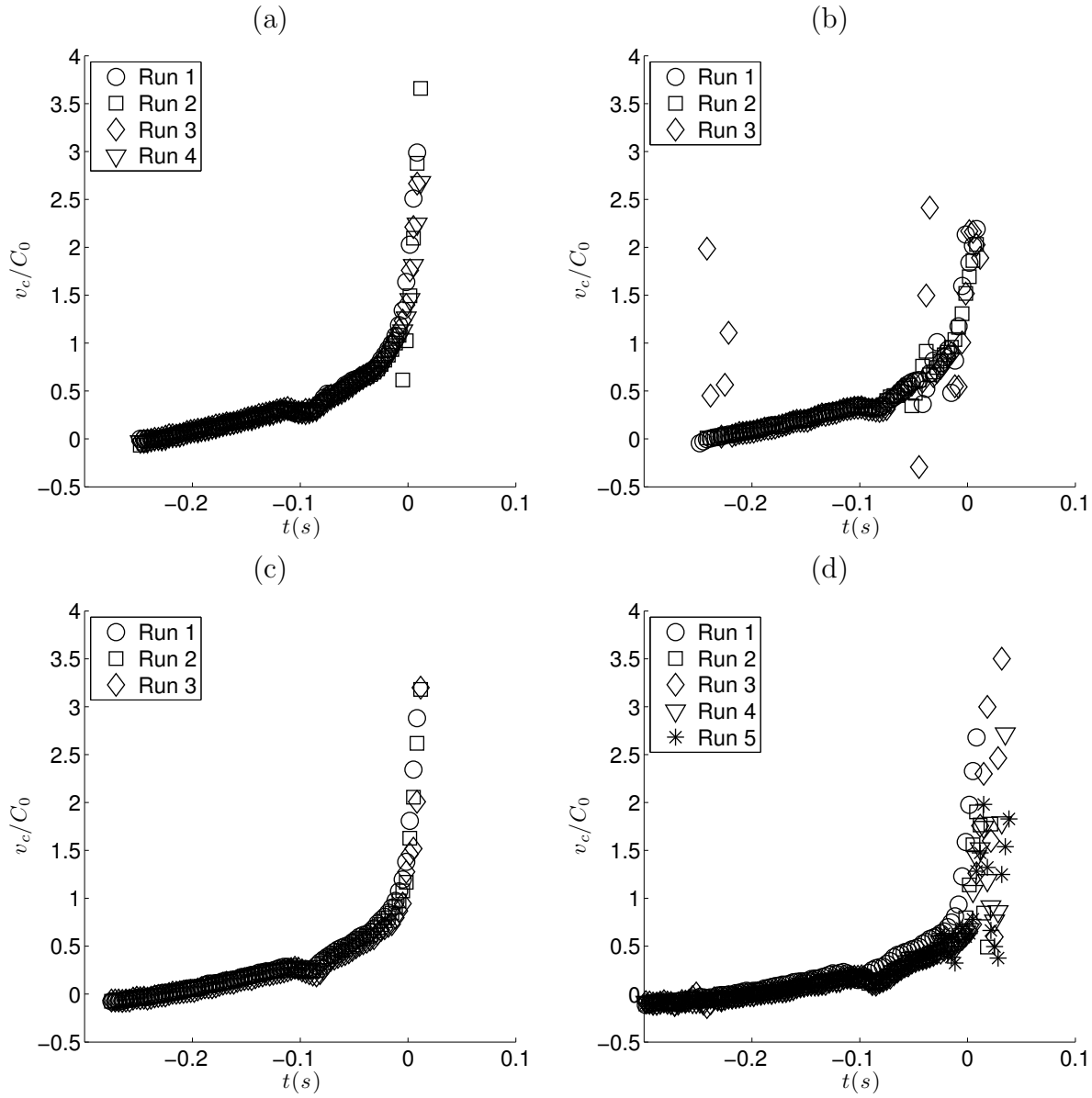

Figure 4.25: Contact point vertical velocity, v_c/v_p, versus time for (a) Cube Position 1, (b) Cube Position 2, (c) Cube Position 3, and (d) Cube Position 4, where v_p is the phase velocity of the wave ($v_p = 135.77$ cm/s). Each position shows three to five repeated runs. $t = 0$ is the moment of impact as defined in the text.

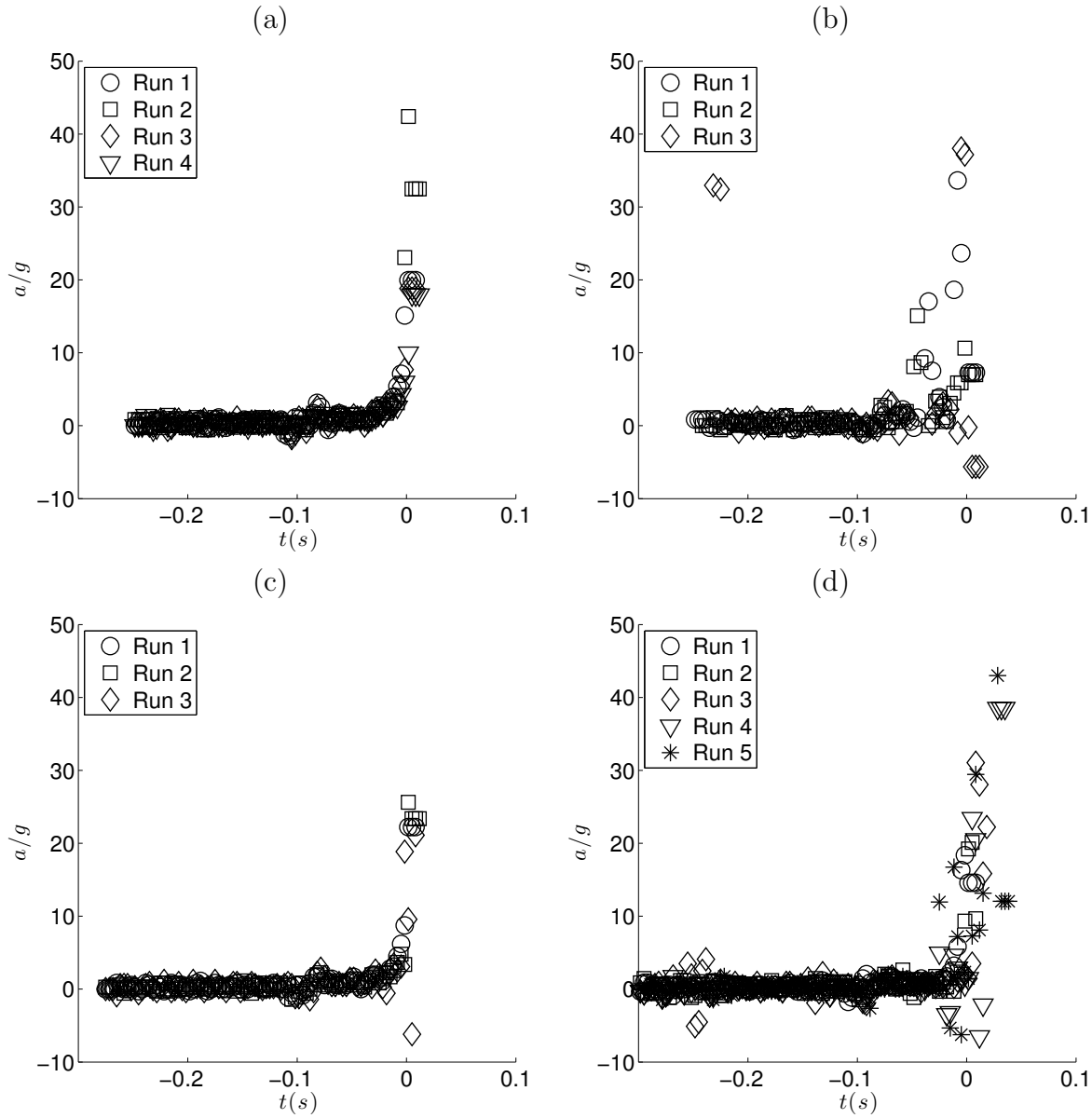

Figure 4.26: Contact point acceleration, a_c/g, versus time for (a) Cube Position 1, (b) Cube Position 2:, (c) Cube Position 3, and (d) Cube Position 4. Each position shows three to five repeated runs. $t = 0$ is the instant of wave impact.

(a)

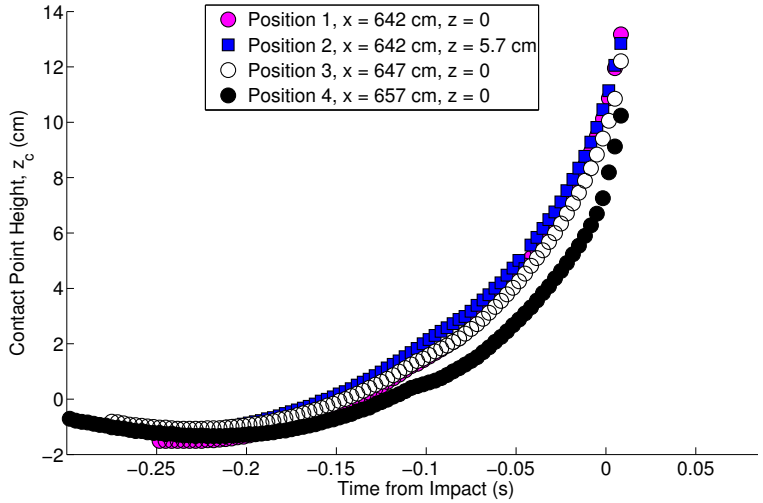

(b)

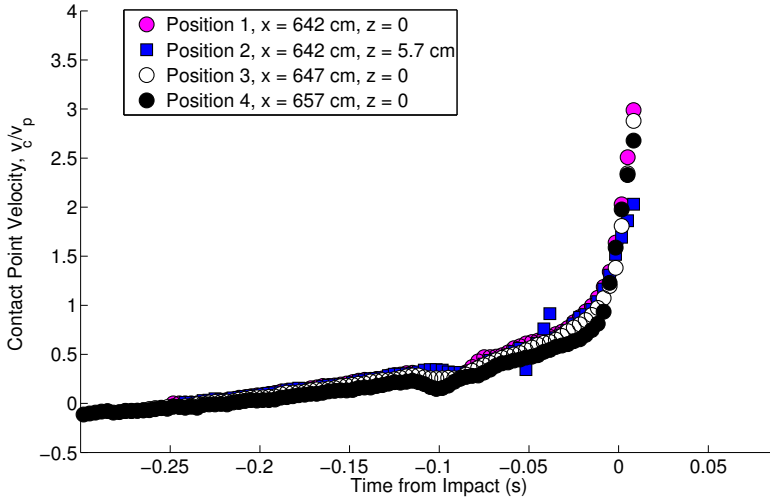

Figure 4.27: A comparison of the contact point height (z_c) and vertical velocity (v_c) for each of the four cube positions. For each cube position, one representative run is shown. (a) shows the contact point height, and (b) shows the vertical velocity. The time scale is shifted so that $t = 0$ is the moment of wave impact.

one representative run is shown. Fig. 4.27 (a) shows the contact point height, and Fig. 4.27 (b) shows the vertical velocity. The contact point height versus time is quite similar for Positions 1, 2 and 3. For Position 4, the contact point rises at a slower rate and to a lower height when compared to the other positions. This different behavior can be interpreted as a consequence of the overturning of the wave as it approaches the cube, which does not happen when the cube is placed at positions 1 to 3.

4.5 Conclusions and Future Work

An experimental study on the impact of plunging breaking waves on a partially submerged cube in deep water was conducted. The results of this chapter focus on the shape evolution of the free surface as a plunging breaking wave approaches the partially submerged cube. The shape evolution was measured using cinematic Laser-Induced Fluorescence (LIF). There were four different positions of the cube relative to the mean free surface and to the breaking point of the single wave used in this study. The positions of the cube are summarized in Sec. 4.4. Within the range of cube positions that were explored, the wave impact phenomenon can be categorized as belonging to Regions I (where the region of the water surface between the water contact point and the crest focuses to a point, without wave breaking, during impact) and II (where a plunging jets forms, overturns and impacts on the front face of the cube before impacting the front face of the wave) as described by Chan and Melville [16]. Comparing the surface evolution of the three cube positions that fell into Region I, it was found that the surface profiles close to the front face

of the cube were nearly identical. This suggests that within this range of cube positions, the surface evolution of an incoming wave is not very sensitive to the position of the cube.

In order to investigate this further and noting that the approaching wave appears to form a circular arc between the front face of the cube and the steepening crest, circular arcs were fit to the measured profile. These circular arcs had decreasing radii over time as the wave approached the cube. It was found that the radius behavior, for all cube positions corresponding to Region I impact was nearly the same.

The contact point position between the free surface and the front face of the cube was extracted from the surface profile measurements. As expected, the time evolution of the contact point obtained in the experimental runs corresponding to different cube positions in Region I, are very similar to one another. For the cube position corresponding to Region II, the contact point evolution did not compare well with that corresponding to cube position in Region I. This result is expected since the nature of the wave impact in Region II is different with the plunging jet overturning before impact with the cube. For all the cube positions studied here, a similar trend is observed in the time evolution of the contact point. Initially, the contact point moves upward at a relatively slow speed. When the wave crest becomes closer to the cube, a sudden increase in the contact point upward speed is observed. Accelerations reached about $14g$ close to the impact event. Ultimately, these high accelerations imply high pressures on the cube front face as a consequence of the impact. However, pressure measurements were not made at this point and

constitute future work.

The conclusions drawn in this dissertation focused mainly on the range of cube positions where flip-through occurred. Flip-through is the region where the highest pressure distributions on the front face of the cube are expected. Future work would include repeating experiments within this region while simultaneously measuring the pressure on the front face of the cube. Finally, the angle of attack of the cube relative to the mean water level is another parameter that can be explored. Preliminary results with the cube tilted toward the wave maker (not included in this dissertation) show promising features not observed in the cases presented here.

Chapter 5
Summary of Conclusions and Contributions

5.1 The Natural Implosion of Cylindrical Shell Structures in High-Pressure Water

From the literature reviewed in Sec. 2.2, it was found that few studies examined the implosion process of cylindrical shell structures. A systematic study that varied the geometry, material, and implosion mode number was conducted in this dissertation. The implosion events were recorded quantitatively with simultaneous high-speed movies and high-frequency pressure-field measurements.

For the cylindrical models that collapsed in mode 2, the pressure distribution and pressure impulse in the azimuthal direction did not correlate with the orientation of the final deformed shape. When comparing the pressure records, the collapse times and peak pressure magnitudes varied significantly from one model design to another. However, when the average of the eight meridian plane pressure sensors was scaled in time with the characteristic bubble collapse time ($R_i\sqrt{\rho/\left(P_c - P_0\right)}$, where R_i is the internal radius of the model, P_c is the natural collapse pressure, P_0 is the initial pressure of the air inside the model, and ρ is the density of water) and scaled in pressure by the relative pressure between the ambient collapse pressure and the initial gas pressure inside the structure ($P_c - P_0$), the pressure waves, are remarkably similar. The normalized collapse times are nearly identical, about 2.5 $\pm$ 0.25. The average normalized pressure peaks vary from 0.5 to 0.9 over the models tested. There is considerable range in the normalized pressure in repeated implosions of the same

model design, particularly in the case of the aluminum models, all of which have the largest diameter and the lowest mass ratio (defined as the mass length of the tube from which was constructed divided by the mass per length of the water displaced by the model). The success of this bubble scaling may indicate that during collapse, the contribution of the stiffness of the out-of-round metal structure is minimal compared to the hydrodynamic forces.

For the two experiments that explore the variation in mode number while holding the available energy (P_cV) constant, the scaling used for the pressure waves in the mode 2 experiments worked well for the time scale (horizontal axis) but not as well for the pressure magnitude scale (vertical axis). In view of the greater amount of deformation per unit length to form higher numbers of lobes, this result is not surprising.

5.2 Explosion-Induced Implosion of Cylindrical Shell Structures

In previous published work involving underwater explosions near structures, the studies focus on sufficiently strong structures that do not implode due to nearby explosions. In these studies, the vibration modes are calculated as well as localized damage. In the current work, the cylindrical structure used is pre-loaded with hydrostatic pressure to about 90% of its natural implosion pressure. Therefore, when the nearby explosion occurs, the cylindrical model becomes unstable and collapses.

In these experiments, the interaction of the model with the explosion shock-waves and oscillating gas bubble from the explosion caused the model to implode by three mechanisms. In the first set of experiments, the cylindrical model imploded

due to the impact of the model-directed re-entrant jet formed during the second bubble collapse of the explosion gases. In the second set of experiments, the stand-off distance between the explosive and cylindrical structure were chosen to be at greater distances than the predicted maximum bubble radius. The stand-off distances were varied while keeping the ambient pressure constant. It was found that at stand-off distances of up to $8.6R_{\text{bub}}$ the cylindrical model would implode due to the explosion event. In the final set of experiments, the collapse of models with different geometry and material was investigated under similar loading conditions. The high-speed movies show that the characteristic explosion events occur within 48 to 96 microseconds (one or two frames) from run-to-run. In these experiments, structure oscillations were observed before implosion. The oscillations are driven by the pulsating pressure field (due to the pulsating explosion bubble). The oscillation frequency was measured from the high-speed movies and was found to be about half the natural frequency for the whipping mode of the model and one third of the natural frequency of the breathing mode of the model as calculated through ANSYS with the model in an air environment.

In these experiments, the pressure at the location of the cylindrical model exceeded the natural collapse pressure for about 0.16 ms. During this time, the cylindrical model did not collapse even though the pressure was at least 4.5 times higher than the natural collapse pressure. The aluminum cylindrical models did not collapse until 4 ms after the high-pressure wave passed.

5.3 The Impact of a Plunging Breaker on a Partially Submerged Cube

Experiments and computational studies of the impact of breaking waves on walls are marine structures is critical to their design. Traditional theoretical studies of water waves do not offer much insight into the high pressures associated with the wave impact process. Therefore, a combination of careful experimental studies and validated computational models are needed to properly predict the pressure field of a wave impacting a wall. Previous impact work has concentrated on two-dimensional studies where the structure is a wall that extends to the bottom of the wave tank.

In the present work the interaction of a plunging breaking water wave with a rigid partially submerged cube ($L = 0.305$ m with water depth $H = 0.91$ m) was studied experimentally in a wave tank. One plunging wave was used for all experimental runs, and surface profile measurements were taken with the cube submerged by $0.5L$ at three horizontal positions ranging from $x_{\text{cube}} = x_b - 0.28$ m to $x_{\text{cube}} = x_b - 0.13$ m, where $x_b = 6.75$ m is the breaker location in the absence of the cube as measured from the back face of the wedge of the wave maker. Measurements were also taken with the cube submerged by $0.3L$ at one horizontal position, $x_{\text{cube}} = x_b - 0.28$ m. Within the range of positions that were explored, the wave impact behavior fell into two categories. In the first behavior category, also called flip-through, the free surface between the front face of the cube and the wave crest forms a circular arc that converges to a point and then forms a high-velocity vertical jet (speeds ≈ 3 m/s). In the second behavior category, the wave forms a plunging

jet that impacts the cube wall directly.

For the conditions where flip-through was observed, circular arcs were fit to the measured profile for the region between the front face of the cube and the crest. These circular arcs had decreasing radii over time as the wave approached the cube. It was found that the radius behavior, for all cube positions corresponding to this impact category, was nearly identical for times when the wave crest was near the cube (within 20 cm). This suggests that within this range of cube positions, the surface evolution is controlled by local dynamic processes. The work presented in this dissertation lays the groundwork for future experiments to be done with pressure measurements of the wave on the cube.

Appendix A
Natural Implosion Figures

Run	Mode n	Material	Outer Diameter D_o (mm)	Wall Thickness w (mm)	Length L (mm)	Collapse Pressure P_c (bar)	Available Energy P_cV (N-m)
B2D25r1	2	Brass	25.4	0.33	231	7.3	81.1
B2D25r2		260				7.1	78.9
B2D25r3						7.5	83.3
B2D16r1	2	Brass	16.6	0.36	152	26.6	80.1
B2D16r2		260				26.5	79.8
B2D16r3						26.9	81.1
A2A2r1	2	Alum	38.1	0.89	241	26.5	661.7
A2A2r2		2024				26.6	664.1
A2A2r3						28.2	704.0
A2A2r4						26.7	666.6
A2A2r5						26.4	659.1
A2A3r1	2	Alum	38.1	0.89	241	28.3	706.5
A2A3r2		3003				28.7	716.6
B3D25r1	3	Brass	25.4	0.33	84	19.4	78.2
B3D25r2		260				18.8	76.0
B3D25r3						20.7	83.6
B3D25r4						21.4	86.4
B3D25r5						21.3	86.1
B4D25r1	4	Brass	25.4	0.33	58	26.1	72.9
B4D25r2		260				28.3	78.9
B4D25r3						28.9	80.4
B4D25r4						27.9	77.9
B4D25r5						31.4	87.7
B4D25r6						31.5	88.0
B4D25r7						31.5	88.0

Table A.1: A summary of the cylindrical models imploded naturally for the first three experiment sets. The names given have an "A" for aluminum or "B" for brass. The mode number follows, then there is either a "D" for diameter followed by numbers representing the diameter, or for the case of aluminum, an "A" for alloy followed by "2" for 2024 or "3" for 3003. Finally, there is an "r" representing the run number for the given geometry and material.

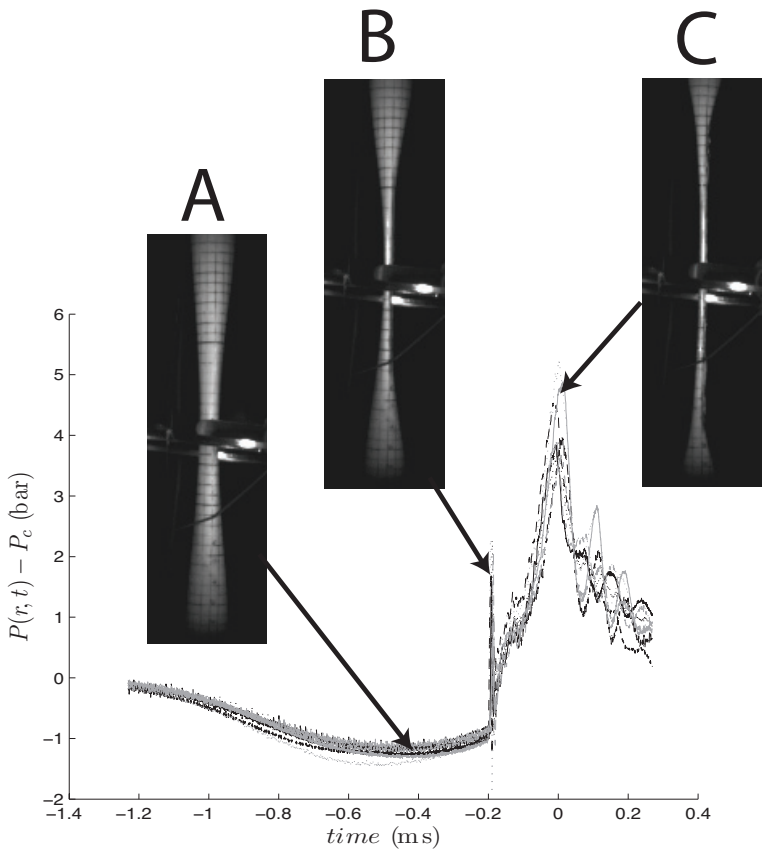

Figure A.1: Each line represents one of the eight meridian pressure sensors for B2D25r2. Three still frames from the high-speed video are shown at the times corresponding to the minimum pressure peak, first small positive peak and the maximum positive peak. As the walls close in, there is a drop in pressure (A). The first small positive peak occurs when the walls first impact each other (B). The large positive pressure peak occurs when the walls make full contact and the collapse is complete (C).

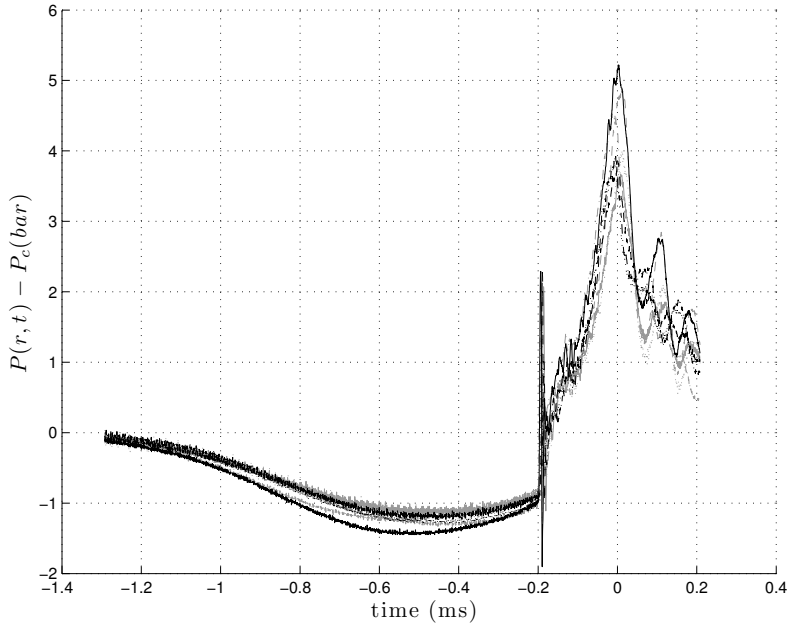

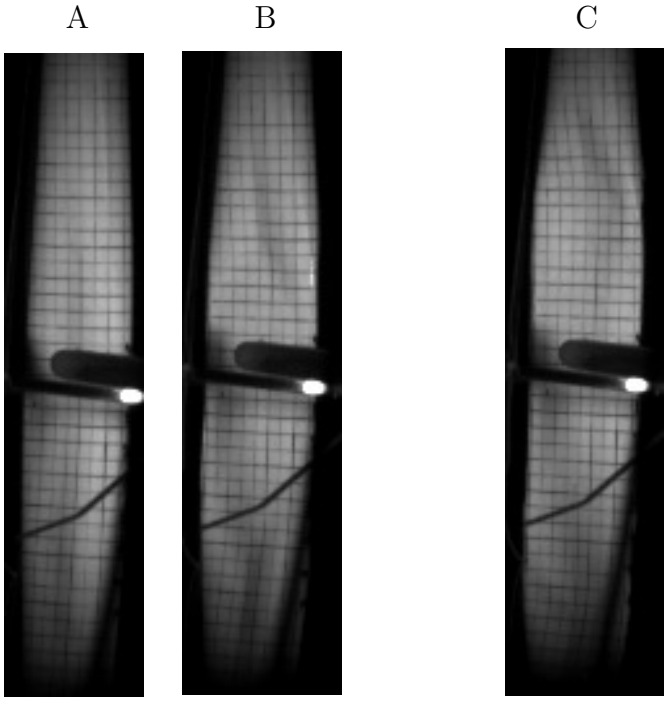

Figure A.2: B2D25r1

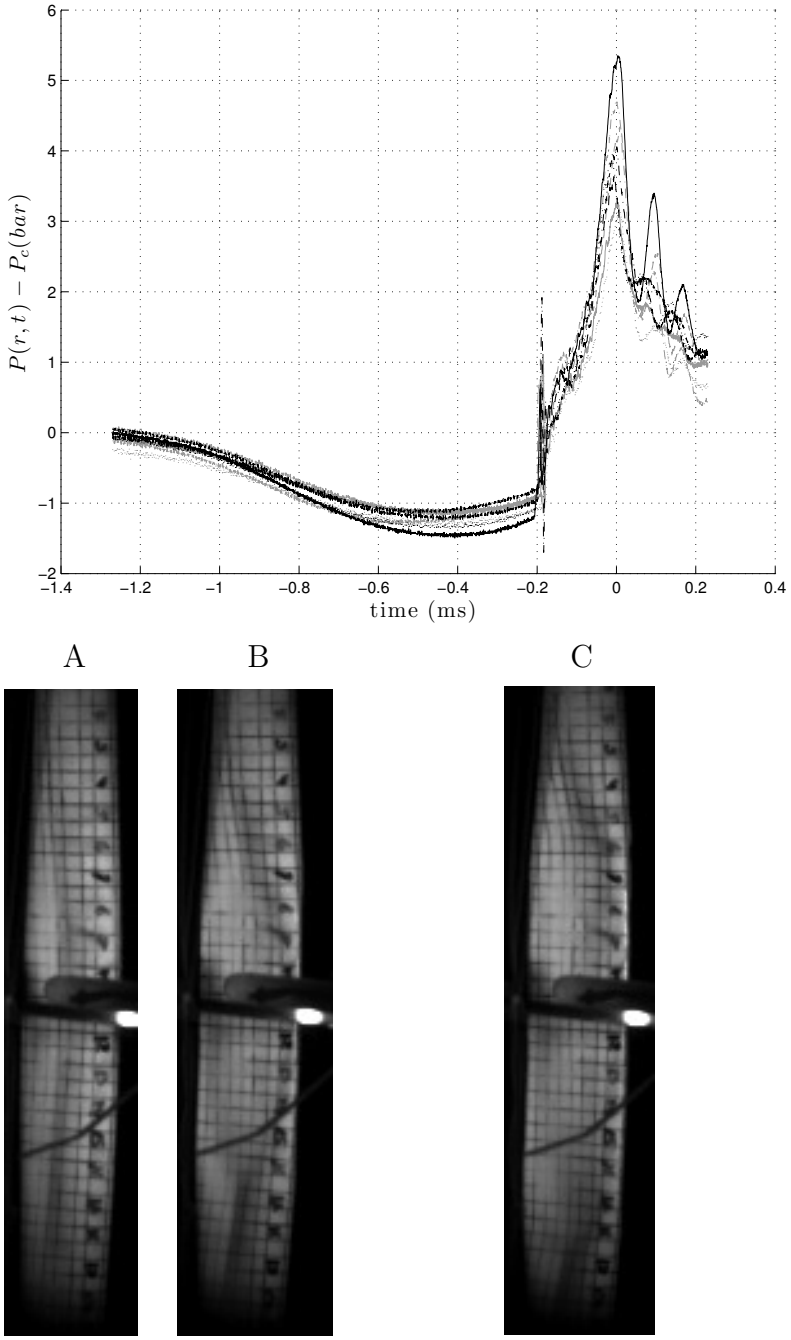

Figure A.3: B2D25r3

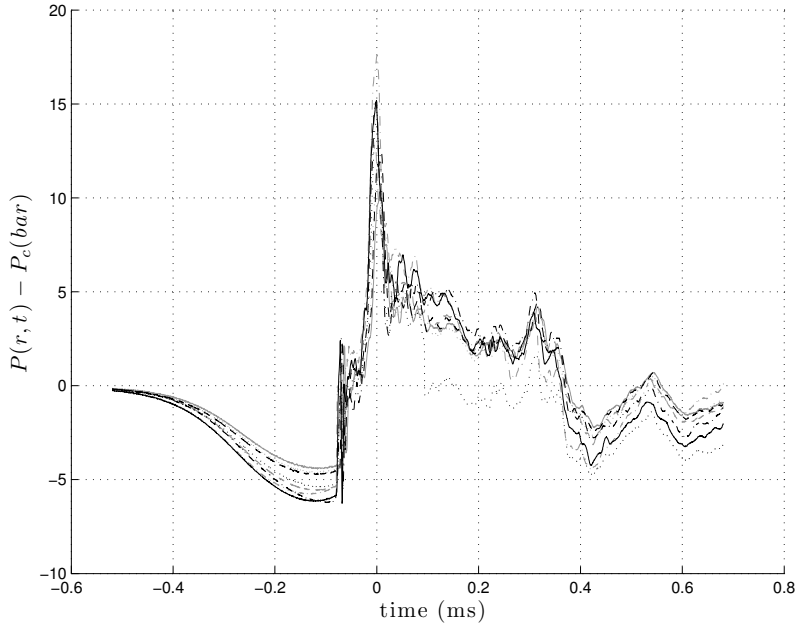

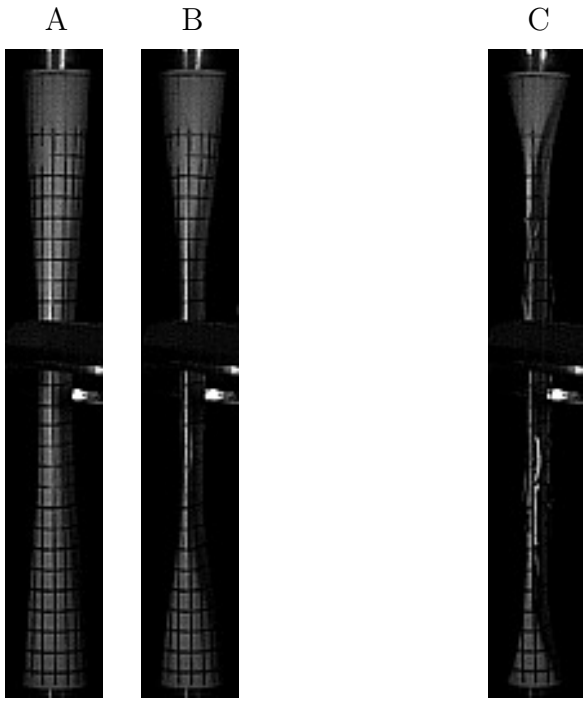

Figure A.4: B2D16r1

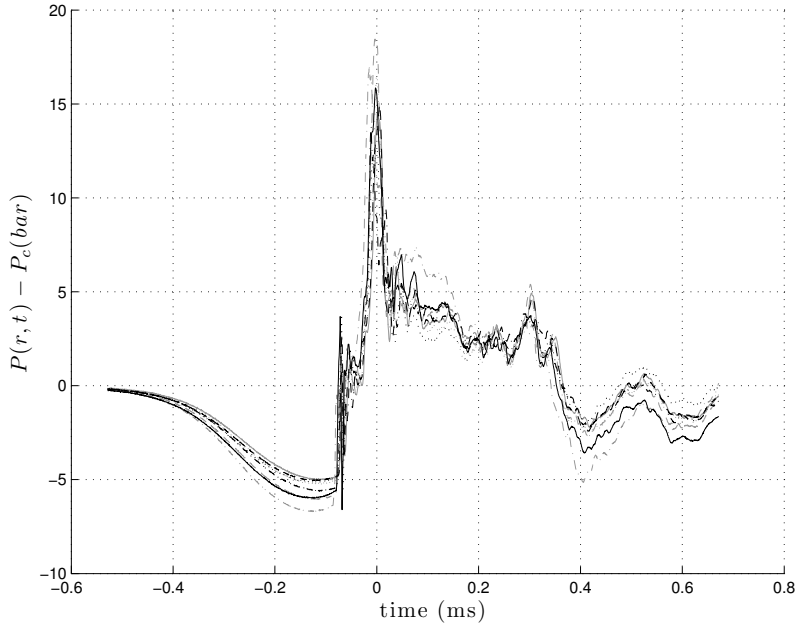

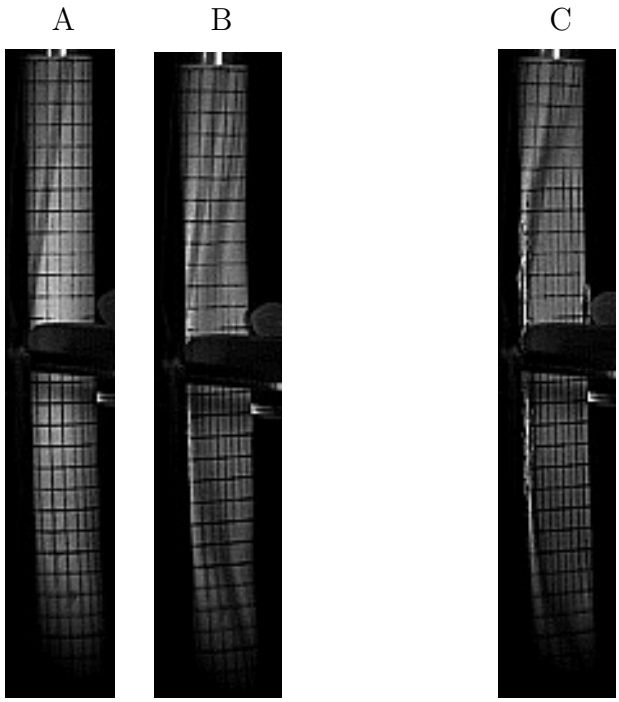

Figure A.5: B2D16r2

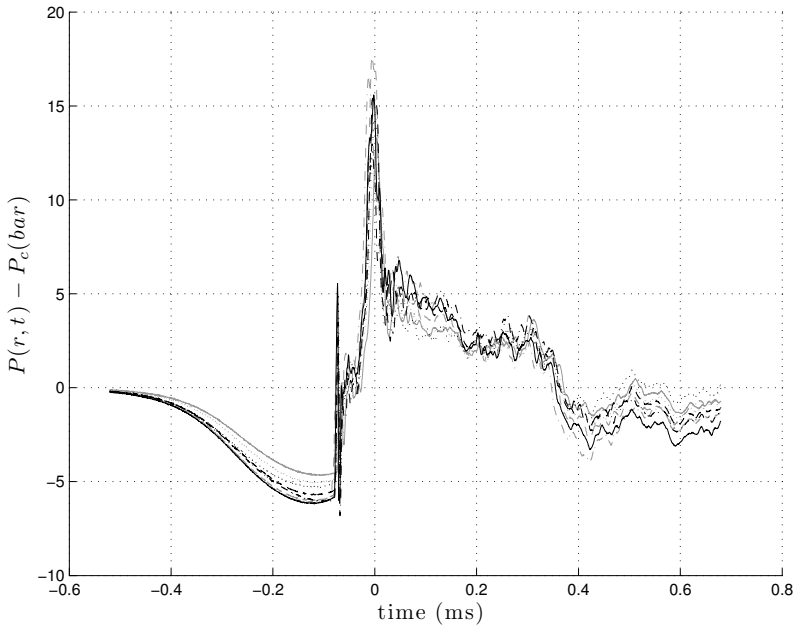

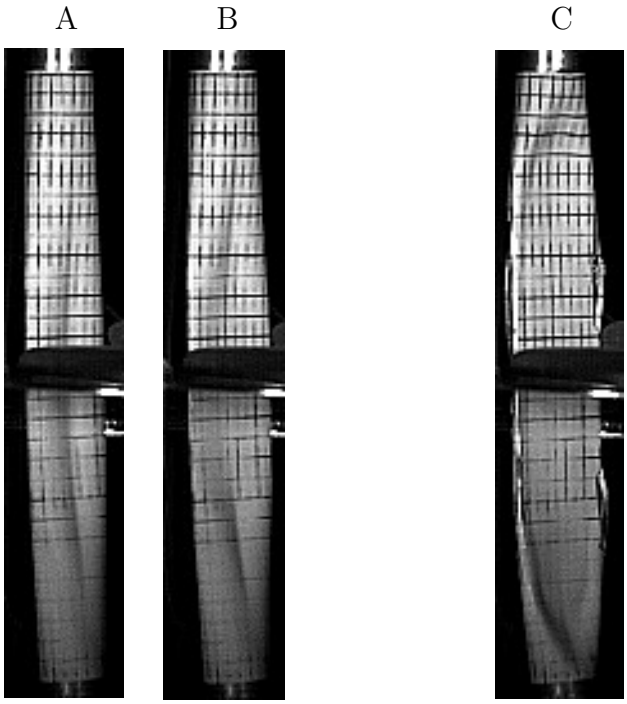

Figure A.6: B2D16r3

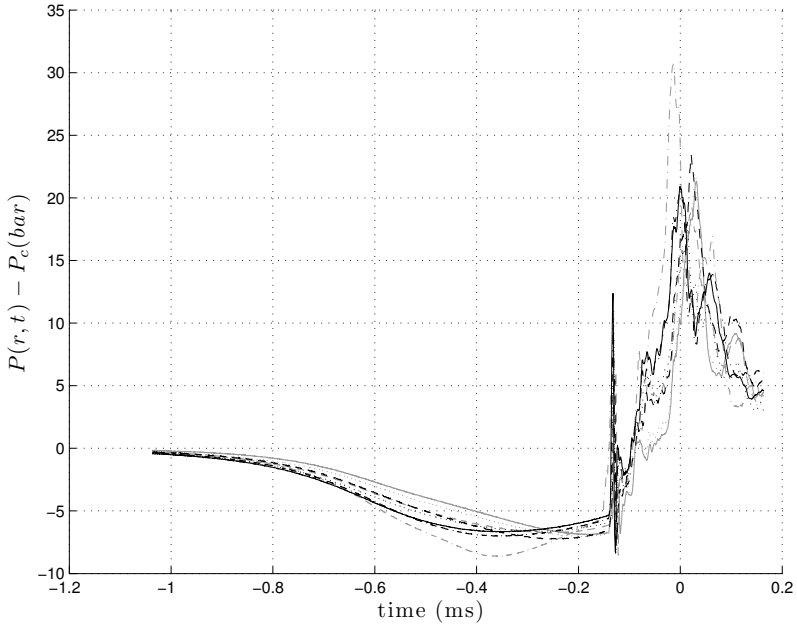

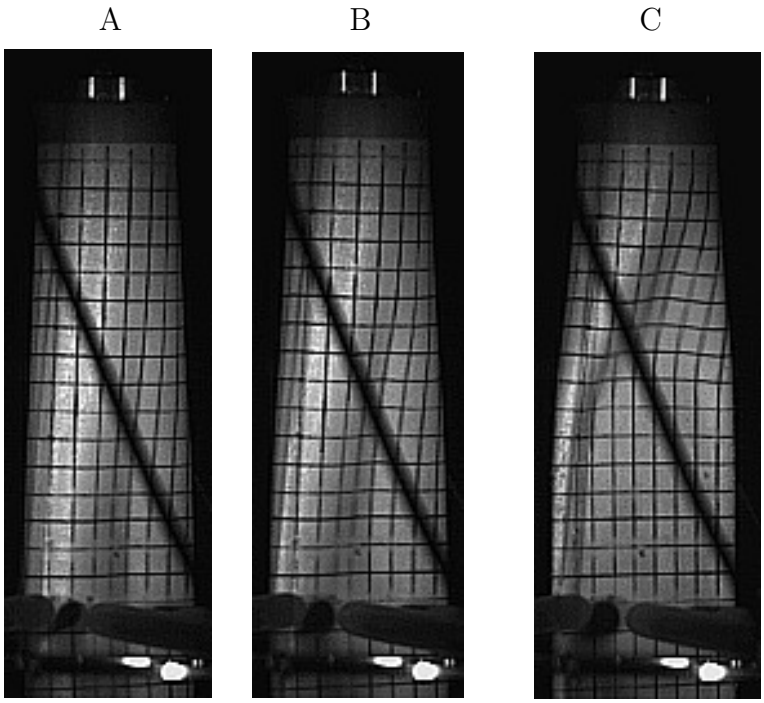

Figure A.7: A2A2r1

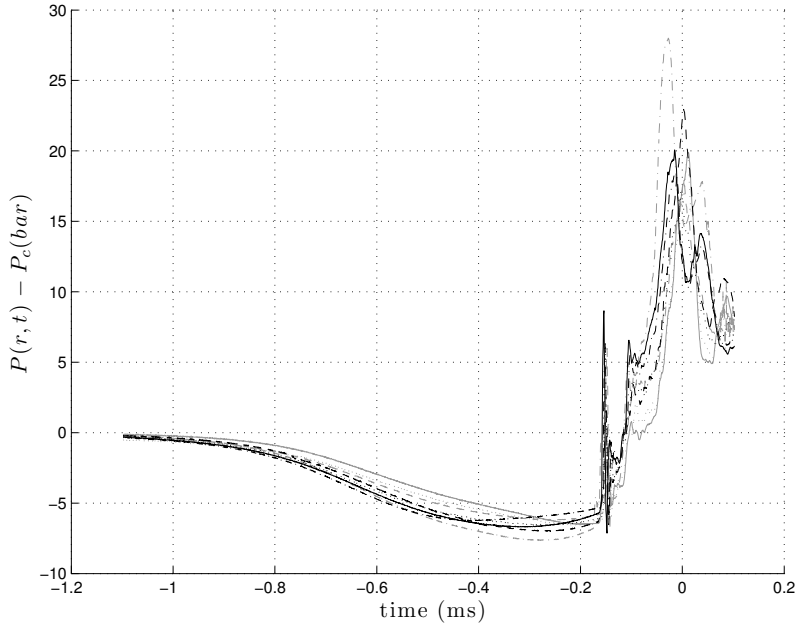

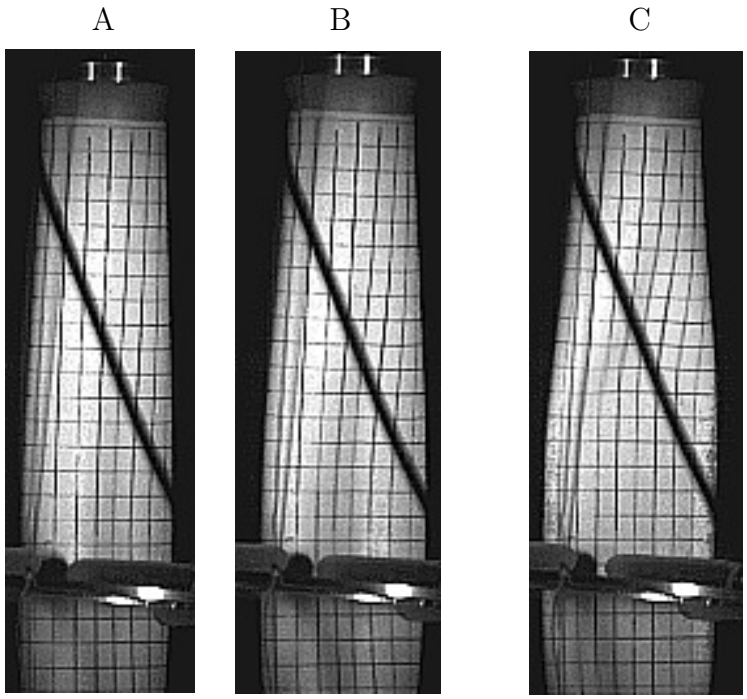

Figure A.8: A2A2r2

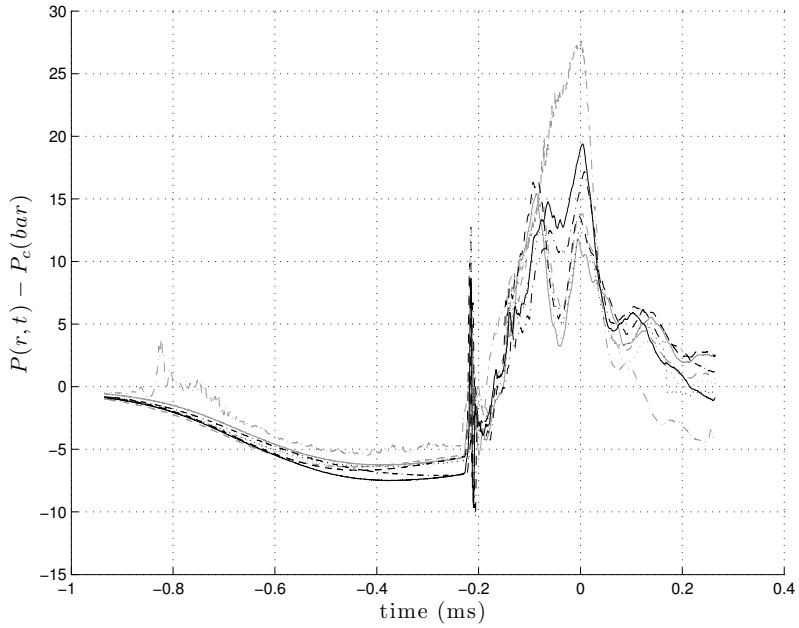

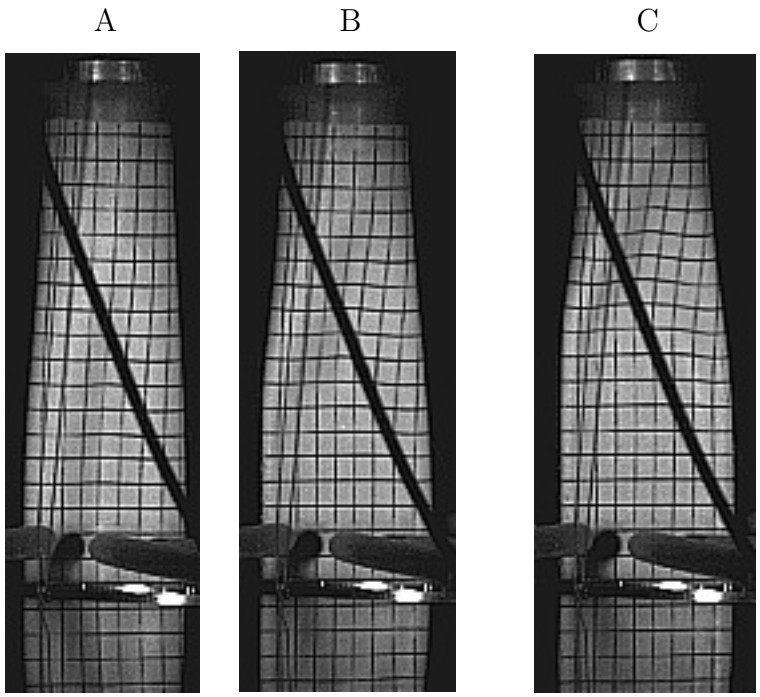

Figure A.9: A2A2r3

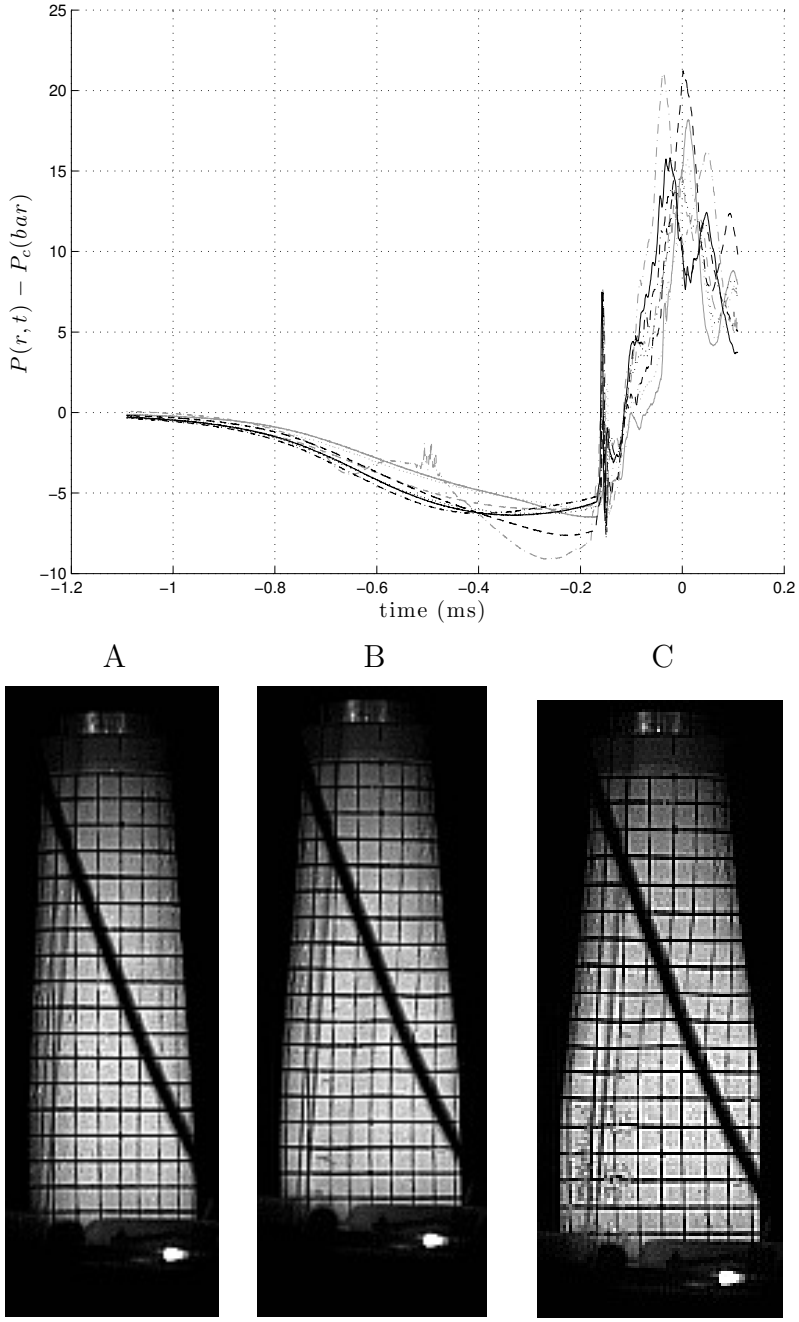

Figure A.10: A2A2r4

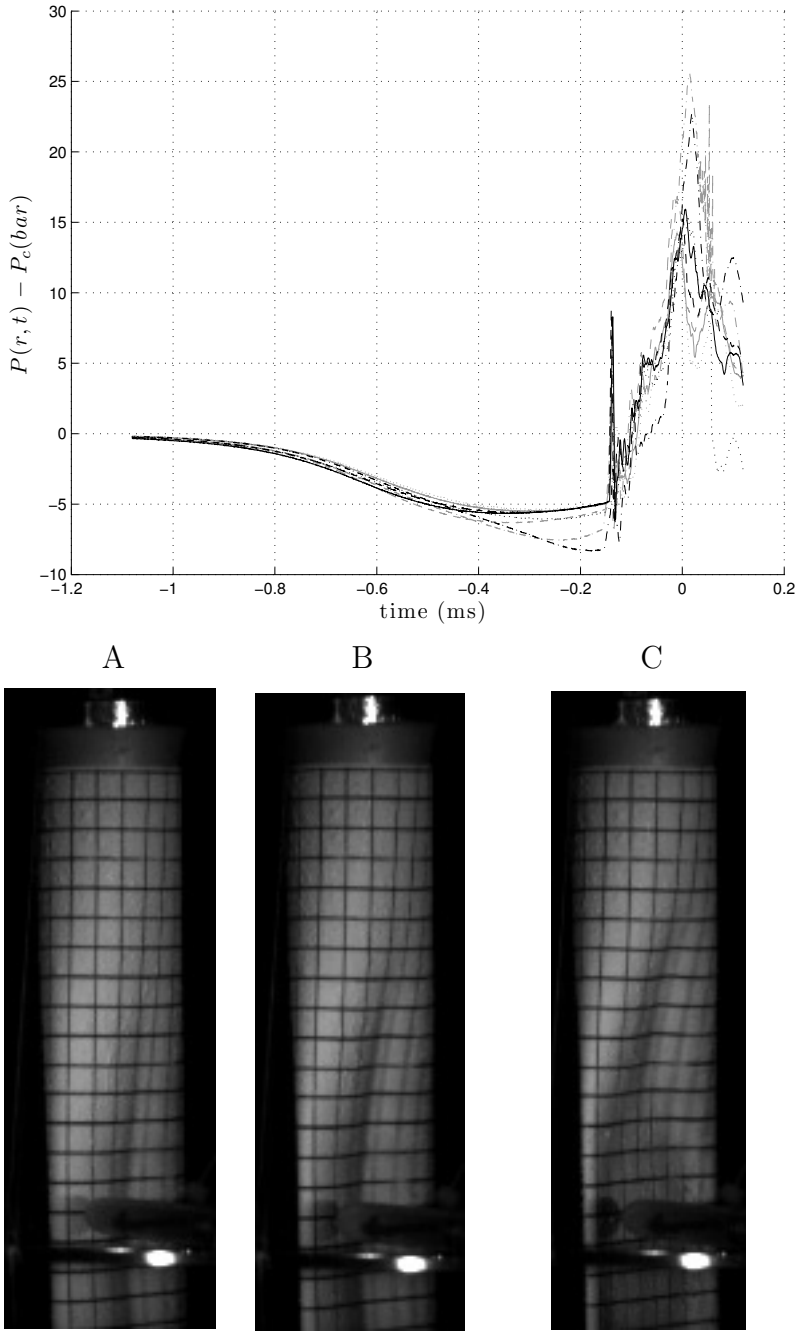

Figure A.11: A2A2r5

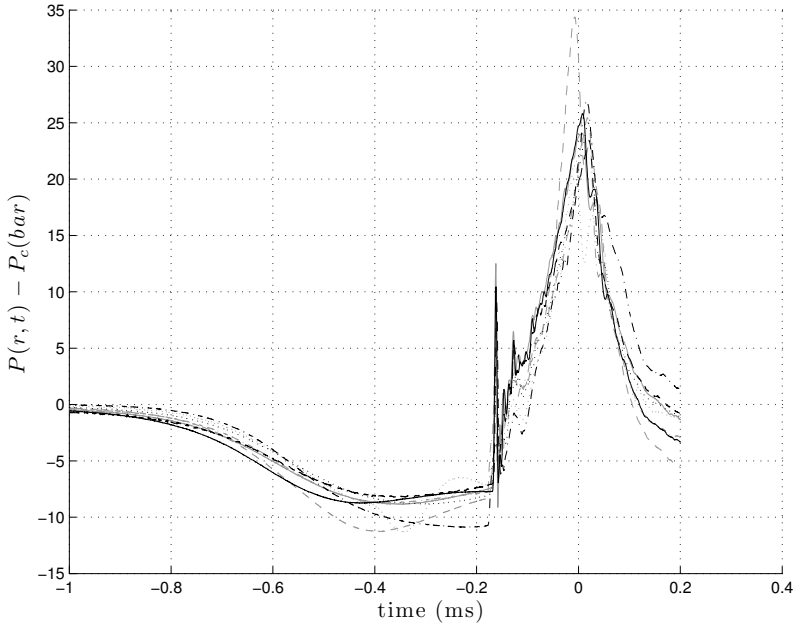

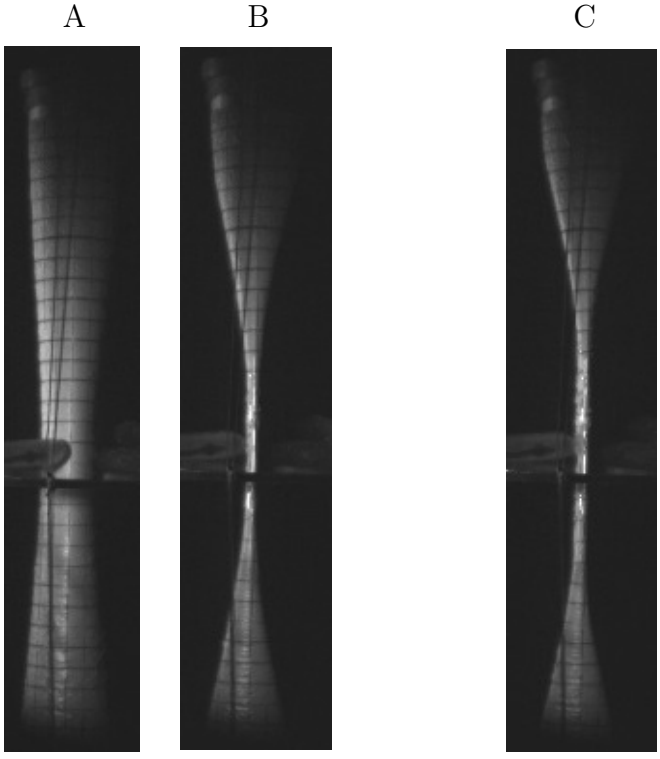

Figure A.12: A2A3r1

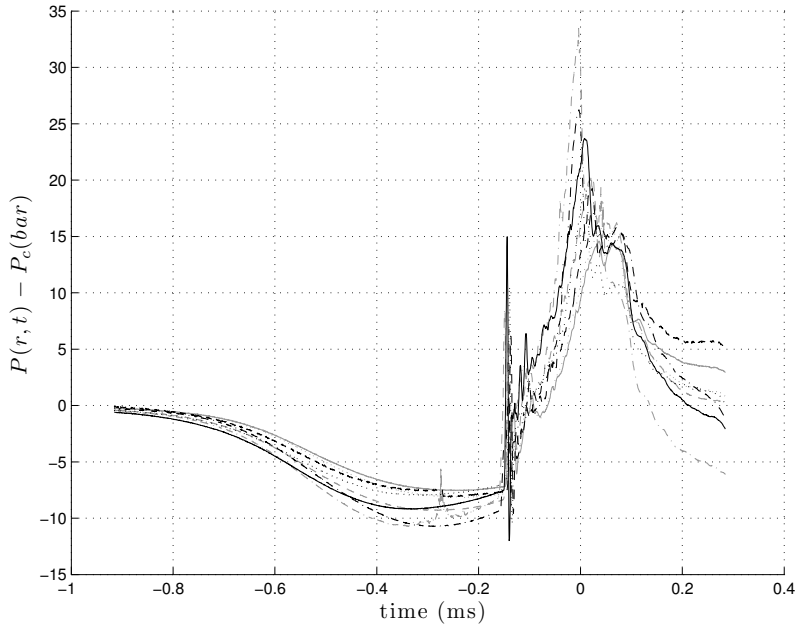

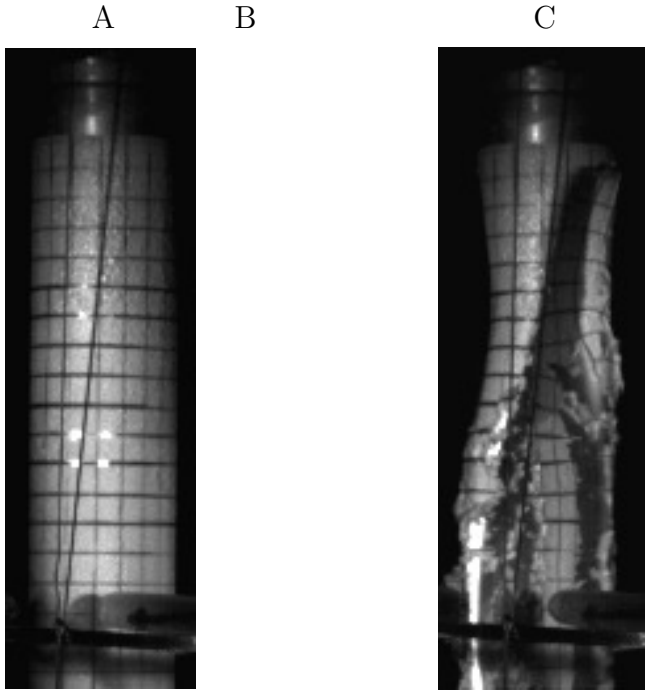

Figure A.13: A2A3r2

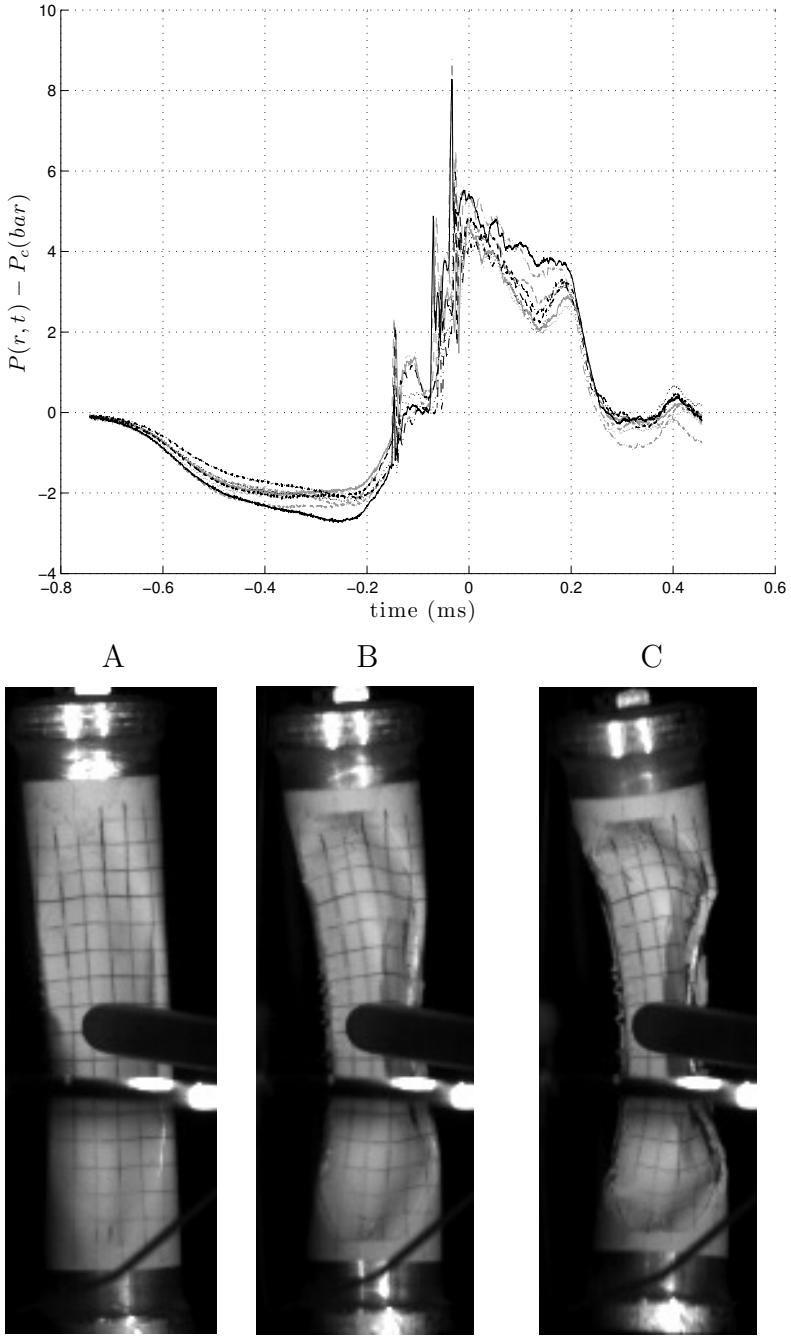

Figure A.14: B3D25r1

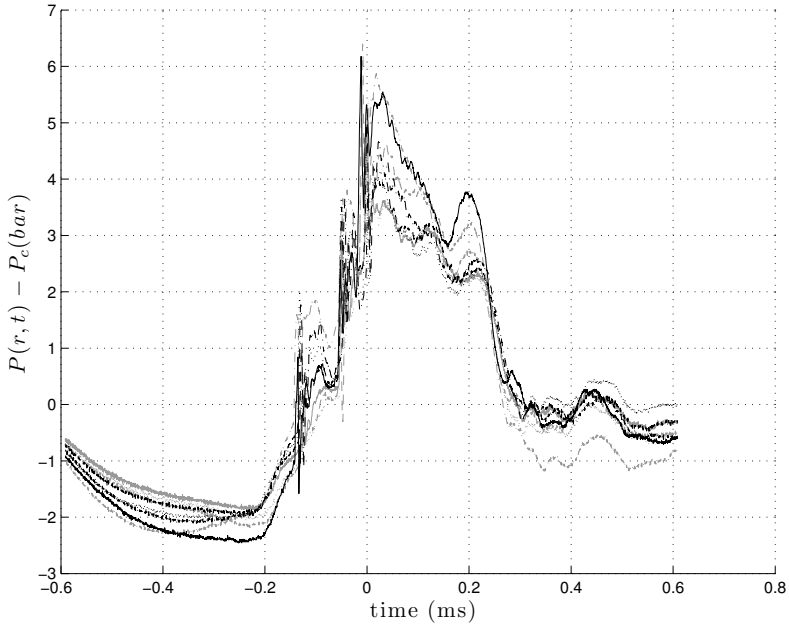

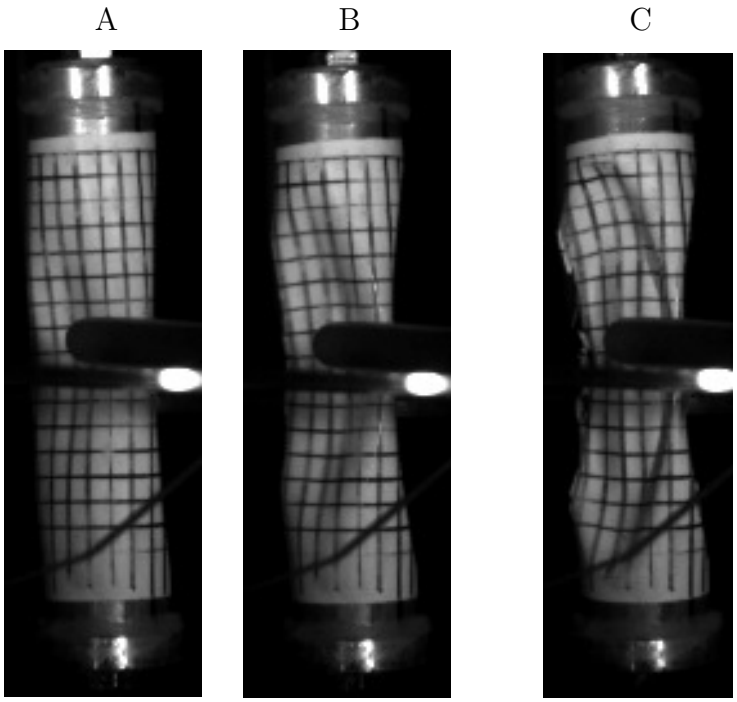

Figure A.15: B3D25r2

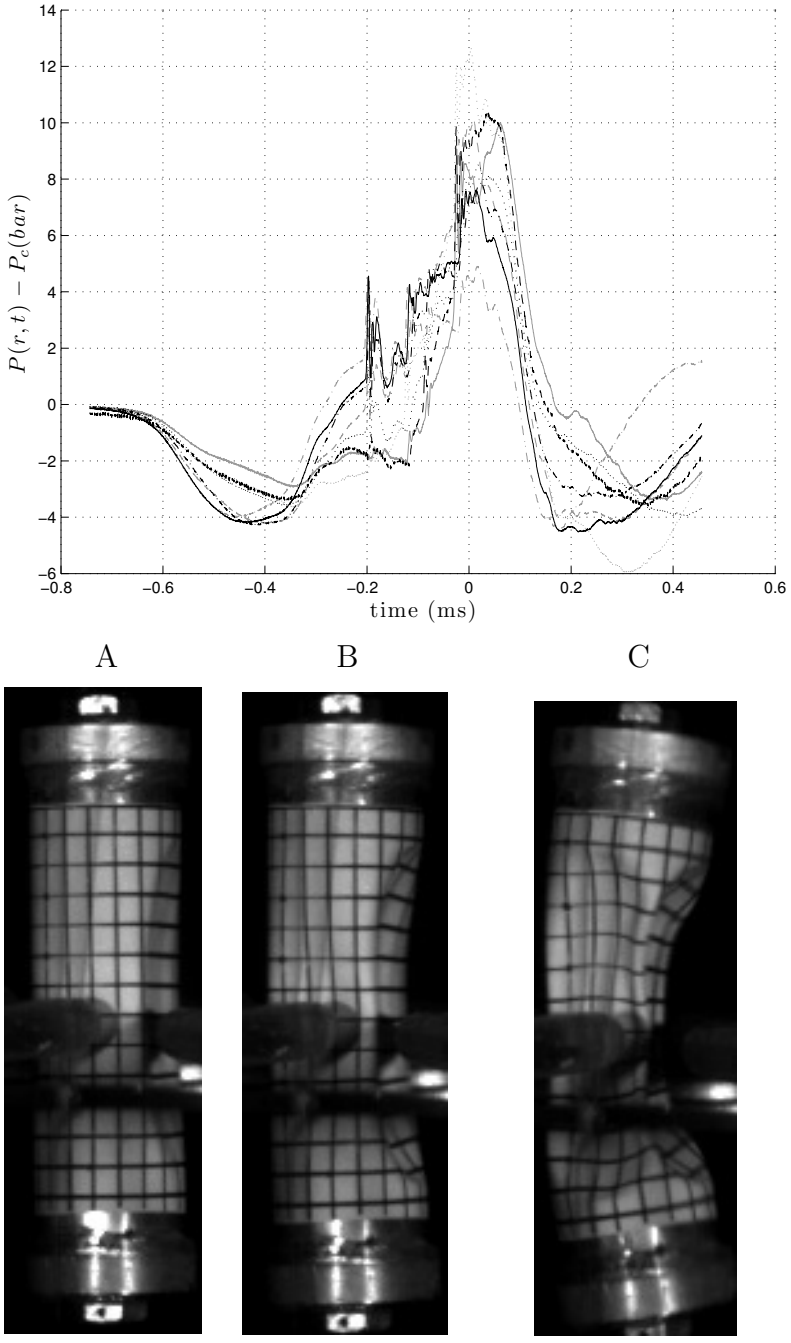

Figure A.16: B4D25r1

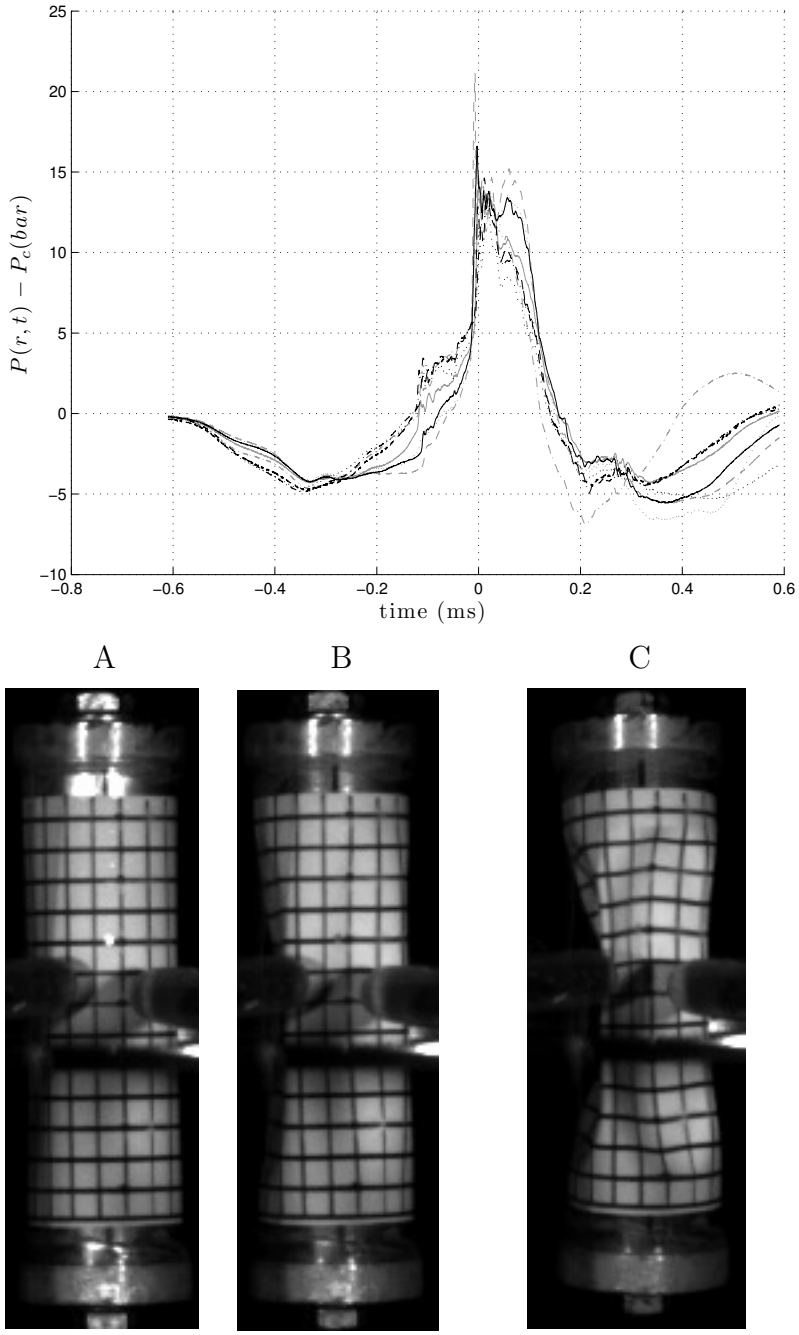

Figure A.17: B4D25r2

Appendix B
Natural Implosion Figures

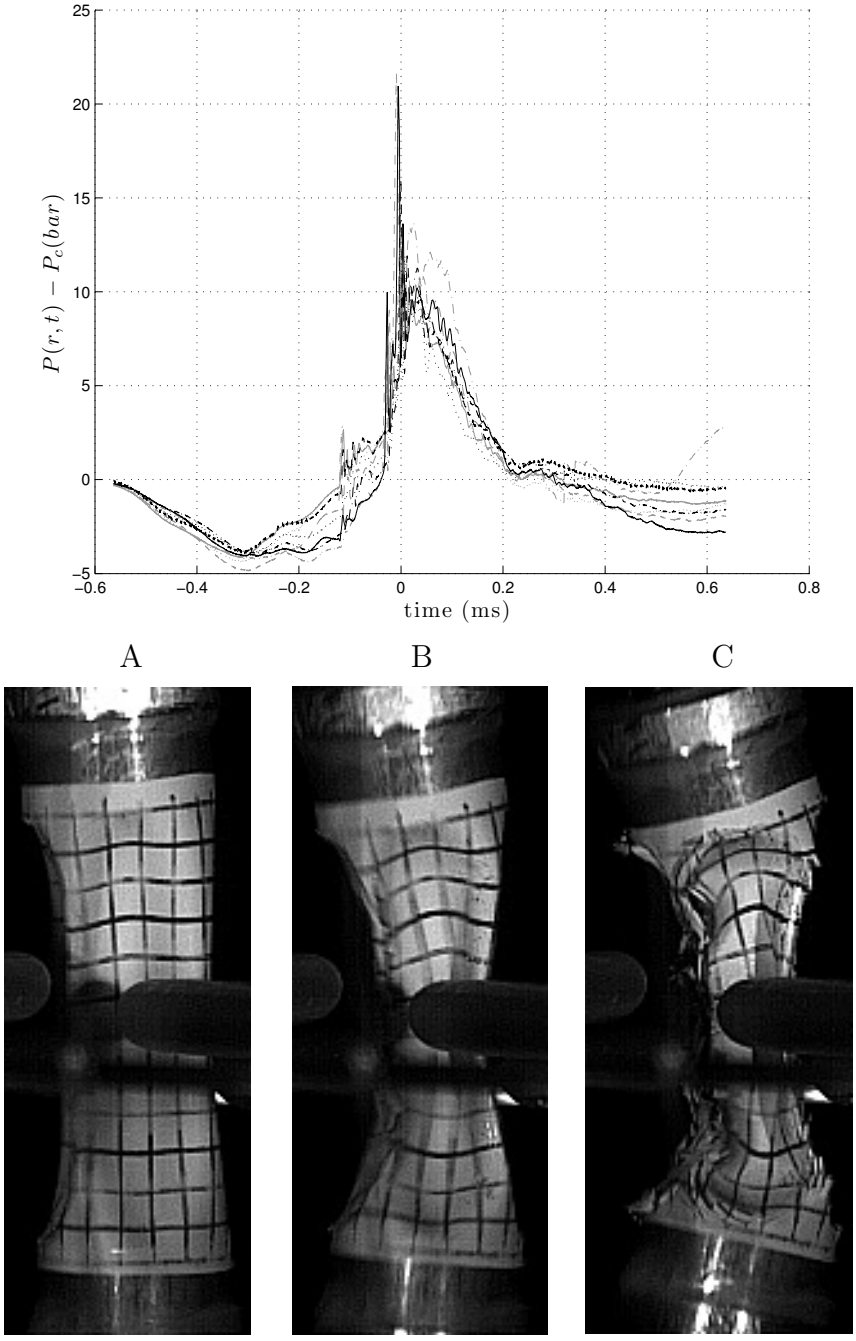

Figure B.1: B4D25r3

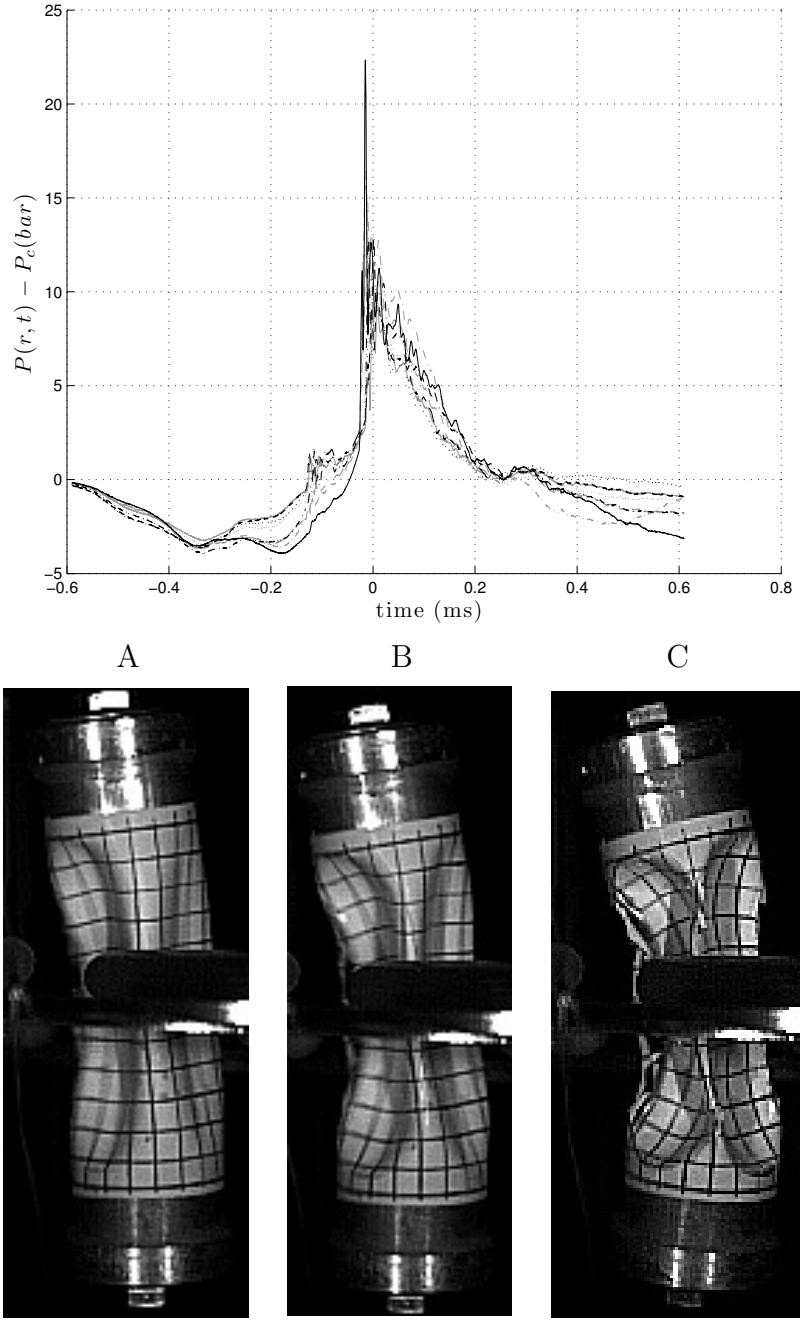

Figure B.2: B4D25r4

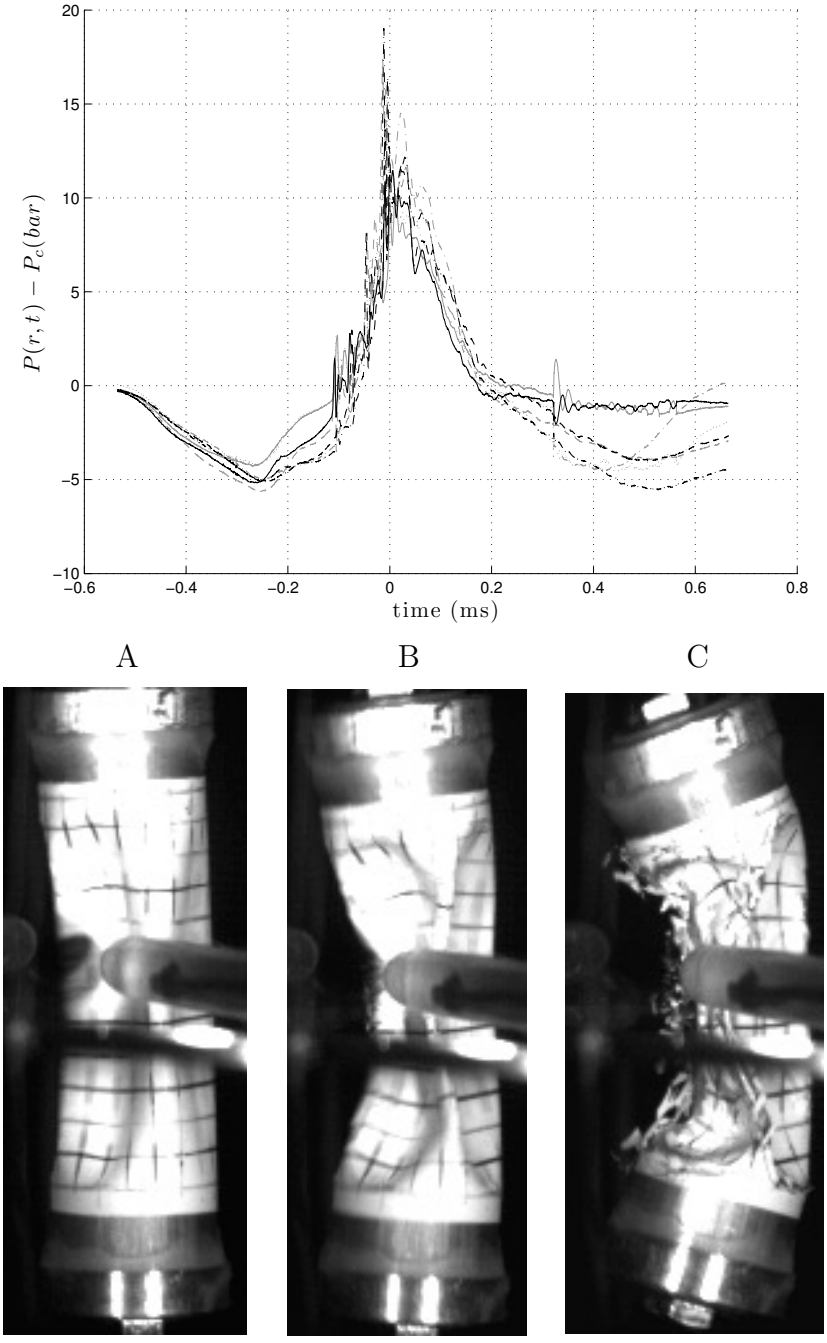

Figure B.3: B4D25r5

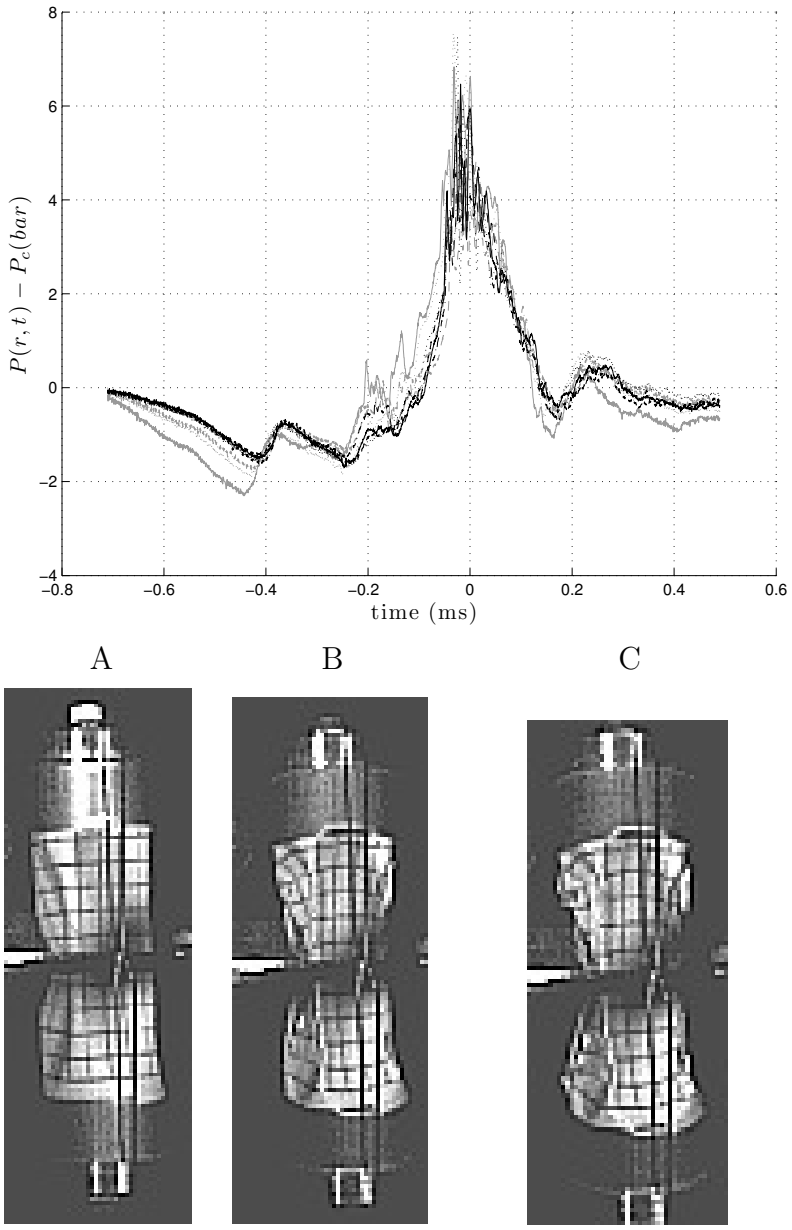

Figure B.4: B4D25r6

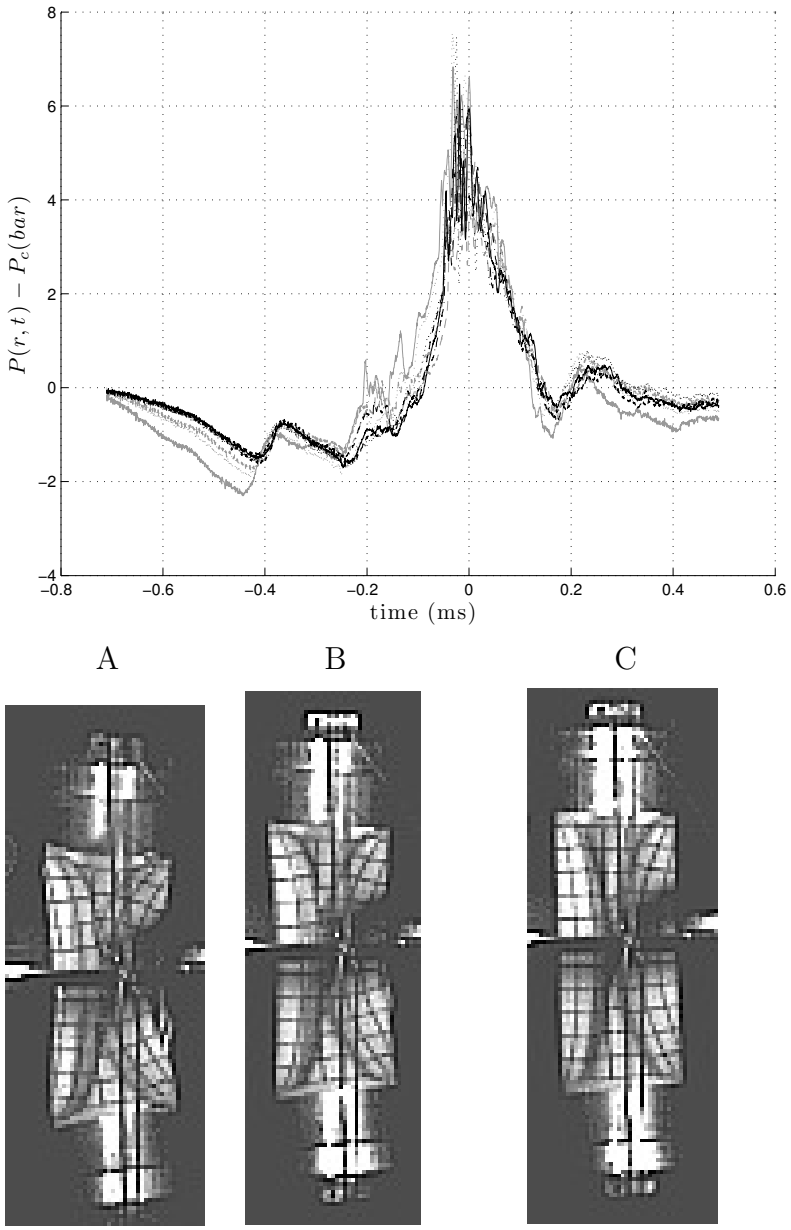

Figure B.5: B4D25r7

B3D25r1

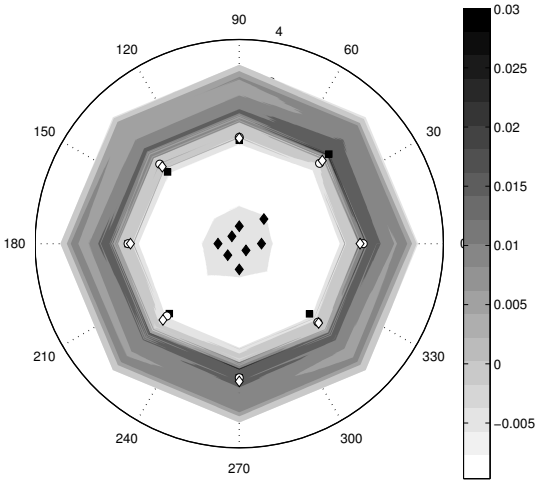

B3D25r2

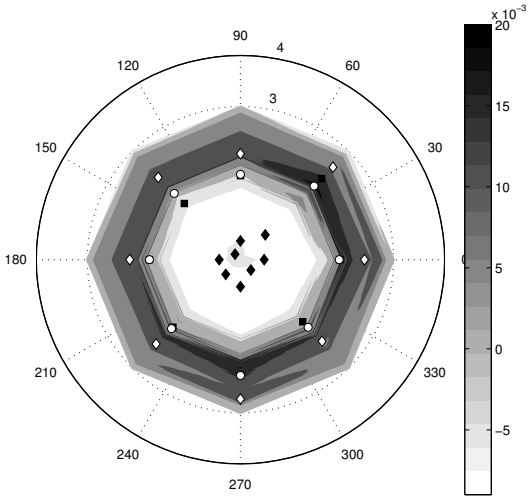

B3D25r3

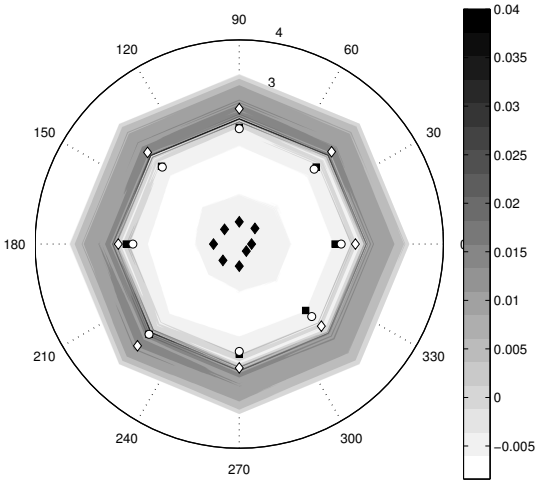

B3D25r4

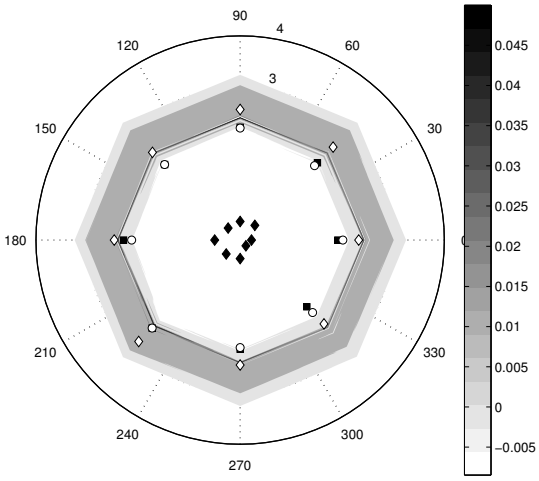

B4D25r1

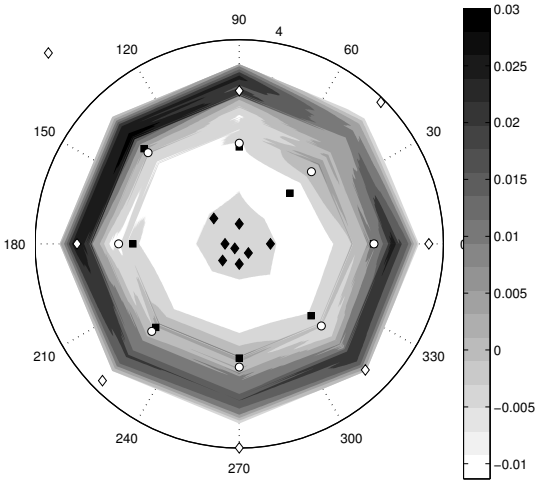

B4D25r2

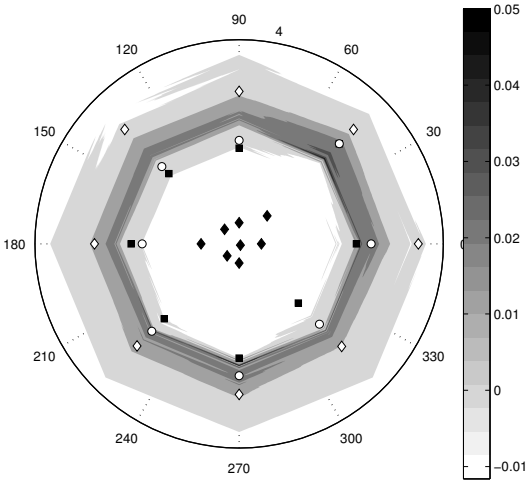

B4D25r3

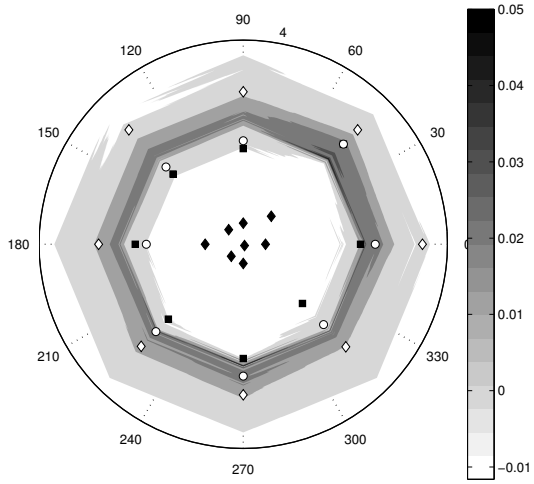

B4D25r4

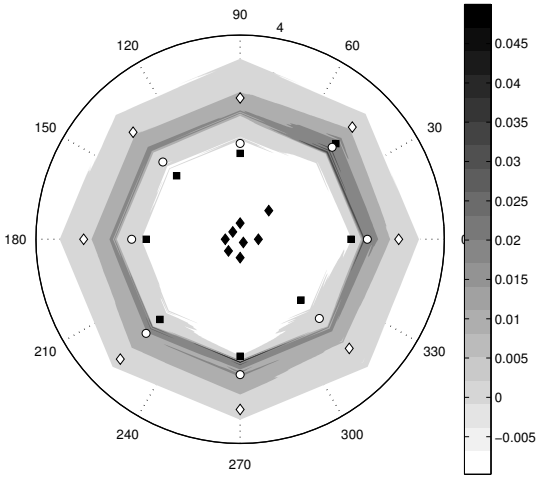

B4D25r6

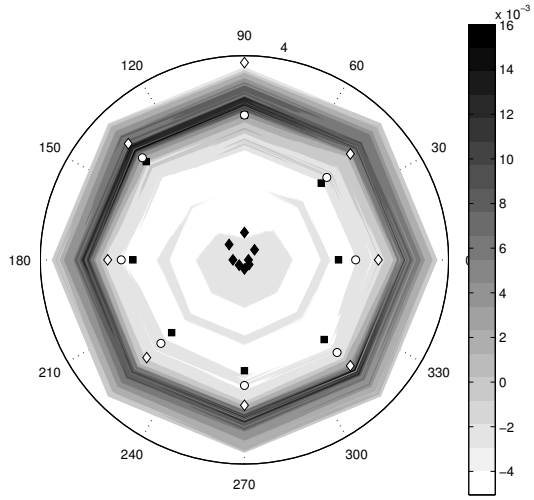

B4D25r6

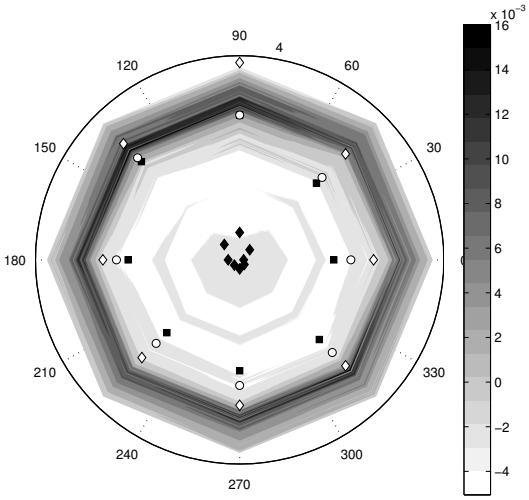

Bibliography

[1] AB Arons and DR Yennie. Energy partition in underwater explosion phenomena. *Reviews of Modern Physics*, 20(3):519, 1948.

[2] MRA Bagnold. Interim report on wave-pressure research. *London, En*, 1939.

[3] W.E. Baker, P.S. Westine, and F.T. Dodge. *Similarity methods in engineering dynamics: Theory and practice of scale modeling*. Spartan Books, 1973.

[4] A.B. Basset. On the difficulties of constructing a theory of the collapse of boiler tubes. *Philosophical Magazine*, 34:221–233, 1892.

[5] PA Blackmore and PJ Hewson. Experiments on full-scale wave impact pressures. *Coastal Engineering*, 8(4):331–346, 1984.

[6] J.M. Brett, G. Yiannakopoulos, and P.J. Van der Schaaf. Time-resolved measurement of the deformation of submerged cylinders subjected to loading from a nearby explosion. *International journal of impact engineering*, 24(9):875–890, 2000.

[7] G.H. Bryan. Application of the energy test to the collapse of a long thin pipe under external pressure. *Proceedings of the Cambridge Philosophical Society*, 6:287–293, 1888.

[8] GN Bullock, AR Crawford, PJ Hewson, and PAD Bird. Characteristics of wave impacts on a steep fronted breakwater. In *Coastal Structures' 99*, pages 455–463, 1999.

[9] GN Bullock, AR Crawford, PJ Hewson, MJA Walkden, and PAD Bird. The influence of air and scale on wave impact pressures. *Coastal Engineering*, 42(4):291–312, 2001.

[10] A.P. Carman. Resistance of tubes to collapse. *Physical Review*, 21:381–387, 1905.

[11] A.P. Carman. The collapse of short thin tubes. *University of Illinois Engineering Experiment Station Bulletin*, 99, 1917.

[12] A.P. Carman and M.L. Carr. Resistance of tubes to collapse. *University of Illinois Engineering Experiment Station Bulletin*, 5, 1906.

[13] A.P. Carman, M.L. Carr, et al. *Resistance of tubes to collapse*, volume 5. University of Illinois, Engineering Experiment Station, 1906.

[14] E. Chan and W. Melville. Deepwater breaking wave force on surface piercing structures. In *OCEANS 1984*, pages 565–570. IEEE, 1984.

[15] E.S. Chan. Mechanics of deep water plunging-wave impacts on vertical structures. *Coastal engineering*, 22(1-2):115–133, 1994.

[16] ES Chan and WK Melville. Deep-water plunging wave pressures on a vertical plane wall. *Proc. Roy. Soc. Lond. Series A*, 417(1852):95–131, 1988.

[17] RH Cole. *Underwater explosions*. Princeton UP, 1948.

[18] G. Cook. The collapse of short tubes by external pressure. *Philosophical Magazine*, pages 51–56, 1914.

[19] G. Cook. The collapse of short tubes by external pressure. *Philosophical Magazine*, 50:844–848, 1925.

[20] MJ Cooker and DH Peregrine. Computations of violent motion due to waves breaking against a wall. In *Proc. 22nd Int. Conf. Coastal Engng. Delft. ASCE*, volume 1, pages 164–176, 1990.

[21] M.J. Cooker and DH Peregrine. Pressure-impulse theory for liquid impact problems. *Journal of Fluid Mechanics*, 297:193–214, 1995.

[22] E. Corona and S. Kyriakides. Asymmetric collapse modes of pipes under combined bending and external pressure. *Journal of Mechanical Mechanics*, 126:1232–1239, 2000.

[23] R.A. Dalrymple and D.L. Kriebel. Lessons in engineering from the tsunami in thailand. *BRIDGE-WASHINGTON-NATIONAL ACADEMY OF ENGINEERING-*, 35(2):4, 2005.

[24] MC Davis and E.E. Zarnick. Testing ship models in transient waves. Technical report, DTIC Document, 1966.

[25] JW Dold and DH Peregrine. An efficient boundary-integral method for steep unsteady water waves. *Numerical methods for fluid dynamics II*, pages 671–679, 1986.

[26] D.G. Dommermuth, D.K.P. Yue, WM Lin, RJ Rapp, ES Chan, and WK Melville. Deep-water plunging breakers: a comparison between potential theory and experiments. *Journal of Fluid Mechanics*, 189(1):423–442, 1988.

[27] JH Duncan, V. Philomin, M. Behres, and J. Kimmel. The formation of spilling breaking water waves. *Physics of Fluids*, 6:2558, 1994.

[28] J.Y. Dyau and S. Kyriakides. On the propagation pressure of long cylindrical shells under external pressure. *International Journal of Mechanical Science*, 35:675–713, 1993.

[29] W. Fairbairn. On the resistance of tubes to collapse. *Philosophical Transactions of the Royal Society of London*, 148:389–413, 1858.

[30] M.S.H. Fatt. Elastic-plastic collapse of non-uniform cylindrical shells subjected to uniform external pressure. *Journal of Thin-Walled Structures*, 35:117–137, 1999.

[31] T.L. Geers and C.A. Felippa. Doubly asymptotic approximations for vibration analysis of submerged structures. *The Journal of the Acoustical Society of America*, 73:1152, 1983.

[32] M. Hattori, A. Arami, and T. Yui. Wave impact pressure on vertical walls under breaking waves of various types. *Coastal Engineering*, 22(1):79–114, 1994.

[33] M.S. Longuet Higgins and E.D. Cokolet. The deformation of steep surface waves on water. i. a numerical method of computation. *Proceedings of Royal Society of London A*, 350:1–26, 1976.

[34] H. Huang and YF Wang. Early-time interaction of spherical acoustic waves and a cylindrical elastic shell. *The Journal of the Acoustical Society of America*, 50:885, 1971.

[35] J.B. Keller and I.I. Kolodner. Damping of underwater explosion bubble oscillations. *Journal of applied physics*, 27(10):1152–1161, 1956.

[36] MS Kirkgöz. Breaking wave impact on vertical and sloping coastal structures. *Ocean engineering*, 22(1):35–48, 1995.

[37] YW Kwon and PK Fox. Underwater shock response of a cylinder subjected to a side-on explosion. *Computers & structures*, 48(4):637–646, 1993.

[38] S. Kyriakides and L.H. Lee. Buckle propagation in confined steel tubes. *International Journal of Mechanical Sciences*, 47:603–620, 2005.

[39] E. Lamarre and W.K. Melville. Instrumentation for the measurement of void-fraction in breaking waves: laboratory and field results. *Oceanic Engineering, IEEE Journal of*, 17(2):204–215, 1992.

[40] P. Lukkunaprasit and A. Ruangrassamee. Building damage in thailand in the 2004 indian ocean tsunami and clues for tsunami-resistant design. *The IES Journal Part A: Civil & Structural Engineering*, 1(1):17–30, 2008.

[41] S. Kyriakides N. Sakakibara and E. Corona. Collapse of partially corroded or worn pipe under external pressure. *International Journal of Mechanical Sciences*, 50:1586–1597, 2008.

[42] M. B. Oshnack, F. Aguiniga, D. Cox, R. Gupta, and J. van de Lindt. Effectiveness of small onshore seawalls in reducing forces induced by tsunami bore: Large-scale experimental study. *J. Disaster Research*, 4(6):382–390, 2009.

[43] T.D. Park and S. Kyriakides. On the collapse of dented cylinders under external pressure. *International Journal of Mechanical Science*, 38:557–578, 1996.

[44] DH Peregrine. Water-wave impact on walls. *Annual Review Of Fluid Mechanics*, 35:23–43, 2003.

[45] DH Peregrine and S. Kalliadasis. Filling flows, cliff erosion and cleaning flows. *Journal of Fluid Mechanics*, 310:365–374, 1996.

[46] S. Popinet and S. Zaleski. Bubble collapse near a solid boundary: a numerical study of the influence of viscosity. *Journal of Fluid Mechanics*, 464(1):137–163, 2002.

[47] R. J. Rapp and W. K. Melville. Laboratory measurements of deep-water breaking waves. *Phil. Trans. Roy. Soc. Lond. Series A*, 331(1622):735–&, 1990.

[48] G. Richert. Eexperimental investigation of shock pressures against breakwaters. In *Proceedings of 11th Int, Conf. Coast. Eng. ASCE*, pages 2954–2973, 1968.

[49] M. Salih Kirkgöz. Impact pressure of breaking waves on vertical and sloping walls. *Ocean Engineering*, 18(1-2):45–59, 1991.

[50] K. Sato, Y. Tomita, and A. Shima. Numerical analysis of a gas bubble near a rigid boundary in an oscillatory pressure field. *The Journal of the Acoustical Society of America*, 95:2416, 1994.

[51] H.E. Saunders and D.F. Windenburg. Strength of thin shells under external pressure. *Transcripts from the American Society of Mechanical Engineers*, 53:207, 1931.

[52] R.V. Southwell. On the collapse of tubes by external pressure. *Philosophical Magazine*, 24:687–698, 1912.

[53] R.V. Southwell. On the collapse of tubes by external pressure. *Philosophical Magazine*, 2:502–511, 1913.

[54] R.V. Southwell. On the collapse of tubes by external pressure. *Philosophical Magazine*, 29:67–77, 1915.

[55] R.T. Stewart. Collapsing pressure of bessemer steel lap-welded tubes, three to ten inches in diameter. *Transcripts from the American Society of Mechanical Engineers*, 27:730–822, 1906.

[56] R.G. Sturm. A study of the collapsing pressure of thin-walled cylinders. *University of Illinois Engineering Experiment Station Bulletin*, 329, 1941.

[57] ME Topliss, MJ Cooker, and DH Peregrine. Pressure oscillations during wave impact on vertical walls. In *COASTAL ENGINEERING CONFERENCE*, volume 2, pages 1639–1639. ASCE AMERICAN SOCIETY OF CIVIL ENGINEERS, 1992.

[58] S. E. Turner. Underwater implosion of glass spheres. *J. Acoust. Soc. Amer.*, 121(2):844–852, 2007.

[59] R. von Mises. Der kritische aussendruck fur allseits belastete zylindrischer rohre (the critical external pressure of cylindrical tubes under uniform radial and axial load), translated by df windenburg in 1933. *Festschrift, Prof. Dr. A. Stodola, Orell Fussli Veriag*, 53:418–430, 1929.

[60] C. Wang and BC Khoo. An indirect boundary element method for three-dimensional explosion bubbles. *Journal of Computational Physics*, 194(2):451–480, 2004.

[61] D.F. Windenburg and C. Trilling. Collapse by instability of thin cylindrical shells under external pressure. *Transcripts from the American Society of Mechanical Engineers*, 56(2):819–825, 1934.

[62] DJ Wood and DH Peregrine. Wave impact beneath a horizontal surface. In *COASTAL ENGINEERING CONFERENCE*, volume 3, pages 2573–2583. ASCE AMERICAN SOCIETY OF CIVIL ENGINEERS, 1996.

[63] D.J. Wood and D.H. Peregrine. Two and three-dimensional pressure-impulse models of wave impact on structures. *COASTAL ENGINEERING*, page 1503, 1998.

[64] D.J. Wood and D.H. Peregrine. Wave impact on a wall using pressure-impulse theory. ii: porous berm. *Journal of waterway, port, coastal, and ocean engineering*, 126:191, 2000.

[65] D.J. Wood, D.H. Peregrine, and T. Bruce. Wave impact on a wall using pressure-impulse theory. i: trapped air. *Journal of waterway, port, coastal, and ocean engineering*, 126:182, 2000.

[66] S. Zhang and J.H. Duncan. The final stage of the collapse of a cavitation bubble near a rigid wall. *J. Fluid Mech*, 1(257):147–181, 1993.

[67] S. Zhang and J.H. Duncan. On the nonspherical collapse and rebound of a cavitation bubble. *Physics of Fluids*, 6:2352, 1994.

[68] S. Zhang, D.K.P. Yue, and K. Tanizawa. Simulation of plunging wave impact on a vertical wall. *Journal of Fluid Mechanics*, 327:221–254, 1996.